Aeolian structure formation in a laboratory wind tunnel

Inaugural-Dissertation

zur

Erlangung des Doktorgrades

der Mathematisch-Naturwissenschaftlichen Fakultät

der Universität zu Köln

vorgelegt von

Merve Seçkin

aus

Attendorn

Köln, 2022

Berichterstatter:	Prof. Dr. Matthias Sperl
(Gutachter)	Dr. Eric J.R. Parteli
Tag der mündlichen Prüfung:	14. Juni 2022

To my parents, Hülya and Hayati Seçkin.

Abstract

Sand dunes and ripples result from the interaction between topography, hydrodynamics and sediment transport and exhibit self-organization on multiple scales. In this thesis, we show the formation of aeolian viscous bedload barchan-ripples in a laboratory wind tunnel. These bedforms are subject to the same longitudinal instability and transverse instability as subaqueous ripples and aeolian dunes and share the same transport mechanism as subaqueous ripples, thus making our bedforms the aeolian counterpart of subaqueous ripples. To realize such an experiment, we carefully select a particle system with small particle diameters at low densities. We follow the evolution of barchan-ripples from onset to their steady state form and show that they arise from both a flat particle bed and a particle heap. We study the transport mechanism at the particle level and demonstrate that the aeolian viscous bedload transport regime is responsible for the formation of the barchan-ripples. We measure and derive the saturation length from equations given by calibrated numerical and theoretical models and show that the order of magnitude is in the millimeter range. Access to this previously unexplored area in parameter space gives us a deeper understanding of the mechanisms that govern sedimentary bedform formation on controllable time and length scales.

Zusammenfassung

Die Entstehung von Dünen und Rippeln ist auf das Wechselspiel zwischen Topografie, Hydrodynamik und Sedimenttransport zurückzuführen. Diese sedimentären Bettformen weisen Selbstorganisation auf mehreren Skalen auf: von zentimetergroßen, sich wiederholenden Mustern bis zu hunderte Meter hohen Dünen. In dieser Arbeit untersuchen wir die Formation von zentimetergroßen, äolischen Barchan-Rippeln in einem Laborwindkanal, die sich aufgrund der viskosen Schicht der turbulenten Grenzschicht bilden. Diese Bettformen unterliegen derselben longitudinalen Instabilität und transversalen Instabilität wie Unterwasserripple und äolische Dünen. Die Barchan-Rippel entstehen durch den gleichen Transportmechanismus wie Unterwasserrippel, was sie zum äolischen Gegenstück macht. Für die Umsetzung dieses Experimentes wählen wir ein Teilchensystem aus, welches kleine Durchmesser bei gleichzeitig geringer Dichte aufweist. Wir zeigen die Entstehung der äolischen Barchan-Rippel aus einem flachen Teilchenbett und einem Teilchenhaufen. Wir untersuchen den Transportmechanismus auf Teilchenebene und zeigen, dass der Barchan-Rippel in der äolischen viskosen Schicht der turbulenten Grenzschicht entsteht. Wir messen die Saturationslänge und leiten sie zudem aus Gleichungen ab, die von kalibrierten numerischen und theoretischen Modellen vorhergesagt werden und zeigen, dass sich die Größenordnung im Millimeterbereich befindet. Der Zugang zu diesem bisher unerforschten Parameterbereich der äolischen Bettformbildung ermöglicht uns ein besseres Verständnis der Mechanismen, denen sedimentäre Bettformbildung unterliegen zu erhalten.

Contents

Introduction

A sand dune with superimposed impact ripples, Morocco

'Here, instead of finding chaos and disorder, the observer never fails to be amazed at a simplicity of form, an exactitude of repetition, and a geometric order unknown in nature on a scale larger than that of crystalline structure.'

R.A.Bagnold (1941)

Sedimentary transport shapes the landscape that surrounds us. Whenever a fluid flows over a loose sedimentary bed consisting of grains with sufficiently large shear forces, the grains are entrained, and bedforms evolve [1–3]. These bedforms typically manifest as ripples or dunes, two types of sediment heaps that we find not only in the desert but also on planets like Mars and Venus and celestial bodies such as Pluto, Churyumov–Gerasimenko, and Titan, one of Saturn's moons [4–7].

From a geological perspective, we can draw conclusions about the paleoenvironment, the environment at a particular time in the geological past, from the study of sedimentary bedforms [8]. The emergence of particular bedforms provides information about climate and sediment characteristics of times long ago and of environments far away, where direct measurements of these characteristics are challenging. For example, analyzing satellite images of bedforms on Mars promises access to the evolution of the climate on Mars [8, 9].

One bedform observed on Mars is particularly puzzling. Bedforms called large Martian wind ripples have been discovered [8]. They are discussed to originate from the same mechanism that on Earth lead to subaqueous ripples [8, 10] or from the same mechanism that on Earth lead to aeolian impact ripples [11]. Thus, they may be indicative for very different environments.

The uncertainty emerges to a large extend from the lack of observations of large wind ripples on Earth. This is mainly caused by the conditions that are necessary to observe the same bedforms in terrestrial terrain. Only fine sand particles can be entrained in the same transport layer where subaqueous ripples develop: the viscous sublayer, a thin layer of flow next to the boundary in which viscous shear stress dominates over turbulent shear stress [12]. Due to attractive forces between the fine grains, the threshold for entrainment by the wind increases. However, the entrainment threshold is typically high, so that grains are entrained in suspension, i.e., lose contact with the bed and are transported over long distances [2]. Thus, an aeolian counterpart to subaqueous ripples on Earth has not yet been observed. Our approach taken in this work is to study this research area by selecting a particle system that allows us to form migrating aeolian bedforms equivalent to subaqueous ripples in a controllable environment of a laboratory wind tunnel.

We will organize this thesis as follows.

In chapter 1, we will introduce the basic principles of structure formation and give insights into the characteristics of flows and sediment, sediment transport, and finally, the coupling of hydrodynamic flow and sediment transport. These concepts will allow us to understand which experimental setup we need to observe migrating aeolian bedforms in the laboratory, much like subaqueous ripples, and interpret this thesis's results.

Chapter 2 is dedicated to the characterization of the setup. We will present a particle system and a custom-made low-speed wind tunnel suitable for studying aeolian viscous bedload bedforms in the laboratory. For this purpose, we first introduce the basic properties of the selected particle system, provide details on the material preparation and microscopy images. Then, we characterize the wind tunnel by surveying the accessible operating speeds and provide velocity mapping from which we will derive characteristic parameters.

In chapters 3 to 5, we will focus on the formation of our aeolian bedforms, which we will term aeolian viscous barchan-ripple. Chapter 3 shows that a flat particle bed consisting of the selected particle system is unstable to wind exposure and decays into migrating barchan-ripples. We compare our flat particle bed experiment results with numerical simulation results and subaqueous experiments. We then measure the particle flux over a flat particle bed and derive a length characteristic of bedform formation called the saturation length.

In chapter 4, we study the formation of barchan-ripples from particle heaps. We follow the evolution from the onset of formation to its mature shape. For this, we show superimposed images in time-lapse sequence, map the dimensions of the structure, and present the height profile evolution. Afterward, we relate our bedforms to subaqueous ripples and aeolian dunes by calculating and comparing characteristic parameters.

In chapter 5, we investigate the motion on a particle level. We introduce a second particle system similar to the previously introduced particle system, differing only in diameter. We track the particle motion on a heap of the respective particle type with a high-speed camera and measure the velocity of the particles under wind exposure. We calculate the predicted characteristic lengths that result for both systems. Finally, we show the evolution of a transient bedform arising from a heap consisting of the new particle system, allowing us to infer conclusions about the transport mechanism.

In the penultimate chapter 6, we summarize our results and note the implications this work has for future research. Finally, in chapter 7, we suggest further investigations that follow from this work and present preliminary results.

1 Basic Principles of Structure Formation

A centimeter-sized barchan-ripple that evolved in the wind tunnel

'Nor can the geomorphologist rest content, in his study for its own sake of the shape and movement of sand accumulations, until he knows why sand collects into dunes at all, instead of scattering evenly over the land as do fine grains of dust, and how the dunes assume and maintain their own especial shapes.'

R.A.Bagnold (1941)

1.1. Introduction

To understand the physical mechanisms that govern sedimentary bedform formation, we have to discuss the interaction between fluid flow and sediment. For this purpose, we will first highlight the characteristics of flows, then those of sediment and sediment transport, and finally the coupling of hydrodynamic flow, the topography and sediment transport, leading to the formation of bedforms.

First, we will give some insights into boundary layer physics and explain which types of flows exist, and how a flat surface and a hill or undulating topography often found in nature affect these flows.
Then, our focus will shift to granular matter: the sediment types involved in structure formation, the forces acting on a single particle at rest on a granular bed, and those necessary to transport this particle. Once lifted, the conditions for continuous transport of the grain and the variety of transport mechanisms resulting from the interaction with the surrounding grains will give us a deeper insight into the physics of sediment transport.
In the penultimate section, we will combine the previous building blocks and examine the interaction between fluid, topography, and sediment transport. Finally, we will highlight characteristic length scales that influence structure formation and the typical morphologies that arise from them.
After these three sections, we will be able to answer the following questions:

1. How can fluid flow at a boundary be described? (sec. 1.2)
2. How do properties of granular matter affect aeolian structure formation? (sec. 1.3)
3. How does the interaction between topography and fluid flow lead to the formation of ripples and dunes? (sec. 1.4)

Finally, based on these three sections, we will discuss our approach taken in this work and answer two further questions: which particle system can self-organize into structures in a low-speed wind tunnel on a centimeter-sized test surface? And which specific wind tunnel setup do we need for this purpose?

1.2. Boundary Layer Physics

This section covers the field of boundary layer theory, focusing on fluids flowing close to a surface. We will not consider large-scale atmospheric effects influencing the flow, such as the Coriolis or thermal effects or the impact of storms. In both turbulent and laminar boundary layer flows, many different morphologies evolve in the presence of loose sediment. Some appear in both boundary layers over several orders of magnitude [2]. To understand this, we will first look at the different types of flow and their characteristics: laminar and turbulent flows in contact with a flat surface and, later, the influence of a hill on the flow behavior. At the end of this section, it will become clear which unique properties and similarities a flow can have across diverse fluids and which relevance this has for the upcoming chapters. Finally, we will answer the following questions:

1. How are different types of flows characterized?
2. What are the effects of a surface on the fluid flow?
3. To what extent does the roughness of a surface disturb the flow?
4. How does the flow respond to the presence of a hill or complex topography?

We follow the structure and didactic approach of the textbook by authors Pye and Tsor 'Aeolian Sand and Sand Dunes' [2]. The descriptions of the basics are drawn from this textbook unless stated otherwise.

1.2.1. Laminar and Turbulent Boundary Layer

A fluid is defined as a substance that deforms under an applied shear force. The characteristic material property of fluids is the dynamic viscosity, which is a measure of its ability to resist deformation [13]. Although it is reasonable to model fluids as a continuum, i.e., modeling large-scale motion patterns and neglecting discrete particle dynamics, interactions on a molecular level are still significant.

Consider a steady flow, i.e., the velocity does not change with time, flowing parallel to a smooth surface. The macroscopic flow will tend to move in thin layers, which do not disrupt each other. But the adjacent layers still interact at a molecular level, i.e., momentum transport arises through the motion and interaction of molecules at the interface. This interaction results in mixing and is the origin of viscosity [13].

The example given above is known as viscous, stratified, or laminar flow. The flow is stratified if there is little or no mixing between the layers. This is primarily the case for low flow velocities or high fluid viscosities. Figure 1.1 illustrates how viscous shear stresses arise. Due to molecular friction, the lowest thin layer adheres to the ground, and a linear velocity gradient develops. A force per unit area must be applied to overcome viscosity for the layers of thickness dz to slide past each other. The velocity gradient dU/dz is also known as the shear rate and is the cause of the resulting shear stress τ:

$$\tau = \mu \frac{dU}{dz}, \qquad \textit{viscous shear stress} \tag{1.1}$$

with the dynamic viscosity μ as a proportionality factor and fluid velocity U. The kinematic viscosity is given by the dynamic viscosity divided by the fluid density ($\nu = \mu/\rho$) and is introduced to simplify the comparability between different fluids. ν equals $1.45 \times 10^{-5}\,\mathrm{m}^2\,\mathrm{s}^{-1}$ for air and is a factor 10 higher underwater.

The flow obeys Newton's laws, i.e., inertial forces must overcome viscous forces to sustain motion. The ratio between inertial and viscous forces is defined as a dimensionless number named after Osborne Reynolds.

$$\mathrm{Re} = \frac{\rho L U}{\mu} = \frac{LU}{\nu}, \qquad \textit{Reynolds Number} \tag{1.2}$$

where L is the characteristic length and depends on the investigated flow scale and fluid density ρ. Equation (1.2) describes whether a fully developed flow condition leads to a laminar or turbulent flow. For small Reynolds numbers, viscous effects dominate, and the flow is laminar; for large Reynolds numbers, the stratification is disturbed by eddies through non-directional and random velocity fluctuations in time and space. In this case, the macroscopic exchange is dominant, in which the

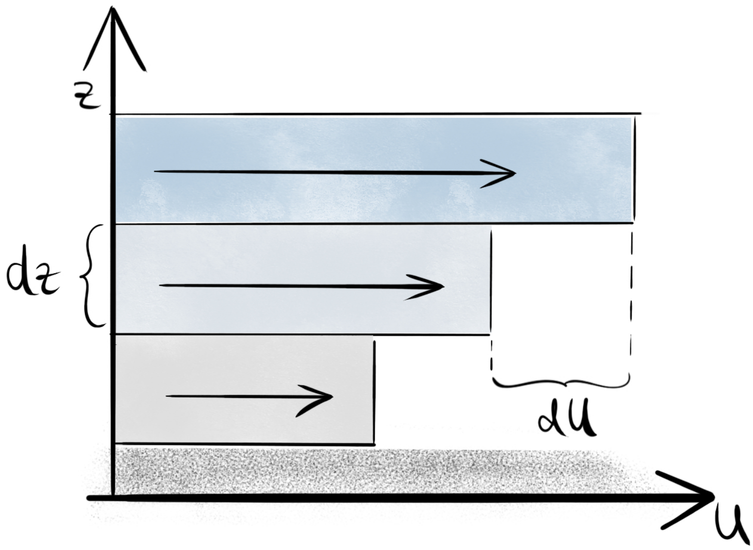

Figure 1.1.: Adjacent fluid layers sliding past each other. The lowest thin layer adheres to the ground, which results in a linear velocity gradient. Figure inspired by Pye and Tsoar [2].

viscous shear stress becomes negligible. The transition from laminar to turbulent flow occurs at a Reynolds number greater than 6000 (critical Re). Since there is a momentum exchange between the layers in turbulent flows, the total mean shear stress is composed of both viscous and turbulent shear stresses:

$$\tilde{\tau} = \tau + \tau_t = (\mu + \eta)(d\tilde{U}/dz), \qquad \textit{mean shear stress.} \tag{1.3}$$

The first term corresponds to equation (1.1), while the second term includes the so-called eddy viscosity η, representing the rate of turbulence [14]. In addition, the averaged velocity $\tilde{U}$ is introduced to cover the contribution of turbulent fluctuations. Determining the fluctuating component is complex but can be modeled using the mixing length theory of Prandtl and colleagues [15]. The eddy viscosity is interpreted as a mixing length, representing the characteristic distance that a fluid element travels before it interacts and mixes with the surrounding fluid, similar to the mean free path. Figure 1.2 shows both flow types in comparison. The distinction between laminar and turbulent flows is thus based on the ability of the adjacent layers to mix. While in laminar flows, the viscous shear stresses keep the fluid particles within one layer, and interaction appears only on a molecular level at the layer interfaces; in turbulent flows, an intense mixing develops across layers on a macroscopic scale. A laminar flow is only stable if externally imposed perturbations can be damped out [13].

Figure 1.2.: Schematic comparing laminar and turbulent flow. Left: A laminar flow in which the adjacent layers do not mix. Right: Turbulent eddies induce intense mixing of the layers. The stratification of the flow is disturbed.

Furthermore, we characterize a flow by the relative magnitude of inertial and gravity effects, which is the definition of the Froude number:

$$Fr = \frac{U_\infty^2}{gL}, \qquad \textit{Froude number} \tag{1.4}$$

with the undisturbed velocity far from the surface U_∞, the characteristic length L, mostly the depth of the flow, and the gravitational acceleration g. In water with a free surface, this ratio of inertial to gravitational forces plays a significant role in describing the state of a flow disturbance [13, 16] and thus the emergence of bedforms [17].

At the beginning of the section, we implicitly mentioned the concept of a boundary layer using the example of laminar flow. In 1904, Ludwig Prandtl introduced this very concept in a lecture at the Heidelberg Mathematical Congress [18]. He simplified the treatment of complex flow equations by separating the flow field over a surface into two regions:

1. the outer layer, in which viscous friction losses are negligible, and the flow is considered inviscid and

2. the inner layer very close to the surface, where viscous effects near the wall dominate.

A fluid flowing along a wall forms a boundary layer where viscous effects are responsible for developing a velocity profile perpendicular to the wall, regardless of flow type. Figure 1.3 visualizes a plane wall's impact on an incoming fluid and the resulting transition from a laminar into a turbulent boundary layer. In this illustration, the thickness of the boundary layer increases from laminar to turbulent. This difference can be explained by the induced eddy disturbances, which increase the vertical distance to the undisturbed flow. A viscous sublayer can remain in the turbulent boundary layer as long as the surface is smooth. The inner layer corresponds to the region in which viscous terms remain relevant in the Navier-Stokes equation. Thus, the division into the inner and outer layer simplifies the solution of boundary layer problems since viscous effects are only considered in the near-surface region.

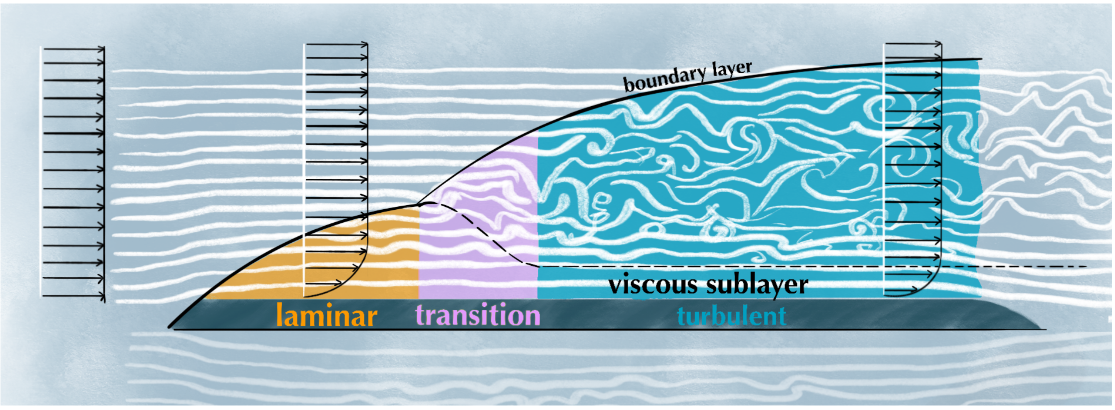

Figure 1.3.: Once a fluid encounters a surface (dark blue), a boundary layer develops in which the velocity at the plate decelerates due to viscous effects. The initial laminar stratification is disturbed by eddies, and only a viscous sublayer remains in the turbulent boundary layer in which stratification is maintained. The thickness of the hydrodynamic boundary layer (black envelop) increases due to the vortices generated. The black arrows indicate the main flow direction. Reproduced from reference [19].

At the fluid-solid boundary, a no-slip condition holds, i.e., the velocity is zero relative to the boundary. Above the boundary the fluid velocity increases until it converges to the undisturbed main stream velocity U_∞, far away from the boundary. In both cases, shear forces are caused by the velocity gradient, which is larger in the turbulent than in the laminar case.

Figure 1.4 illustrates the origin of the different velocity gradients and originates from a series of experiments in fluid mechanics performed by Abernathy [20]. The response of an incoming flow onto a flat plate is visualized using hydrogen bubbles generated by electrolysis. The bottom picture shows a laminar boundary layer; the upper flow was tripped with a wire and thus corresponds to a turbulent boundary layer. The motion in the latter case is unsteady, while the laminar boundary layer shows no interruptions. A superposition of several individual lines is shown on the right side of the image 1.4. The resulting mean velocity profile shows a larger gradient (=larger wall shear stress) for the turbulent layer than for the laminar layer.

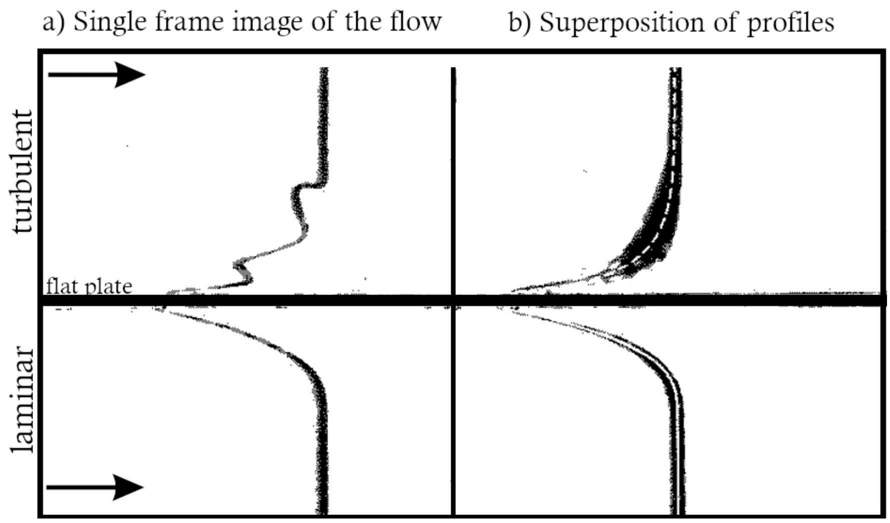

Figure 1.4.: Comparison of a laminar and turbulent boundary layer profile, visualized by hydrogen bubbles generated by electrolysis along wires perpendicular to the plate. The profiles correspond to a) a single snapshot of the flow and b) the superposition of many profiles together with the mean velocity profile. Modified for better visibility from reference [20].

The turbulent boundary layer can be described by equation (1.5). It is known as the *Kármán-Prandtl logarithmic velocity profile* or simply *law of the wall*, where κ is von Kármán's constant, u_* the shear velocity, z_0 the roughness length, U the wind velocity above a certain height z.

$$U(z) = \frac{u_*}{\kappa} \ln\left(\frac{z}{z_0}\right), \qquad \textit{law of the wall.} \tag{1.5}$$

The shear velocity, which has the dimensions of a velocity, characterizes the flow and is a measure of the shear stress τ_0 at the surface:

$$u_* = (\tau_0/\rho)^{1/2}, \qquad \textit{shear velocity} \tag{1.6}$$

with the fluid density ρ. The general validity of equation (1.5) allows us to measure the shear stress indirectly via the flow velocity [21]. For an estimation of the shear velocity, which is directly related to the shear stress as given in equation (1.6), velocity measurements at different heights are necessary. Plotting ln(z) against U(z) gives the shear velocity as the slope of the linear plot.

The thickness of the boundary layer is defined by reaching 99% of the mean stream velocity. For smooth surfaces, the thickness of the viscous sublayer in the turbulent boundary layer is approximately:

$$\delta_\nu \sim \frac{\nu}{u_*}, \qquad \textit{thickness of the viscous sublayer.} \tag{1.7}$$

Under aeolian conditions on Earth the thickness of the viscous sublayer is approximately ~0.4 mm and ~2 mm on Mars [22]. In this region, the velocity profile is linear:

$$U(z) = \frac{u_*}{\delta_\nu} z, \qquad \textit{linear velocity profile.} \tag{1.8}$$

In the turbulent boundary layer, the viscous sublayer is maintained under an aerodynamically smooth boundary but is disturbed in the presence of a rough surface. Figure 1.5 illustrates this situation. Particles induce turbulence by forming vortices, which favors the mixing of the adjacent layers and thus destroys/disrupts the viscous sublayer.

The grain-based Reynolds number describes whether a surface is hydrodynamically smooth or rough and is given by:

$$Re_d = \frac{u_* d}{\nu}, \qquad \textit{grain-based Reynolds number.} \tag{1.9}$$

The roughness of a surface is in direct relation to the roughness length z_0, given in equation (1.5). For smooth conditions, the hydrodynamic roughness is $z_0 = 0.11\delta_\nu$

and depends solely on the thickness of the viscous sublayer [12]. For particle diameters larger than $10\,\delta_\nu$ this dependence vanishes and the roughness, for fixed grains, is given by $z_0 = 0.03 - 0.1d$ [12]. A moving layer of grains, however, increases the roughness z_0 [12]. Turbulent flows are present in all natural flows.

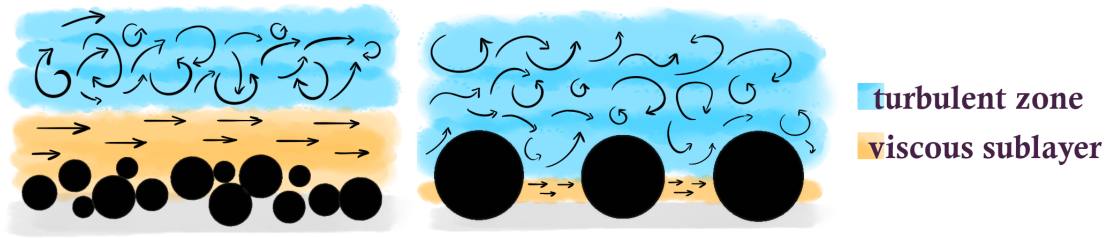

Figure 1.5.: Fluid flowing over grains lying on a surface. Left: particles with a small diameter do not disturb the flow in the viscous sublayer. The flow is said to be hydrodynamically smooth. Right: As larger particles cause turbulence, particle scale eddies disrupt the viscous sublayer. This is known as a hydrodynamically rough surface.

A laminar flow can be disturbed already by small disturbances of the surface at wind speeds of $0.1\,\mathrm{m\,s^{-1}}$. Nevertheless, this does not imply that the observed structures, both of aeolian and subaqueous nature, were always formed under turbulent flows [23]. Lajeunesse et al. [23] investigated the morphodynamics of bedforms formed underwater and showed that several laminar flow analogues of turbulent flow morphologies exist. However, for a deeper insight into the mechanism of structure formation under both flow types, some building blocks are still missing and will be addressed in the coming sections.

1.2.2. Flow over an Isolated Hill

So far, we only discussed fluids flowing over a flat surface. However, a hill or complex topography causes variations in the shear stress, which ultimately affects the erosion and growth of a sandhill. Therefore, we will provide a qualitative description of the treatment of flows over hills, allowing a better understanding of the interaction between flow and topography.

Figure 1.6 shows a simplified illustration of a fluid flowing over the hill. Bernoulli's principle [2] can be applied, assuming that the flow is incompressible and turbulent fluctuations can be averaged to a mean flow in one flow direction (streamline representation). This law is also valid for air flows since at wind speeds up to $60\,\mathrm{m\,s^{-1}}$ the compressibility of air is negligible [2].

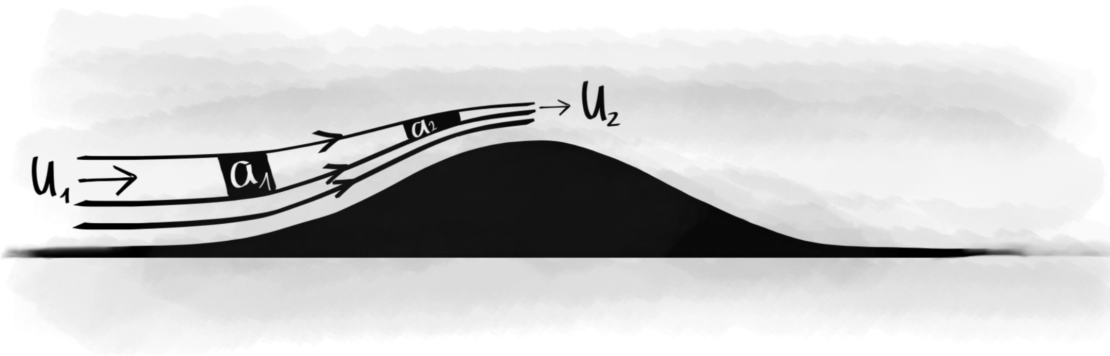

Figure 1.6.: Flow over a smooth hill. The streamlines narrow towards the crest. The fluid volume flowing from left to right with velocity U_1 passing through area a_1 must be the same as the one passing through a_2 with velocity U_2. Inspired from reference [2].

The continuity equation for this system can be described as $U_1 a_1 = U_2 a_2 = const$, obeying the law of conservation. The converging flow lines in figure 1.6 imply an increase in velocity, whereas the diverging indicate a decrease (the opposite is true for the pressure). The total pressure p_t is obtained from the sum of the static p_s and the dynamic pressure p_{dyn}:

$$p_t = p_s + p_{dyn} = p_s + \frac{1}{2}\rho U^2 = const., \qquad \textit{Bernoulli equation.} \tag{1.10}$$

As long as viscous forces dominate over inertial forces, a flow generally follows the contour of a body [24]. The higher the Reynolds number, the more inertial forces dominate over viscosity, with the result that at sufficiently high Reynolds numbers, even streamlined bodies experience a separation of the flow. A fluid flowing over a semi-cylinder develops a boundary layer due to viscous shearing in the presence of a surface, as illustrated in figure 1.7. The upper limit of the boundary layer is represented by the streamline adjacent to the surface. The previous assumption (Bernoulli effect) still holds: the flow velocity increases in the direction of the crest (highest elevation point of the hill) while a decreasing pressure gradient forms.

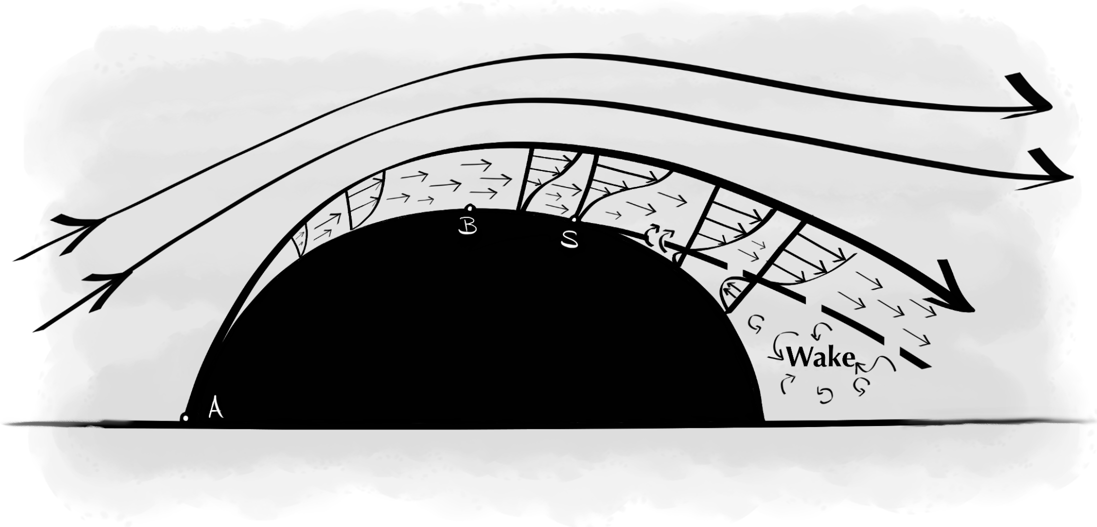

Figure 1.7.: Sketch of a fluid flowing over a semi-cylinder and the separation of flow. From point A to B: the flow accelerates, the pressure decreases and a thin boundary layer develops; the opposite is true from point B to S. At point S the flow separates, causing a reversed flow and a recirculation bubble on the downwind side of the semi-cylinder. Inspired from reference [2].

The flow can again be separated into the inner and outer flow, each affecting the other, respectively. In Figure 1.7, the velocity is lowest at point A, i.e., the static pressure is high. Along the semi-cylinder from point A to B, the acceleration of the flow comes with decreasing pressure and a thin boundary layer. After point B, the cross-section of the cylinder decreases, the flow slows down, the static pressure increases again, and the thickness of the boundary layer thickens downwind. The flow separation occurs at point S, where the retraction of the flow leads to a disappearing wall shear stress; the flow is no longer attached to the body's surface. As soon as the flow can no longer follow the profile, it detaches from its surface, and a reversed flow emerges. After a certain distance, the flow reattaches to the ground, leaving a turbulent recirculation bubble in its wake. The presence and intensity of the flow separation depend strongly on the body's geometry. For example, a flow over an ellipsoidal shape tapers downstream and is known as a streamlined body. Dunes induce boundary-layer separation, which results in a trap for sediments in the recirculation bubble.

The seminal work of Jackson and Hunt [25] lead to a deeper understanding of boundary layer flow over hills. Figure 1.8 shows the underlying concept of their analytical model for neutral flow over a rough hill: the division of the flow into a thin inner layer and the outer layer, far from the surface. On the left side of figure 1.8 three velocity profiles are sketched. U_∞ corresponds to the undisturbed free stream velocity, U_0 to the velocity in the absence of the hill, and $U_B(z)$ to the perturbed flow velocity changing with height z. The velocity profile becomes strongly curved from the outside inwards with increasing height (see figure 1.7 for comparison).

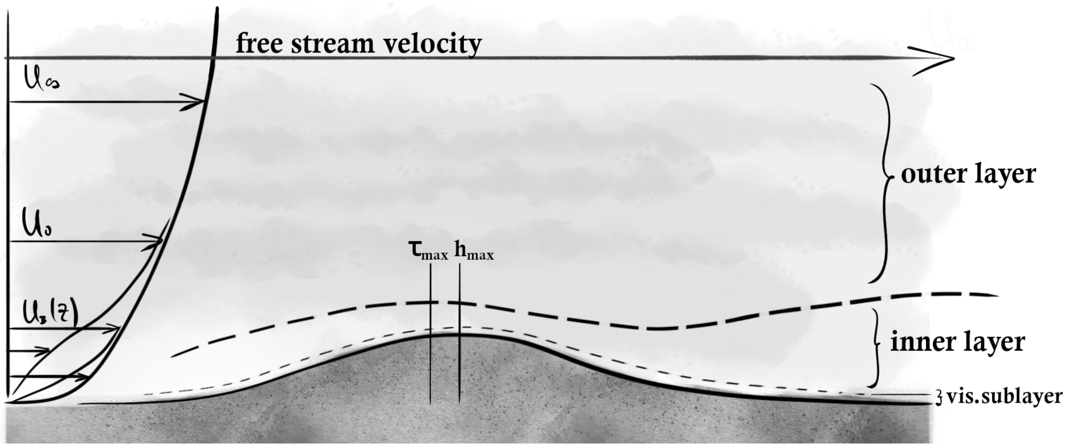

Figure 1.8.: Sketch of main regions of a turbulent flow over a hill. In the case of a hydrodynamic smooth surface, a thin viscous sublayer remains. The flow can be divided into two regions: the inner and outer layer. The shear stress maximum τ_{max} lies before the crest h_{max}. For explanations of the velocity profiles on the left side, see text. Drawn after reference [26].

The main finding was to treat the flow in the outer layer as an inviscid, irrotational velocity field dominated by fluid inertia, known as potential flow, and consider turbulent Reynolds stresses only in the inner layer. For each layer, the scaling analysis provides different leading order terms, which results in separate solutions in the inner and outer layer [25, 27]. By asymptotically matching the inner and outer layer, the overall solution gives the result that the shear stress in the inner layer reaches its maximum upstream before the crest [25]. The velocity is largest above the crest, and the streamlines follow the topography. The upstream shift of the shear stress, also measured and confirmed in the field [28], is followed by the saturation of the sediment flux with a delay [29]. In the case that the maximum saturation flux is reached before the crest, sediment deposition results in the growth of bedforms. This relationship will be discussed in more detail in section 1.4. For a deeper insight into the development in the field of boundary layer flows over complex topography, see the review by Finnigan et al. [27].

1.3. Granular Matter and Sediment Transport

Similar to the section on boundary layer theory, the research fields of granular matter and sediment transport both cover entire textbooks [3, 30–33]. The questions addressed in this section focus on those properties of granular matter that influence structure formation. We will answer the following questions in the next section:

1. What types of sediment are involved in structure formation?
2. Which forces control the dynamics of sediment transport?
3. What limits the transport of particles in a fluid?
4. What are the possible transport modes of sediments in a fluid?

After a brief introduction to the characteristics of sand, an insight into the forces acting on a particle at rest will reveal the conditions required for its transport. Once lifted by the fluid, the particle interactions with the surrounding grains and the resulting transport modes will shed light upon the preconditions leading to the instability of an erodible bed. We will introduce dimensionless parameters that simplify the comparison of sediment transport characteristics in water and air.

1.3.1. Grains and the Onset of Motion

Granular matter is a generic term for the collection of macroscopic particles that exhibit disorder at grain level but behave like a solid or fluid in aggregation [3]. Typical examples of granular media are rice, coffee, cornflakes, sand, sugar, flour, and powder, all of which share many fundamental properties. Still, there are significant differences in the type of interactions, depending on the particles' size, density, and shape, which requires further differentiation. Andreotti, Forterre, and Pouliquen [3] refer in their textbook 'Granular Media' to all particles larger than 100 µm as granular matter, whereas smaller particles with a diameter between 1 to 100 µm are referred to as powders [3].

Sand belongs to the category of granular matter and is a loose, unconsolidated material with a diameter of 62.5 to 2000 µm. Although the mineral composition is not decisive for the definition of sand, the majority in nature consists of quartz grains [2]. The origin of sand lies in physical, chemical, and biological weathering processes, in which rock fragments and the remaining loose material decompose into smaller grain sizes. We refer to the deposited grains as sediment. During transportation sedimentary grains are sorted according to their size, density, and their shape [2].

In order to interpret sedimentary bedforms correctly in a paleoenvironmental context, an understanding of the physical characteristics of individual grains and the composition of the particle population is required [2]. For example, the grain shape, its roundness, and surface texture influences the porosity and the packing distribution (see chapter 3.2 of reference [2]). Aeolian sand dunes mostly consist of moderately to well-sorted sand of size 70 to 250 µm. Silt and clay are not found in large quantities in aeolian dunes, as they tend to be entrained in suspension by the wind (see transport mechanisms in the next section) [2].

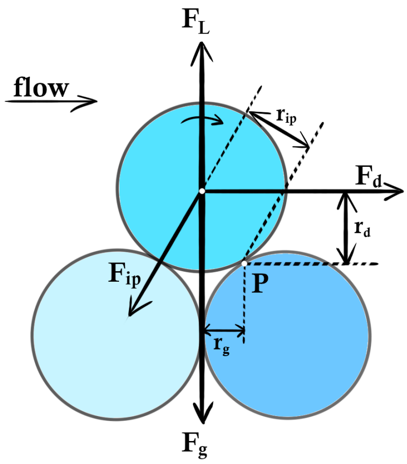

Figure 1.9.: A sand particle resting on a bed of other particles experiences four forces: gravitational F_g, and interparticle forces F_{ip} and aerodynamic drag F_d and lift F_l forces (indicated by thick black arrows). If the aerodynamic forces exceed the other two forces, the particle will first pivot around point P and then be entrained into the flow direction. Drawn after reference [22].

Whether the surrounding fluid entrains a particle or not depends mainly on the balance between gravitational, interparticle, drag and lift forces. Figure 1.9 shows a schematic of a loose grain resting on a bed of similar particles. To move a grain out of its pocket and initiate motion, the hydrodynamic lift F_l and drag forces F_d must exceed gravitational F_g and interparticle forces F_{ip} [31, 34]. The latter describes attractive forces between particles and between particles and surfaces, which arise mainly due to van der Waals interactions, electrostatic forces, and capillary bridges [3].

As soon as the hydrodynamic forces dominate, the particle begins to pivot around point P and is then entrained by the fluid. This transport is initialized whenever the fluid reaches a value above the *fluid* or *static threshold* [2, 3, 22, 35]. This threshold can be derived from the force balance at the moment of lift-off and takes the following form:

$$r_d F_d \approx r_g (F_g - F_l) + r_{ip} F_{ip} \tag{1.11}$$

where r_d, r_g and r_{ip} are the moments arms proportional to the particle diameter d_p. The effective gravitational force is given by equation (1.12) and takes buoyancy forces into account:

$$F_g = \frac{\pi}{6}(\rho_p - \rho_f) g d^3 \tag{1.12}$$

where ρ_p and ρ_f are the densities of the particle and fluid respectively and g is the gravitational acceleration. The drag forces exerted by a fluid on a particle protruding into the flow is described by:

$$F_d = K_d \rho_f d^2 u_*^2 \tag{1.13}$$

where K_d is a dimensionless coefficient (for specific values see table 3.1 in reference [31]) and u_* is the shear velocity (see equation (1.6)). The fluid threshold, first derived by Bagnold [1], is obtained by combining equations (1.11) to (1.13):

$$u_{*ft} = A_{ft} \sqrt{\frac{\rho_p - \rho_f}{\rho_f} g d}, \qquad \textit{fluid threshold} \tag{1.14}$$

where A_{ft} is a function of interparticle forces, lift forces, and the Reynolds number of the flow [31]. For loose sand on Earth, interparticle forces become negligibly small and A_{ft} is ≈ 0.1 in air and 0.2 in water [36]. There is also the dynamic threshold for saltation transport, which describes the shear velocity needed to sustain saltation after initiation. The fluid threshold is higher than the dynamic threshold in the case of aeolian saltation transport [3]. Bagnold's equation has been continuously improved and developed so that today there are various expressions based on equation (1.14) (see table 1 of reference [22]). A widely used, semi-empirical expression developed by Shao and Lu [34] includes the parameter γ, which scales with the strength of the interparticle forces:

$$u_{*ft} = A_N \cdot \sqrt{gd\frac{\rho_p - \rho_f}{\rho_f} + \frac{\gamma}{\rho_f d}} \tag{1.15}$$

where γ has a value between 1.65×10^{-4} to $5 \times 10^{-4}\,\mathrm{N\,m^{-1}}$ for dry, loose dust and sand on Earth and $A_N = 0.111$, which is close to the original value obtained by Bagnold [1, 34]. For aeolian conditions and particle sizes of about ~ 70 to $100\,\mathrm{\mu m}$, equation (1.15) yields a minimum in the parabolic curve resulting from the interparticle forces balancing the gravitational forces [34]. For grains of smaller diameter, the increasing interparticle forces, and for larger grains, the increasing gravitational forces must be overcome by the aerodynamic forces to initiate particle transport. The incipient motion can also be expressed by the dimensionless Shields number [37]. It represents the ratio between fluid forces and particle weight as a dimensionless fluid threshold:

$$\Theta \equiv \frac{\tau}{(\rho_p - \rho_f)gd}, \qquad \textit{Shields number} \tag{1.16}$$

with the shear stress τ.

1.3.2. Sediment Transport Mechanisms

The dominant transport mechanism depends on the diameter and density of the grain and the characteristics of the surrounding fluid. Sediment transport occurs close to the surface when gravitational forces dominate and confine transport to a layer close to the ground [2]. If hydrodynamic forces dominate, eddies moving through the transport layers due to turbulent flow can support the weight of the sediment, thus keeping them indefinitely in the fluid without contacting the ground. This transport mode is known as *suspension* [2]. There are three forms of trajectories resulting from bedload transport mode: saltation, reptation, and bedload [2]. Figure 1.10 shows an overview of the possible transport mechanisms.

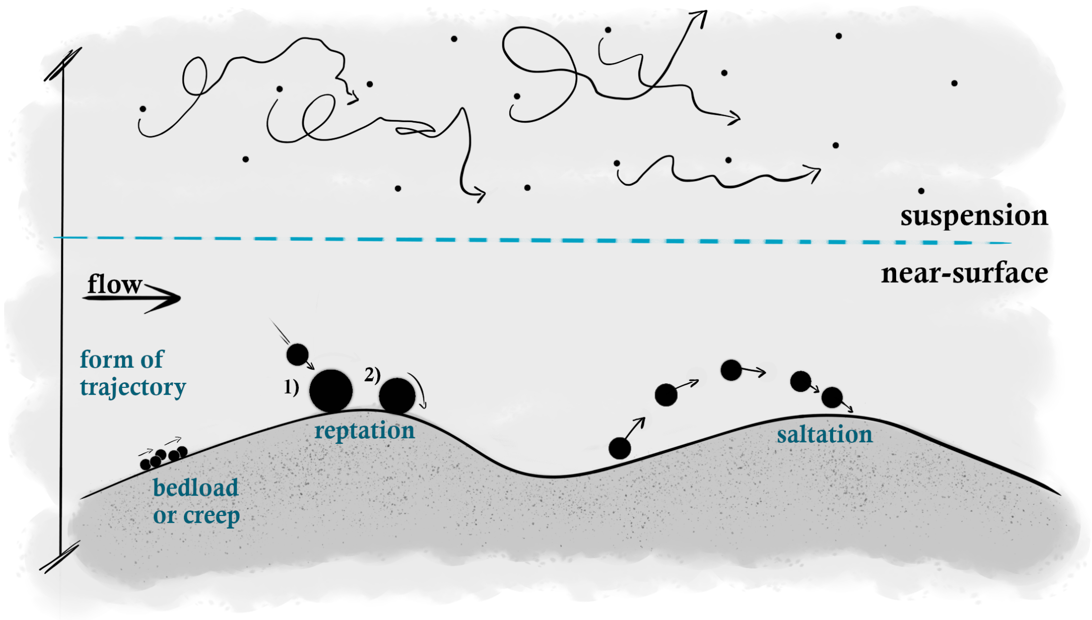

Figure 1.10.: Two different transport mechanisms, suspension and near-surface, and the possible form of trajectories close to the bed (bedload, reptation and saltation). The resulting movement of the grains depends on which forces dominate (see fig. 1.9). For a more detailed explanation see text.

Saltation is the hopping motion of particles, which follow ballistic trajectories before they impact upon the particle bed (see figure 1.11) [1]. The collision with the surface causes the impacting particle to rebound and transfer energy to other particles in the bed, resulting in their ejection. These grains release even more particles from the bed (splash effect), which ultimately results in a retardation of the wind speed (feedback effect) [38]. This complex process is the predominant transport mechanism responsible for forming aeolian dunes.

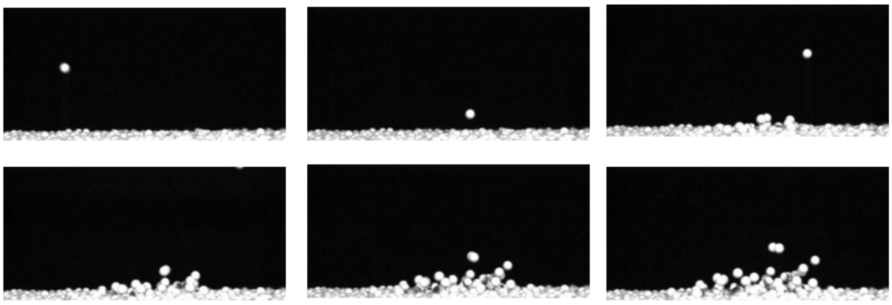

Figure 1.11.: High-speed images of a sand particle colliding with a sand bed. After the impact, the particle rebounds and splashes other sand particles from the bed. The time step between two subsequent images is 4 ms. Reprinted with permission from [39].

As soon as gravity and interparticle forces dominate, grains tend to be dragged along by the fluid and roll in direct contact with the surface on the particle bed. This type of motion is often referred to as *bedload* or *creep* in fluvial based research or as *fluid drag*, mostly in aeolian context [1, 3, 40]. The formation of subaqueous ripples is attributed to this very mechanism [3]. The same forces dominate in the case of *reptation*, which describes a creeping movement over the surface, including small hops. However, the origin of this motion type lies in the energy transfer of saltating grains that impact the bed and induce the motion to the creeping particles [1]. This type of trajectory is known to be the main cause for aeolian impact ripple formation [1].

1.3.3. The Saturation Length

In each case, the moving layer of particles leads to momentum exchange between grains and fluid and a balance of erosion and deposition. As a result, the flux of particles reaches a saturated state, the saturated flux q_{sat}. However, the mechanism controlling saturated transport differs between saltation and bedload. During saltation, energy is dissipated through collisions with other grains, and saturation is reached by statistically replacing each grain with a new grain after a collision [41]. In bedload transport, the motion of the grains takes place in a mobile layer on top of a static bed (see figure 1.12), in which the grains are at rest [3]. As a result, the fluid shear stress decreases at the interface between the two layers, resulting in a saturation once the transport threshold is reached.

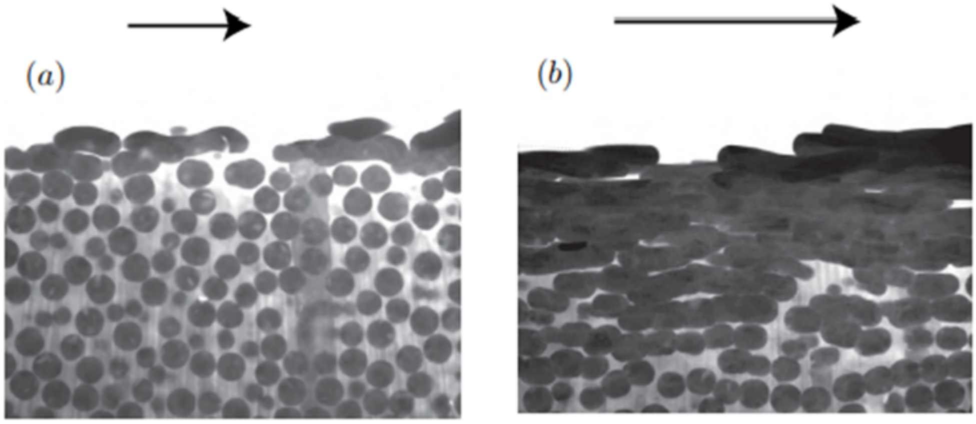

Figure 1.12.: Bedload transport near transport threshold (a) and far from the threshold (b). Once in motion, transport takes place in a mobile layer on top of the static bed. Credits: M. Pailha. Reprinted with permission from [3].

The flux does not adapt instantaneously to changes in the local shear velocity changes, so it only relaxes to its saturated value after a time t_{sat}, and a length l_{sat}, known as the saturation length l_{sat} [1, 42–47]. In practice, the flow is never far from its saturated value, and a first-order relaxation equation can model the process [43, 48]:

$$t_{sat}\frac{\partial q}{\partial t} + l_{sat}\frac{\partial q}{\partial x} = q_{sat} - q. \tag{1.17}$$

The saturation time t_{sat} is negligible compared to the time scales at which bedforms form. For this reason, we can study the hydrodynamics and sediment transport by considering the topography as fixed [12, 49, 50].

Figure 1.13 illustrates a simple method to determine the saturation length experimentally, as suggested by authors Andreotti et al. [47]. There is a fixed bed in front of the erodible bed; the wind flows from left to right. The erosion rate profile can be determined from the elevation profiles $h(x,t)$ at different points downwind at regular time intervals. The sediment flux $q(x)$ can be obtained by:

$$q(x) = -\int_0^x \partial_t h(\xi) d\xi. \tag{1.18}$$

The lower plot in figure 1.13 shows the particle flux versus distance downwind. The flux relaxes to the saturated flux after l_{sat}. Fitting the measurements to an exponential law of the form $q_{sat}(1 - exp(-(x - x_0)/l_{sat}))$ gives the saturated flux q_{sat} and the saturation length l_{sat}.

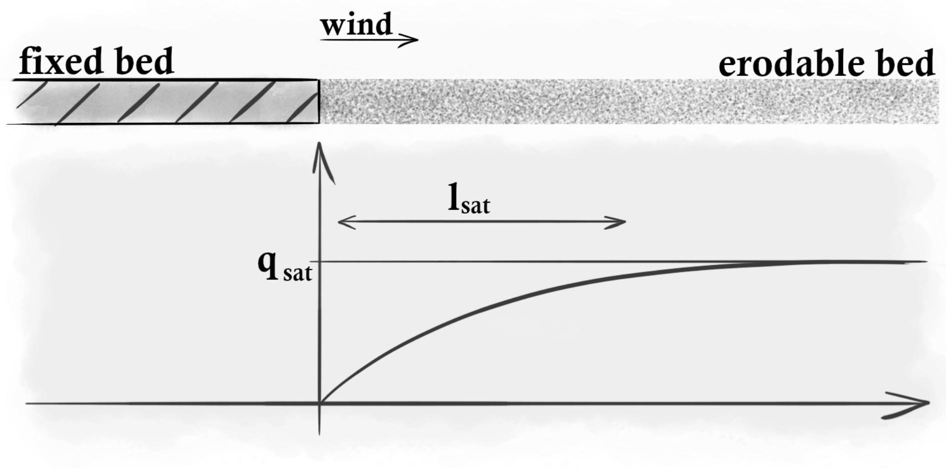

Figure 1.13.: Experimental setup to measure the sand flux as a function of space. l_{sat} is the length needed to relax to the saturated flux q_{sat}. The lower plot shows the approximate shape of q_{sat}.

There are numerical and theoretical models that reliably predict the saturation length. In particular, the equations introduced below have been tested against experimental data from the laboratory and field. Here, we distinguish between the saturation length for bedload and saltation.

An expression for the aeolian saturation length as a function of average sediment velocity in the limit of large $u * /u_t$ is given by authors Pähtz et al. [46]:

$$l_{sat}^{aeol} \approx 3 c_v V_s^2 [\mu g]^{-1} \tag{1.19}$$

with the parameter $c_v \approx 1.3$, V_s the average particle velocity towards its steady state value, the gravitational acceleration g and the Coulomb friction coefficient $\mu \approx 1$ as an empirical quantity [46]. Following this model, authors Duran Vinent et al. [10] implement this relationship in their numerical model and determine an expression that is fitted to wind tunnel and field measurements:

$$\frac{l_{sat}}{d} = \frac{a_s u_t^2}{gd} \approx a_s s \Theta \tag{1.20}$$

with Θ the threshold Shields number (eq. 1.16) and the particle-fluid density ratio:

$$s = \frac{\rho_p}{\rho_f}. \tag{1.21}$$

The calibration against experimental measurements and field data yields $a_s = 210 \pm 40$ for sand in air [10, 47]. Assuming that the particles accelerate to the wind speed by turbulent drag, the saturation length scales with the drag length:

$$l_{sat} \sim l_{drag} = \frac{\rho_p}{\rho_f} d = sd \tag{1.22}$$

where l_{drag} is the distance an entrained grain needs to reach wind velocity [48]. For subaqueous bedload, the expression for the saturation length according to Pähtz et al. [46] takes the following form:

$$l_{sat}^{subaq} = [2s+1] c_v V_s V_{rs} F [\mu(s-1)g]^{-1} \tag{1.23}$$

with V_{rs} the steady state value of the relative velocity V_r, the value F depending on V_{rs}, $c_v \approx 1.7$ and the Coulomb friction coefficient for subaqueous cases $\mu \approx 0.5$. For a detailed specification of the respective values, see reference [46].

In the numerical model of Duran Vinent et al. [10] the bedload expression is obtained by fitting the model to bedform wavelengths measured in experiments:

$$\frac{l_{sat}}{d} = \frac{a_b Re_d}{Ga^{1.2}} \tag{1.24}$$

with the particle Reynolds number $Re_d = du_*/\nu$ as introduced in section 1.2 and the proportionality constant $a_b = 140$ (for a detailed derivation of a_b, see supplement of reference [10]).

1.3.4. Dependence of Transport Onset on Transport Mechanism

The onset of grain movement depends on the transport mechanism and leads to different Shields numbers. Recently, authors Pähtz and Duran [51] studied the sediment transport threshold for an extensive range of particle-fluid density ratios and provided a general threshold diagram that applies to any environmental condition. This simplifies considerably the determination of a threshold value in environments where shear stress cannot be measured [51]. It thus provides a way to predict the transport mechanism of any particle system in any fluid. In the following, we will briefly outline the relevant parameters.

The Galileo number is introduced as a dimensionless parameter, which compares the effects of gravity to fluid viscosity and can be interpreted as a settling velocity Reynolds number [51]:

$$Ga \equiv \frac{\sqrt{(s-1)gd^3}}{\nu} = \frac{Re_d}{\sqrt{\Theta}}, \qquad \textit{Galileo number} \tag{1.25}$$

with the particle-fluid density ratio $s = \rho_p/\rho_f$, the gravitational acceleration g, the particle diameter d, the kinematic viscosity ν, the grain-based Reynolds number Re_d (eq. (1.9)) and the Shields number Θ (eq. 1.16). The combination of the Galileo number Ga and the square root of the particle-fluid density ratio $\sqrt{s}Ga$, introduced as Stokes-like number by authors Pähtz and Duran, captures the transition from bedload to saltation transport [51–53].

Figure 1.14 shows the rebound threshold Θ_t^r as a function of the Stokes-like number $\sqrt{s}Ga$ [51]. The colored code indicates the parameter S, representing the respective contribution of the hopping particles in the transport layer and thus the intensity of intergranular contacts. For saltation, the parameter is $S \geq 0.9$, as contacts are negligible, and bedload transport $S < 0.9$, since in this case, contacts become significant. The different lines correspond to various particle-fluid-density ratios s. The rebound threshold refers to the threshold value for the cessation of bulk

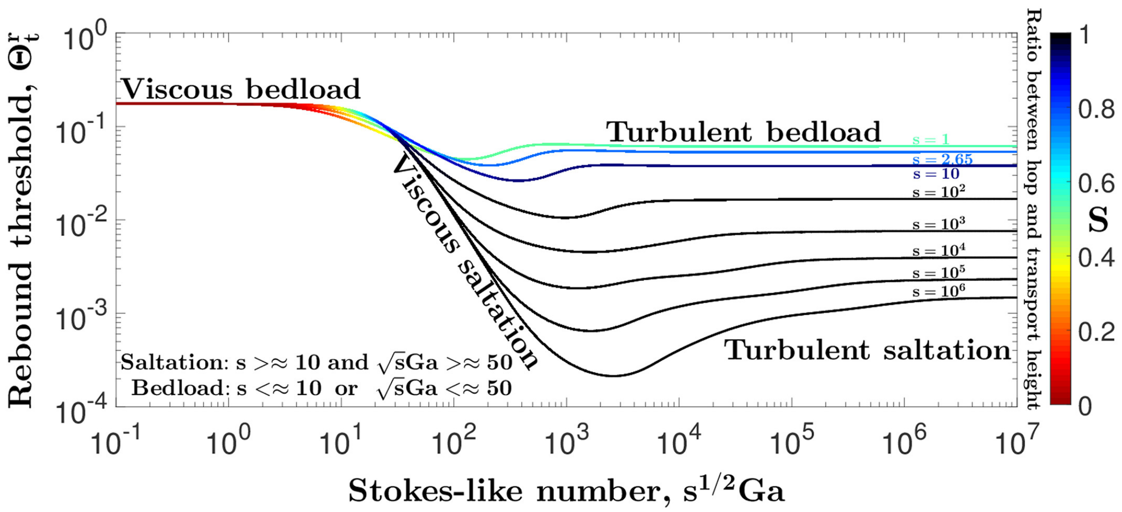

Figure 1.14.: General threshold diagram showing the rebound threshold Θ_t^r as a function of the Stokes-like number $\sqrt{s}Ga$. The colored code S represents the intensity of intergranular contact. The threshold and corresponding transport mechanism is controlled mainly by the ability of particles to hop (parameter $S \geq 0.9$ means mainly hopping movement, $S < 0.9$ corresponds to grain movement close to the bed) and the behavior of the grain in specific environments (fluid-density ratio and Galileo number). Reprinted with permission from reference [51].

sediment transport. Since the fluid loses energy due to rebounding particles, there is a minimum fluid shear stress that must be overcome to maintain transport [51].

1.4. Physics of Ripple and Dune Formation

We outlined the conditions for sediment transport mechanisms and will now discuss the formation of subaqueous bedforms and aeolian dunes. In the last section, we explained that the particle flux relaxes after a certain length, known as the saturation length l_{sat}, to its saturated flux. How does this affect the formation of bedforms? In the following, we will take a closer look at the interaction between topography and fluid flow and answer the following questions:

1. What is the fluid's hydrodynamic response to a smooth or rough topography?
2. Which characteristic length scales are involved in the formation of structures of different sizes?
3. Which morphologies emerge when structures form in a self-organized way?

Impact ripples have a different transport mechanism, as briefly outlined in section 1.3, and will be out of the scope of this thesis. The discussion refers exclusively to aeolian dunes and subaqueous ripples and dunes. From here on, we will use the term ripple to denote subaqueous ripples unless stated otherwise.

1.4.1. Instability and the Formation of Bedforms

Sedimentary bedforms are formed wherever a fluid flows with sufficiently large shear forces over an erodible bed. During this process, undulations are formed whose crests define a characteristic wavelength transverse to the flow direction. These so-called surface waves have been extensively studied in laminar [44] and turbulent regimes underwater [17, 44, 49, 54] and in aeolian environments [10, 45, 48, 55] and can be understood as linear instability.

Even over a hill with a small amplitude, the flow is disturbed and accelerates on the windward side, which increases sand flux. The shear velocity maximum lies before the crest [25], and the sand flux reaches its saturated value only after a distance l_{sat} [29, 42, 56]. Thus, we can identify two zones, which result in either erosion of the entire hump or deposition of sand and thus growth of the hump. These two mechanisms are the origin of the wavelength selection of incipient dunes.

Duran Vinent et al. [10] recently presented a model that captures bedform formation with only two dimensionless parameters: the grain-based Reynolds number Re_d and the rescaled saturation length $l_{sat}u_*/\nu$ [10]. This model provides insight into the hydrodynamic conditions to which bedforms are subjected to in different planetary environments and also allows an estimation of the possible bedforms that can emerge in laboratory experiments. In the following, the model's main aspects are outlined, based on the articles in references [10, 12, 57], unless stated otherwise.

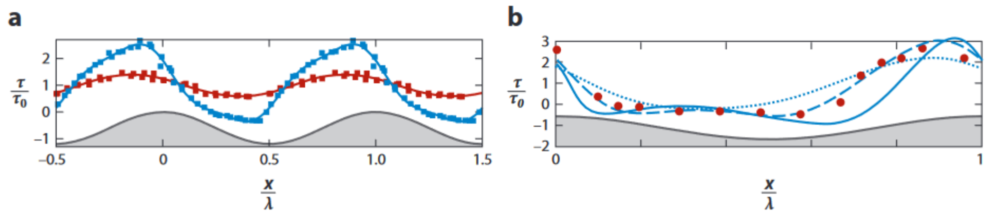

Figure 1.15.: Shear stress variation τ/τ_0 over a smooth sinusoidal bottom (*gray*) (a) Measurements for $2\zeta_0/\lambda = 0.0125$ (*red squares*) and 0.05 (*blue squares*) together with the best fit (*solid lines*). (b) Measurements for $2\zeta_0/\lambda = 0.2$ (circles) and large-eddy simulation for $2\zeta_0/\lambda = 0.0125$ (*dotted line*), 0.1 (*dashed line*), and 0.2 (*solid line*). Reprinted with permission from reference [12], see references therein for details.

For a wavy surface of the form $\zeta = \zeta_0 cos(kx)$, the response of the disturbed flow for weak amplitudes ($k\zeta_0 < 0.1$) is sinusoidal. The flow shows a linear response and is phase-shifted compared to the topography [12]. This shift is a direct effect of the viscous forces causing the shear stress to be phase-advanced and peak upstream of the crest, as discussed in section 1.2.2. The shear stress τ_b is described by:

$$\tau_b = \frac{1}{2}(\hat{\tau}e^{ikx} + \hat{\tau}^* e^{-ikx}), \qquad \hat{\tau} = \tau_0(\mathcal{A} + i\mathcal{B})k\zeta_0 \tag{1.26}$$

with the bottom shear stress τ_0, with the hydrodynamic coefficients $\mathcal{A}$ and $\mathcal{B}$ are functions of the wavenumber $k = 2\pi/\lambda$ [12, 29, 49, 57–59]. They are generically positive, which indicates that the shear stress over a topography is greater than over a flat surface ($\mathcal{A} > 0$), and the maximum shear stress is located upstream of the crest ($\mathcal{B} > 0$) [3]. The response of the shear stress to a wavy topography is shown in figure 1.15. The symbols denote measurements; the lines are fitted. There is a direct linear response for gentle slopes (a), and for larger slopes (b), harmonics grow, and the phase advance decreases. This phase advance is independent of the type of flow (turbulent or laminar) and arises close to the bed in the inner layer due to viscous effects (see section 1.2) [12]. $\mathcal{A}$ and $\mathcal{B}$ depend only on the parameter kz_0, i.e., on the ratio of roughness length to wavelength, assuming that the vertical extent of the fluid is much larger than the penetration depth of the flow disturbance.

Figure 1.16 shows measurements and theoretical predictions of the two shear stress components; four different hydrodynamic regions are distinguished depending on kz_0: viscous, inertial, transitional, and the turbulent regime [10]. The shear stress modulation over a sinusoidal bottom shows a distinct transition between the laminar regime, i.e., at small wavelengths and large wavenumbers, and the turbulent regime, vice versa ($10^{-5} < kz_0 < 10^{-3}$). Experimental data (blue and green symbols) confirm the predicted model in the limit of $\mathrm{Re}_d = 0$ (black) and $\mathrm{Re}_d \to \infty$ (blue). The inset in figure 1.16 shows the phase shift $\tan^{-1}(\mathcal{B}/\mathcal{A})$ in degrees, which is positive for almost all kz_0. The phase becomes negative within a narrow range, which will be discussed a few paragraphs further down.

This result can be interpreted as follows: at small wavelengths, the flow disturbance can be confined close to the surface, and turbulent fluctuations can be neglected [12, 24, 61]. This applies to laminar flows but also to the viscous sublayer in turbulent flows. In this case, the inner layer is equivalent to a thin layer close to the surface and is dominated by viscous stresses. In the outer layer, where inertia dominates, the flow is treated as a potential flow (see sec. 1.2.2). The thickness of the inner layer δ_i is approximately:

$$\delta_i \approx \left(\frac{\delta_\nu^2}{k}\right)^{1/3} \tag{1.27}$$

with the viscous length $\delta_\nu = \nu/u_*$. In the turbulent regime, i.e., large wavelengths, Reynolds stresses have to be taken into account, and the flow disturbance takes place far beyond the surface, resulting in a much thicker inner layer. A recent finding confirmed that this is true for both smooth and rough hydrodynamical roughness z_0 [57]. The transitional regime is between the two regions, where the disturbance partially penetrates the turbulent region, so neither viscous nor turbulent effects can be neglected. In this regime, there is a region where the maximum shear stress shifts from upwind to downwind ($\tan^{-1}(\mathcal{B}/\mathcal{A}) < 0$). This is referred to as a hydrodynamic anomaly by authors Duran Vinent et al. [10] and corresponds to the transition of the disturbed flow from laminar on the upwind to turbulent on the downwind side, as the streamlines diverge and turbulent fluctuations amplify. Thus, the inner layer periodically changes from viscous to turbulent.

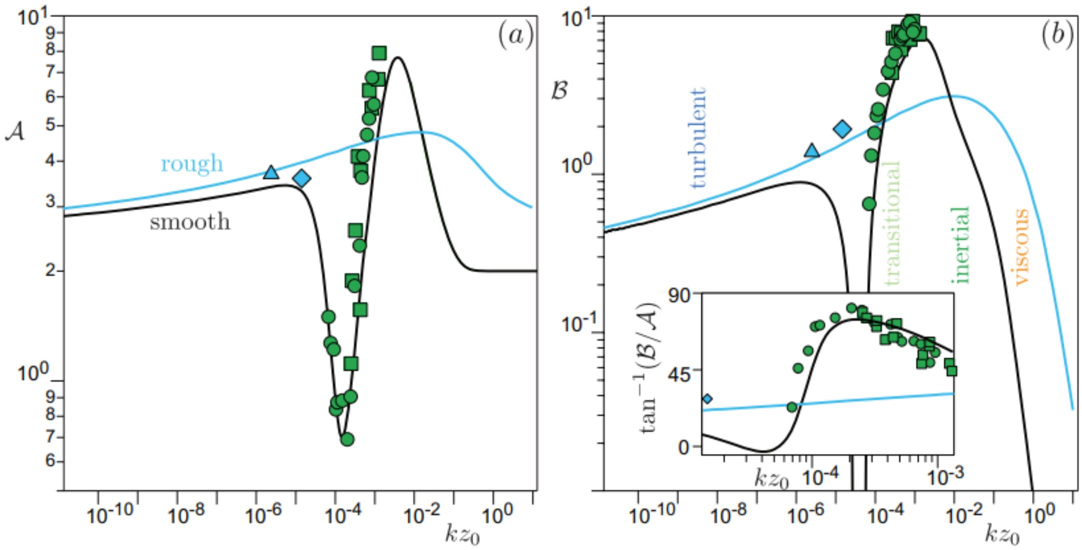

Figure 1.16.: Shear stress components of the shear stress modulation over a sinusoidal bed (a) in-phase $\mathcal{A}$ and (b) in quadrature $\mathcal{B}$ as a function of wave number k rescaled by the hydrodynamic roughness z_0; (inset) phase shift $\tan^{-1}(\mathcal{B}/\mathcal{A})$ in degrees. Symbols: green from experiments in the hydrodynamic smooth regime [58, 59] and blue in the rough case [28, 60]. The solid lines are predictions of the proposed model by Duran Vinent et al. [10] in the limit of $R_d = 0$ (black) and $R_d \to \infty$ (blue). For further explanation, see text. Reprinted with permission from reference [10].

These complex dynamics are illustrated in a simplified scheme in figure 1.17. Figure 1.17 shows a fluid's hydrodynamic response to a smooth and rough topography. The flow schematics are arranged in the plane spanned by the grain-based Reynolds number Re_d and the wavelength Reynolds number $\mathrm{Re}_\lambda = \lambda u_*/\nu$; the fluid flows from left to right. On the far left, the respective hydrodynamic response is shown: from bottom to top, the wavelengths increase, which means that the structures become larger and go through all responses from viscous to turbulent in the hydrodynamically smooth case. A viscous response is not possible if the surface is rough since larger particles cause eddies on a particle scale and disturb the viscous sublayer (see figure 1.5). The orange-colored region indicates the dominance of viscous stresses, the color blue in this scheme represents dominant Reynolds stresses. The outer layer is drawn in green above the inner layer in each image (except in the viscous case at the bottom left).

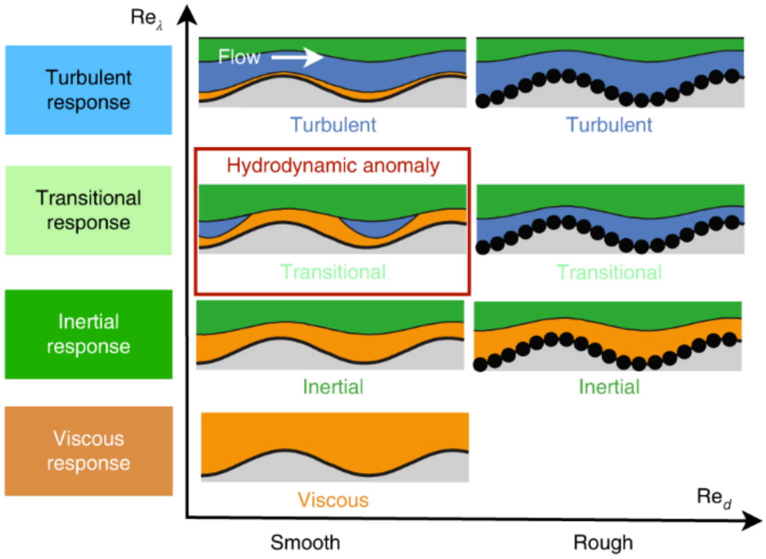

Figure 1.17.: A schema showing the layered hydrodynamic response to the bed topography as a function of $Re_\lambda = \lambda u_*/\nu$ and $\mathrm{Re}_d = u * d/\nu$. The colors represent the dominant hydrodynamic mechanism that balances the pressure gradient modulation: viscous diffusion (*orange*), inertia (*green*) or turbulent fluctuations (*blue*). The thickness of the layers is not to scale. Reprinted with permission from reference [10].

We have outlined the hydrodynamic response of the fluid to a smooth and rough topography, but which characteristic length scale affects bedform formation? Bedforms exposed to a fluid undergo continuous changes due to sediment transport. The saturation of the particle flux does not occur instantaneously, is sensitive to changes in shear stress, and adapts with a delay, as described in section 1.3. Figure 1.18 illustrates how the position of the shear stress shifted upwind results in the offset of the maximum transport rate with respect to the highest point of the hill, the crest. This longitudinal instability drives bedform evolution [56]. The distance δ_τ between the crest and the maximum bed shear stress is proportional to the wavelength of the bedform and must be greater than the saturation length for a sand hill not to be completely eroded. The growth conditions are thus given

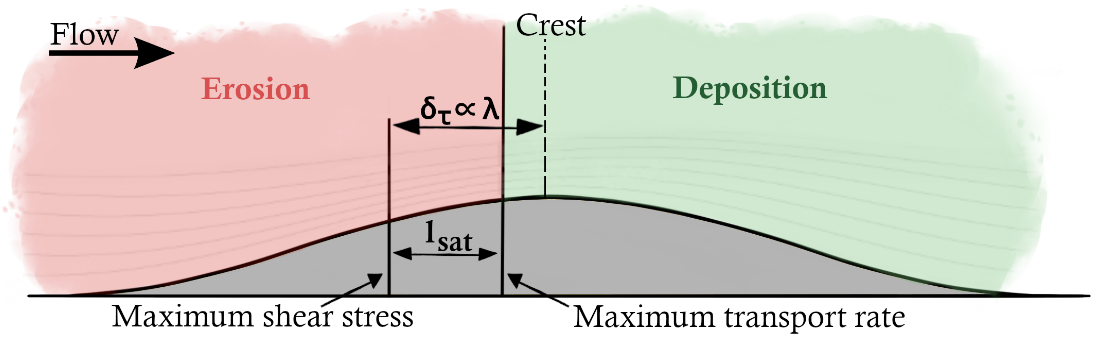

Figure 1.18.: Flow over a hill (grey). The condition for bedform growth is fulfilled for $\delta_\tau > l_{sat}$. The maximum shear stress is positioned upwind; the spatial relaxation of the maximum transport rate takes places after a length l_{sat}. The shift of the maximum bed shear stress to a downwind position and thus $\delta_\tau < l_{sat}$ leads to the erosion of the hill. Redrawn after reference [10].

by $\delta_\tau > l_{sat}$. The hydrodynamic anomaly described previously corresponds to the displacement of the maximum shear stress downstream and results in a cessation of bedform growth and thus $\delta_\tau < l_{sat}$. However, this condition is only relevant for the hydrodynamically smooth case, as rougher surfaces generate particle-scale turbulent fluctuations, precluding any viscous response.

Figure 1.19 shows a phase diagram of ripples and dunes as a function of the dimensionless parameters [10]. We will introduce the terms ripples and dunes in the next section. Planetary conditions are shaded; experimental points show water and water-glycerol mixture and aeolian data. The wavelengths at which bedforms emerge in different environments under the action of various fluids depend on the grain-based Reynolds number Re_d and the saturation length rescaled by the size of the viscous sublayer, $l_{sat}u_*/\nu$. The first threshold results from the smooth-rough transition at about $\mathrm{Re}_d \approx 20$ and the second from transport relaxation, which stabilizes ripples ($l_{sat}u_*/\nu \approx 10^3$). Both thresholds determine the appearance of ripple-like or dune-like structures. In diagram 1.19, the respective grain-based Reynolds numbers were corrected for the data points to include transport effects (see in detail supplementary material of reference [10]).

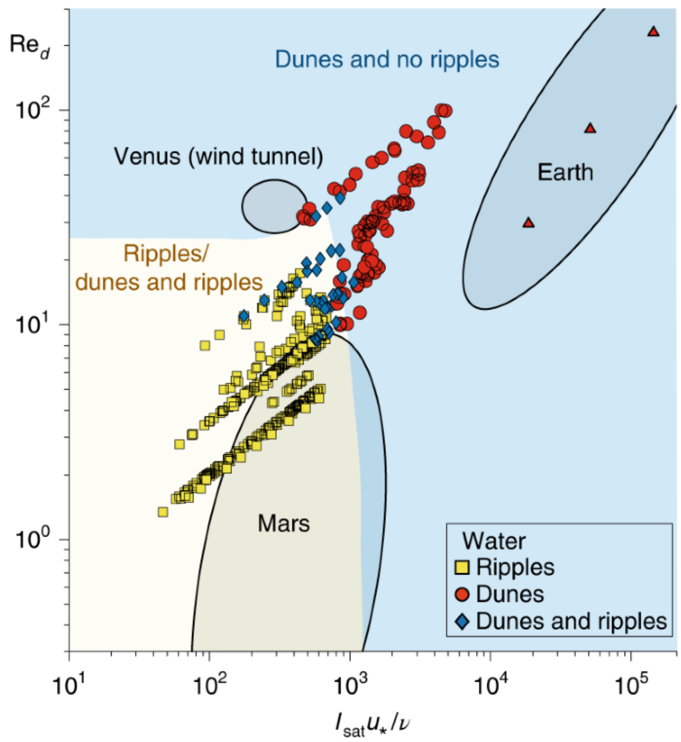

Figure 1.19.: A diagram of ripples and dunes in various environments as a function of the rescaled saturation length $l_{sat}u_*/\nu$ and the grain-based Reynolds number Re$_d$, which is corrected to include transport effects (for details see attachment of ref. [10]). The yellow area shows conditions for the presence of ripples and dunes; in the blue area only dunes are possible. The symbols correspond to water and water-glycerine mixture data (squares, circles, diamonds) and aeolian Earth data (triangles; initial dunes); both for monodisperse sand. To denote the range for different planetary conditions, the areas are shaded. Reprinted with permission from reference [10].

Figure 1.19 shows that bedforms with small wavelength Reynolds number Re_λ are governed by the same physics independent of the surrounding fluid and even of the planetary environment. Some Martian bedforms are analogous to subaqueous ripples. The size of these Martian bedforms and subaqueous ripples is selected by the thickness of the viscous sublayer ν/u_*. Sediment transport is confined within this layer, and the grains are mostly in contact with the particle bed. We introduced this transport mechanism earlier as bedload (see section 1.3). As soon as the response becomes turbulent, the grains' motion range is not restrained to this thin layer close to the bed surface, as eddies can lift the particles from the bed. The transport layer differs for bedload and saltation, from a few micrometers to several centimeters in air. In contrast to ripples, the minimal size of dunes scales with the saturation length l_{sat}, which has been independently measured and modeled [47, 56, 62].

The morphodynamics described above in terms of instability is only valid for the onset of formation. Once a mature bedform is formed, non-linear processes are at work that can no longer be described by linear stability analysis [12]. During the growth phase, an aspect ratio of the bedform is reached where the non-linear hydrodynamic response leads to the formation of a recirculation bubble (see section 1.3) [12].

1.4.2. Bedforms under Unidirectional Flow

We encounter sedimentary bedforms of various sizes, which challenges the traditional terminology to distinguish ripples from dunes. Ripples are said to be those bedforms that are centimeters in size, as opposed to dunes, which can range from a few to hundreds of meters [2]. However, we observe bedforms of different sizes on planets such as Mars or Venus, in laboratory experiments underwater and pressurized wind tunnel [4, 63–68], some of them with ripple length scales and the morphology of meter-sized dunes and mid-sized Martian bedforms, whose origin is still ambiguous.

Based on the work of Duran Vinent et al. [10], the structures that trigger a turbulent response will be referred to as dunes in this thesis. All other bedforms will be termed as ripples since their scale of the maximum size is determined by the size of the viscous sublayer $\nu/u*$ [10]. We still exclude impact ripples in this description because a different transport mechanism governs them (reptation, for detail, see section 1.3).

Dunes show a variety of morphologies, depending on the sediment availability and the direction of the incoming fluid. The most studied dune is crescent-shaped and evolves under unidirectional flow and low sand availability. The structure is known as a barchan and owes its name to the Turkmen word for crescent dune (figure 1.20). A characteristic feature of a barchan are the horns, which point in the direction

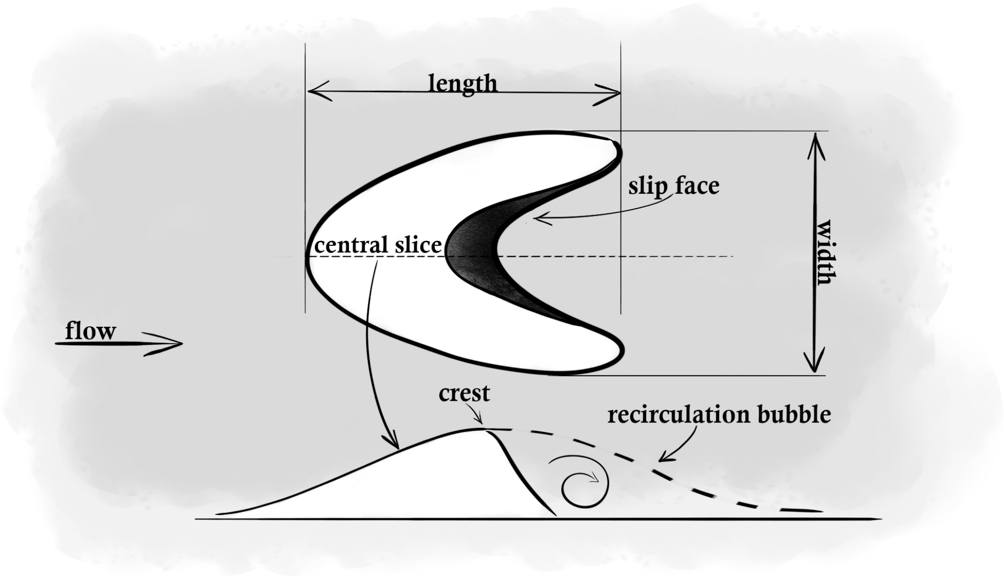

Figure 1.20.: The characteristic features of a barchan: a crescent-shaped bedform, with two horns pointing in the migration direction and a slip face, where sand avalanches and is trapped by the recirculation bubble that occurs due to flow separation. Figure inspired by Hersen [69] and Courrech du Pont [70].

of migration. On the windward side (luv), sand is transported uphill. As soon as the sand pile reaches the angle of repose, avalanches of grains slide down on the lee side, and a sharp dune crest is formed. For medium-fine sands, the angle of repose varies from 30.5 to 35.5°, but is typically 32–3° [2]. As a result, the entire amount of sand from the original sand heap is redeposited over time, resulting in the dune's forward migration.
The time it takes a dune to travel its length is also known as the turnover time [1]. It was shown by the authors Parteli et al. [62], that the minimal dune width W_{min} is approximately $12l_{sat}$ [62], which gives a minimal size of ~10 meters for aeolian barchan dunes.

Elbelrhiti et al. [55] gave an expression between the elementary size of a mature bedform and the saturation length:

$$\lambda_{max} \sim 12l_{sat}. \tag{1.28}$$

In this thesis, we will refer to all bedforms that share the morphological characteristics of barchan dunes as barchans. This form occurs in all sizes and under different conditions, as shown in figure 1.21. The bedforms shown in figure 1.21 were all formed under laboratory conditions, either in water tanks or in wind tunnels. The captions give details about the setup and material used in these experiments.

As it is the central topic of this work, emphasis has only been put on the description of barchans. However, winds often flow from several directions, affecting the mobility and morphology of bedforms. For an overview, see references [2, 31, 71].

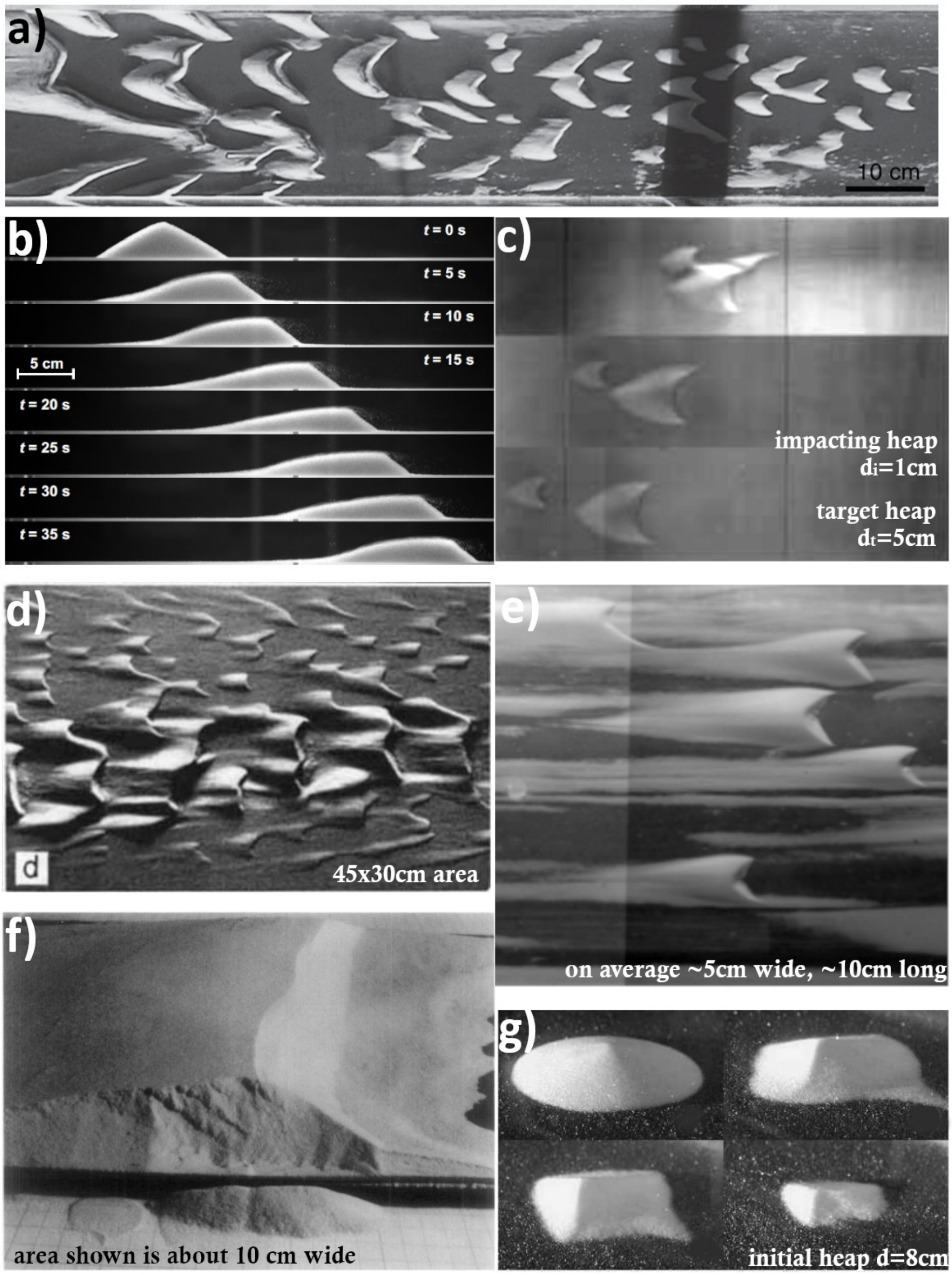

Figure 1.21.: Various bedforms that formed in laboratory experiments under water (a-e) and in air (f,g) in unidirectional flow. (a) 'Barchan-shaped ripples' formed in a recirculating flume out of a flat sand bed with 3 mm thickness. Material: 100 µm well sorted sand [72]. (b) 'Barchan dune slices' in a 6 mm wide channel, to approximate two-dimensional conditions. Material: 560 to 600 µm glass beads [73]. (c) Collision of two different sized subaqueous dunes. Material: 150 µm sized glass beads [74]. (d) 'Bedforms' formed in a recirculating flume out of a flat sand bed with 1 cm thickness. Material: 66 µm sized 'natural fluvio-glacial sediment' [75]. (e) 'Beds of quartz silt' formed in a rectangular tilting flume. Material: 'crushed rock', quartz grains of 4.15 µm size [76]. (f) 'Microdunes' formed in the Venus Wind Tunnel simulating the average Venusian environment. Material: quartz sand of 50 to 200 µm range [65]. (g) "Barchan' dunes' formed in a ambient wind tunnel. Material: mono-dispersed sand of 250 µm diameter [68]. Figures are reprinted with permission of references given in the respective description.

1.5. Conclusion for the Experimental Study

We introduced the basic principles of structure formation that will allow us to understand this work's key ideas and results. With this understanding of the basic concepts of structure formation, we will now motivate our work in more detail and present the conditions under which we can observe migrating aeolian bedforms in the laboratory.

Ripples and dunes have been studied in water tanks [44, 66, 67, 72, 74, 77–79] and in high pressurized wind tunnels [64, 65, 80]. These laboratory studies enabled the calibration of theoretical and numerical models that allow us to understand the formation of bedforms and the underlying physics of a variety of structures on Earth, Mars, Venus, and other celestial bodies [10, 33].

Recently, Martian bedforms were reported to be analogous to subaqueous ripples [8, 10, 81]. This hypothesis is still under debate since the conditions under which these structures develop are quite different. Duran Vinent et al. [10] propose that these Martian bedforms are similar to subaqueous ripples, and that the thickness of the viscous sublayer determines their scale [10], as presented in section 1.4. In contrast, Sullivan et al. [11] show in numerical simulations that the proposed mechanism is not necessary to explain the range of observed bedform wavelengths' on Mars and that these structures are similar to aeolian impact ripples [11]. The ongoing discussion underlines a knowledge gap: the transport mechanism that is thought to be responsible for the formation of Martian bedforms has not been studied under aeolian conditions on Earth.

The proposed universality of the models of Duran Vinent et al. [10] suggests that the same structures that form on Mars and are compared with subaqueous ripples should also be reproducible under aeolian conditions on Earth. However, the study of aeolian viscous bedload structures in nature remains relatively unexplored to this date [8]. This is owed to the characteristics of sand found in the field, and the viscous sublayer thickness in a turbulent boundary layer, which is approximately 0.4 mm [22]. Only fine sand could potentially be transported in the viscous sublayer. However, due to cohesive effects, the fluid threshold is high enough to directly entrain the grains in suspension, like dust in deserts. Saltation and reptation typically dominate as transport mechanisms. For aeolian viscous bedload transport, the grains would have to be small and light enough to be transported in the viscous sublayer without going immediately into suspension. A condition that is not found predominantly in natural environments on Earth.

Our approach is to access this area in a laboratory experiment. In section 1.3 we introduced the general threshold diagram by Pähtz and Duran [51], a diagram with which we can predict the transport mechanism of any particle system in any fluid. Figure 1.22 shows the general threshold diagram again, with an outlined area in red that we will discuss in more detail below.

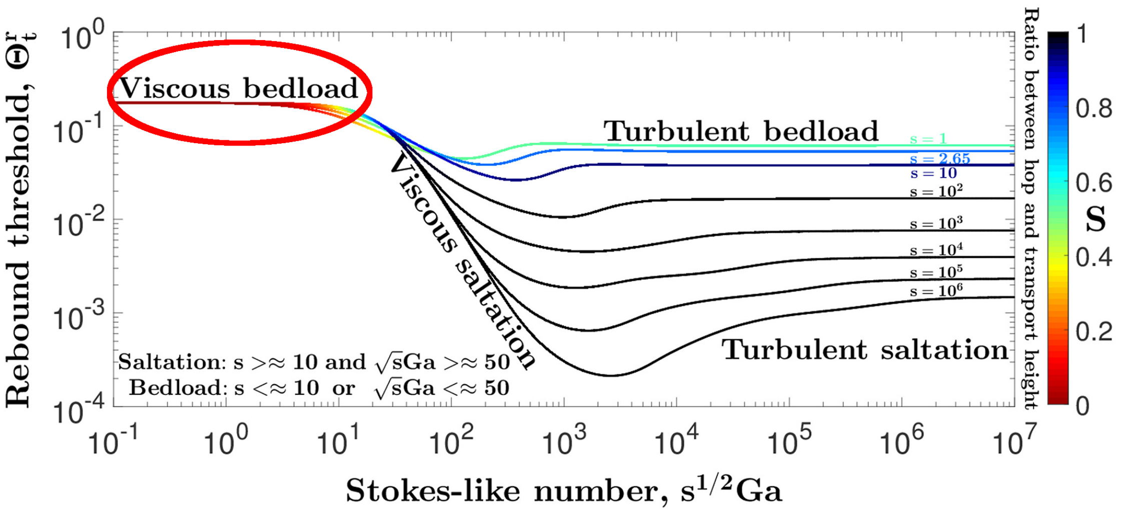

Figure 1.22.: General threshold diagram as introduced in figure 1.14 and the transport regime we want to access, marked in red. Reprinted with permission from reference [51].

For the viscous bedload transport mechanism to be accessible under aeolian conditions, the Stokes-like number $s^{1/2}Ga$ must be less than 50. The key parameters for the selection of the particle system are the particle-fluid density ratio s (eq. (1.21)) and the Galileo number Ga (eq. (1.25)). We fix the fluid density and kinematic viscosity value, as we want to perform our experiments in aeolian ambient air conditions. In addition, the diameter of the particles should not exceed 50 µm, for reasons that will be explained further below. Combining both equations and performing minor manipulations lead us to the following relation:

$$\frac{50^2 \cdot \nu^2}{g \cdot d^3} = s(s-1). \tag{1.29}$$

From this, we calculate a maximum density value ρ_p of $800\,\mathrm{kg\,m^{-3}}$, which must not exceed to stay in the viscous bedload regime. The rebound threshold that results for viscous bedload lies between $0.1 < \Theta_t^r < 0.2$. The threshold Shields number is $\Theta_t > 2\Theta_r^t$ for viscous bedload [53], resulting in a value between $0.2 < \Theta_t < 0.4$. From this, we approximate the shear velocity needed in the wind tunnel to enable sediment transport:

$$u_* = \sqrt{\Theta \cdot [(s-1)gd]} \approx 0.25 \text{ to } 0.36\,\mathrm{m\,s^{-1}}. \tag{1.30}$$

As described in section 1.4, the grain-based Reynolds number Re_d and the rescaled saturation length $l_{sat}u_*/\nu$ are two dimensionless parameters which cover the characteristics of bedform formation. With the values given above, we can calculate these characteristic length scales and provide an approximate size of the structures that we expect to form in the wind tunnel:

$$\mathrm{Re}_d = \frac{u_* d}{\nu} = \frac{0.3\,\mathrm{m\,s^{-1}} \cdot 50\,\mathrm{\mu m}}{14.5\,\mathrm{\mu m^2\,s^{-1}}} = 1 \tag{1.31}$$

with a shear velocity of $0.3\,\mathrm{m\,s^{-1}}$ in between the desired range and a saturation length for viscous bedload after equation (1.24):

$$l_{sat} = \frac{a_b\,\mathrm{Re}_d\,d}{Ga^{1.2}} = \frac{140 \cdot 1 \cdot 50\,\mathrm{\mu m}}{2^{1.2}} = 3\,\mathrm{mm}. \tag{1.32}$$

The initial wavelength of the structures scales with the thickness of the viscous sublayer ν/u_* (see section 1.4). The bedforms are therefore expected to be centimeters in size. For mature subaqueous ripples and aeolian dunes, the height-to-length ratio is approximately 1/15 [12, 82, 83], which should then result in bedforms with a height in the millimeter range. Table 1.1 summarizes the relevant dimensionless parameters and potential particle system values.

The wind speed must be low enough to form a viscous sublayer in the turbulent boundary layer. For this, the surface of the test area of the wind tunnel should be in the hydrodynamically smooth regime. At the same time, the wind speed must be high enough to allow sediment transport. With a mean threshold of $u_* = 0.3\,\mathrm{m\,s^{-1}}$ obtained above, the thickness of the viscous sublayer is estimated to be:

$$\delta_\nu \sim \frac{\nu}{u_*} \sim 70\,\mu\mathrm{m}. \tag{1.33}$$

Thus, the choice of the particle system is 1) limited by this diameter, as bigger particles will be entrained into suspension, and 2) the commercial availability. In size ranges below 100 µm, we expect increased cohesive forces, which raise the fluid threshold [34]. As a countermeasure, we will need to coat the particles to reduce cohesion [32], and still keep low wind velocities. The test area should be at least 30 cm long in wind direction to be able to observe migrating structures.

Under the conditions specified above, we expect the formation of self-organized structures, specifically ripples, in the wind tunnel in which the particles are transported within the viscous sublayer. In a previous study, a particle system was investigated in a laboratory wind tunnel that satisfies the required conditions [84]. In the next chapter, we will present this particle system and introduce the wind tunnel used in this work.

Parameters	Notation	Value	Unit
Fundamental parameters			
Gravitational acceleration	g	9.81	$\mathrm{m\,s^{-2}}$
Fluid density	ρ_f	1.2	$\mathrm{kg\,m^{-3}}$
Kinematic viscosity	ν	$1.45 \cdot 10^{-5}$	$\mathrm{m^2\,s^{-1}}$
Required parameters			
Particle density	ρ_p	800	$\mathrm{kg\,m^{-3}}$
Particle diameter	d	50	µm
Shear velocity threshold	u_t	0.25-0.36	$\mathrm{m\,s^{-1}}$
Viscous sublayer thickness	δ_ν	≈ 70	µm
Dimensionless parameters			
Particle-fluid density ratio	s	666	
Grain-based Reynolds number	Re_d	1	
Galileo number	Ga	2	
Stokes-like number	$\sqrt{s}\mathrm{Ga}$	>50	
Threshold Shields number	Θ_t	0.2-0.4	
Predicted parameter			
Saturation length	l_{sat}	≈ 3	
Wavelength	λ	$\approx 3 - 4$	cm
Height	h	≈ 3	cm

Table 1.1.: Summary of the characteristic parameters of the experimental setup: fundamental parameters relevant for calculating the dimensionless and predicted parameters and the required values for the experimental setup to access the aeolian viscous bedload transport regime.

2 Characterization of the Experimental Setup

Light microscopy image of hollow glass microspheres

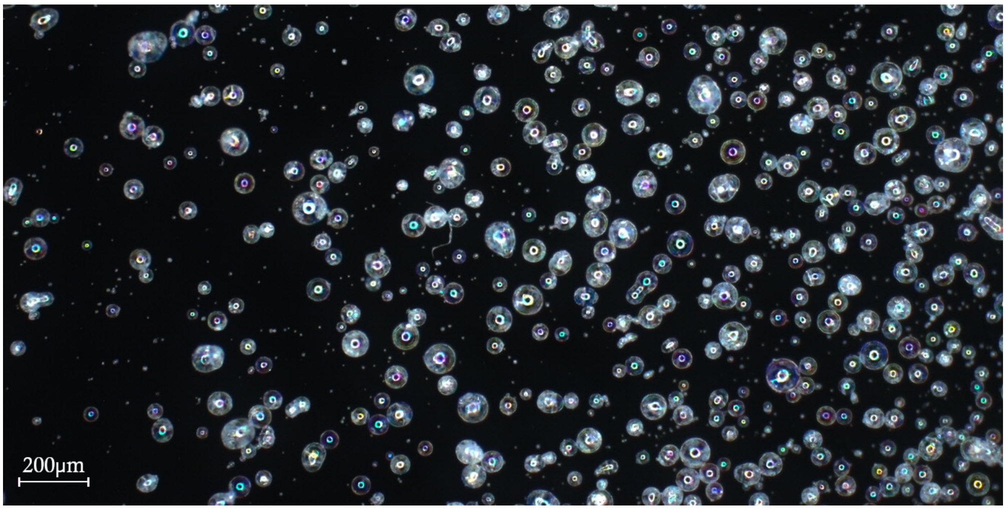

'It appeared to me, therefore, that a research into sand-dune formation should best be divided into two stages. The first stage should comprise laboratory work with a suitable wind tunnel, by means of which an insight would be gained into the physics of the action of the air stream on the sand grains and of the reaction of the sand grains on the air stream.'

R.A.Bagnold (1941)

2.1. Overview

A suitable particle system and setup are needed to access the aeolian viscous bedload transport regime in the laboratory. We will characterize a setup that satisfies the requirements specified in section 1.5. The first section covers the basic properties of the chosen particle system, such as density, particle diameter, and characteristic dimensionless quantities, together with a protocol for material preparation and microscopy images that will demonstrate the advantages and disadvantages of the particle system.

Subsequently, a characterization of the wind tunnel follows. After describing the design, the required equipment, and the methods used for characterization, we will provide an overview of achievable operating speeds and the wind velocity distribution above the test surface. Finally, the derivation of characteristic parameters from the wind profile will provide information about the investigation regime and its limitations.

By the end of this chapter, two questions will be answered:

1. Which particle system is suitable for observing aeolian viscous bedload structures in the wind tunnel?
2. What type of wind tunnel is needed to enable transport in the viscous sublayer for the selected particle system?

2.2. Particle System

Manufacturers offer a spectrum of different materials with various particle densities and sizes for industrial use, e.g., the food, cosmetic, paint or pharmaceutical industry [32]. They are added in large quantities to the base material in order to change its physical properties [85]. This abundance of different materials provides the opportunity to find a particle system that combines small grain diameters with low densities. For our investigation purposes, we need a material that has a diameter of about 50 µm and a density lower than 800 kg m^{-3}. Only this combination limits the transport mechanism to viscous bedload, as discussed in section 1.5.

We introduce a particle system that satisfies the conditions set in section 1.5. The particles have a diameter of 43 µm and a density of 238 kg m^{-3}. Previous studies investigated these particles under aeolian exposure and concluded that the coating with a flow control agent reduces the attractive interparticle forces and has a positive effect on the flow behavior [84, 86]. We perform the ideal coverage calculation and provide a detailed material protocol, which includes the optimal preparation of the particle system. With light microscopy images, we will show the material's sensibility to prolonged exposure to ambient air and its tendency to tribocharge. Finally, the calculation of the characteristic parameters will give us an estimate of the expected bedform sizes.

2.2.1. Hollow Glass Microspheres

Hollow glass microspheres (HGMs) are spherical glass particles of between 10 to 200 µm with a wall thickness of 0.5 to 2 µm [87]. Due to the cavity, the particles have low densities of 70 to 400 kg m^{-3} [87]. HGMs are powders whose flow behavior is reminiscent of a liquid. The properties of this class of particles match nicely with our desired particle type. For this work, we use HGMs produced by PQ Corporation under the brand name Q-CEL® 5020FPS and are distributed in Germany by Lehmann & Voss & Co.KG. For the coating of the HGMs, we use a flow control additive.

2.2.2. Flow Control Additive

Interparticle forces strongly influence the bulk behavior of powders [88]. Van der Waals forces, capillary forces, and electrostatic forces can significantly influence the flow properties [88]. To decrease interparticle attractive forces, the HGMs have been coated with nanometre size particles, called flow control additives or glidants [88, 89]. The adsorption of the nanometre-sized particles on the primary particle, which is the material to be coated, acts as a roughening of the surface. Irregularly shaped fine particles are more flowable than spherical particles, as the interparticle forces depend on the local radius of curvature at contact [88]. This results in enhanced flow properties by already using small quantities of the flow control additive [89, 90].

In this work, we use the flow control additive Aerosil® R812, which is nanometre-sized silica manufactured by Evonik [91]. The Aerosil particles have an average diameter of 7 nm and a density of $2.2\,\mathrm{g\,cm^{-3}}$ [91]. Studies on the effectiveness of nanoscale flow control additives have shown that the nanoparticles adsorb as agglomerates and not as separate particles on the primary particles' surface [90]. An increased mixing time can lead to the agglomerates' deterioration during the mixing process, as illustrated in figure 2.1. A complete surface coverage will lead to a smooth surface, which results in a deterioration of flowability [90]. Previous studies with Aerosil® R812 have shown that a mixing time of 5 min is most efficient [84, 92].

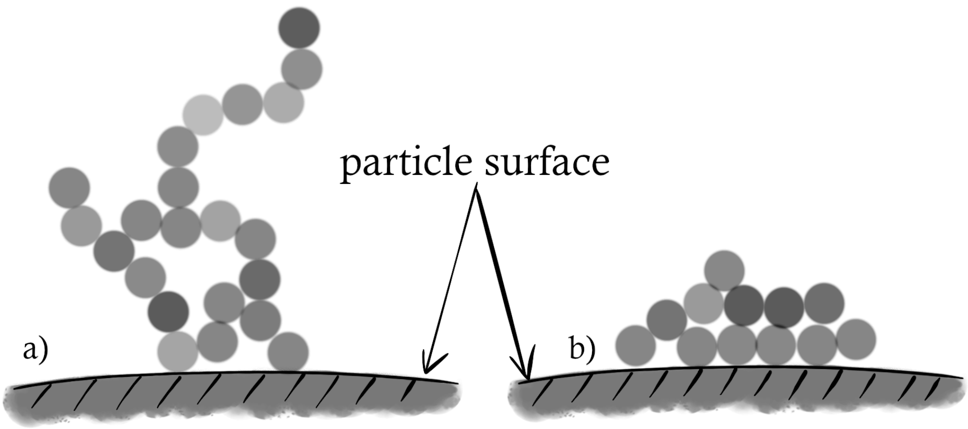

Figure 2.1.: Model for particle surface coverage with nanoparticle flow control additive [93]. a) At the beginning of the mixing process, agglomerates of the nanometre-sized particles settle on the surface. b) In the course of the mixing process, the agglomerates are destroyed, resulting in the deposition of smaller fragments. Reproduced after reference [32].

2.2.3. Experimental Methods

For the calculation of the particle surface coverage with nanoparticles we assume that the primary particles are spherical and monodisperse. The highest density packing of spherical particles on a surface can be approximated by a hexagonal packing arrangement [90].

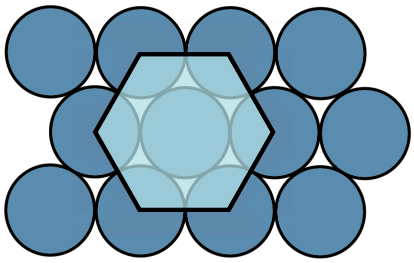

Figure 2.2.: Arrangement of particles on a surface according to the hexagon model.

As shown in figure 2.2, a particle occupies the area of a hexagon. The area of a regular hexagon with side length D is:

$$A_H = 2 \cdot \sqrt{3} \cdot D^2. \tag{2.1}$$

Within each hexagon the area is covered by circles with area $A_C = \pi/4D^2$:

$$A_{HC} = 3A_C = \frac{3\pi}{4}D^2. \tag{2.2}$$

So that the packing density is:

$$PD = A_{HC}/A_H = \frac{\pi\sqrt{3}}{6} \approx 0.9069. \tag{2.3}$$

With this packing efficiency, we can relate the surface area of a spherical particle A_p to the radius of the coating particles:

$$0.9A_p = 3.6\pi r_p^2 \approx N_c \pi r_p^2 \tag{2.4}$$

with the radius of the primary particle r_p and the nanoparticle r_c respectively and the number of nanoparticles N_c, which yields the following relation:

$$N_c = 3.6\left(\frac{r_p}{r_c}\right)^2. \tag{2.5}$$

The masses of the respective particles are calculated with the given density ρ, radius r and number of particles N:

$$m_p = \frac{4}{3}\pi\rho_p r_p^3 N_p, \tag{2.6}$$

$$m_c = N_p\frac{4}{3}\pi\rho_c r_c^3 N_c. \tag{2.7}$$

The ratio of the mass of coating particles to primary particles is obtained by performing some manipulation on equations (2.5) to (2.7):

$$\frac{m_c}{m_p} = 3.6\frac{r_c\rho_c}{r_p\rho_p}. \tag{2.8}$$

Material Preparation Protocol

We have a detailed particle size analysis for the HGMs Q-CEL® 5020FPS provided by the distributor and determined the density with a helium pycnometer, AccuPyc 1340 II of company Micromeritics. With the given density and particle diameter, together with the specifications for Aerosil from the datasheet, we determine the mixing ratio. To coat the HGMs with the flow control additive, we placed the desired amount in a bulk container and mixed the components in a VWR VV3 orbital vortex mixer for 5 min. Next, we placed the coated material into a glass dish and heated it in a Heraeus VTR 5022 vacuum oven at 200 °C for at least half an hour, as this has a positive effect on flowability, according to previous studies [84]. During the drying process, larger agglomerations of particles form that we removed by sieving through a 200 µm mesh.

Furthermore, we analyzed the HGMs with a light and a scanning electron microscope (SEM). With the light microscope Zeiss AxioImager A.2m, we took magnified images of the HGMs. In addition, we used dark-field microscopy, which gives a high degree of contrast. It is a technique in which the light passing through the sample is reflected, diffracted, or refracted from oblique angles into the microscope objective. This results in a bright image of the specimen on a dark background. To resolve the surface of the HGMs, we use an SEM (Zeiss GeminiSEM 500). This method allows us to analyze the surface coating with a higher magnification. An SEM produces images by scanning over a sample surface with a high-energy beam of electrons. The interaction of the electrons with the sample produces secondary electrons, backscattered electrons, and X-rays, whose signals are collected by detectors and processed into images.

2.2.4. Results

The particle size analysis provided by the distributor gives us a mean diameter of $d = 43\,\mu\text{m}$ and particle percentiles of $d_{10} = 14\,\mu\text{m}$ and $d_{90} = 72\,\mu\text{m}$. The density measurement with a helium pycnometer gives us a density ρ_p of $238\,\text{kg}\,\text{m}^{-3}$. We attached the particle size distribution analysis and the pycnometer results in the appendix.

Figure 2.3 shows dark-field microscopy images of the uncoated Q-CEL® 5020FPS. The image rows represent different magnification levels, as seen from the scale at the bottom left. In the left column, we show the images of an HGM sample that is more than ten years old and has been exposed to ambient air for longer periods; the sample on the right side was delivered by the manufacturer a few weeks before we took the image. In figure 2.3a and 2.3c we see that the material exhibits several larger agglomerations. At the same magnification level as in the left column, figure 2.3b and 2.3d shows the new material. Compared to the old material, there are no agglomerates. Furthermore, we notice the materials' polydispersity and that a few particles deviate from the round shape and appear more oval.

With a diameter of $43\,\mu\text{m}$ and density of $238\,\text{kg}\,\text{m}^{-3}$ given above, we determined the flow control additive coating mass of 0.005 following the calculations in subsection 2.2.3 and prepared the material as described in 2.2.3.

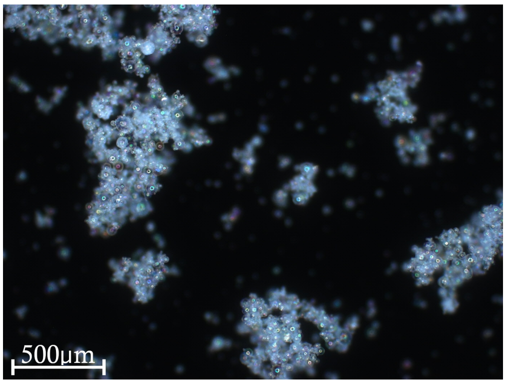

(a) 500 µm resolution; old material.

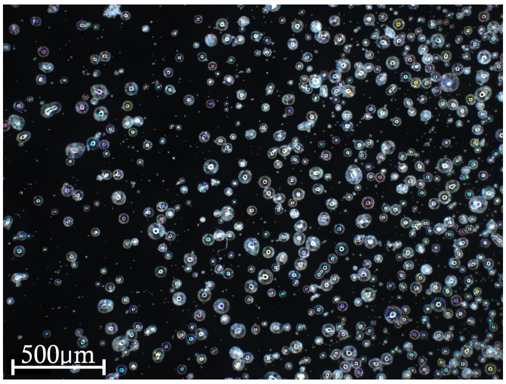

(b) 500 µm resolution; new material.

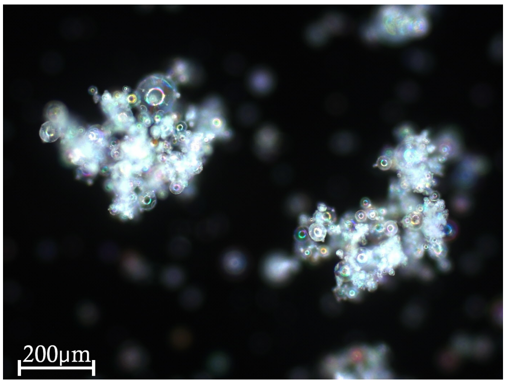

(c) 200 µm resolution; old material.

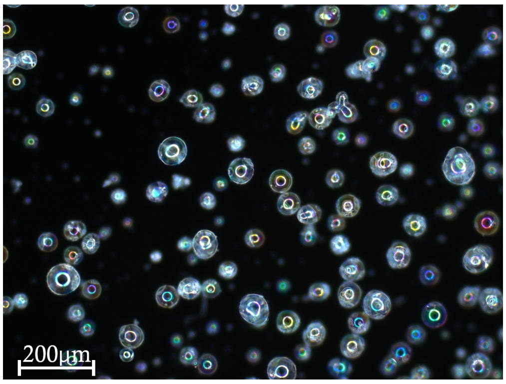

(d) 200 µm resolution; new material.

Figure 2.3.: Dark-field microscopy images of two different (uncoated) HGMs of Q-CEL® 5020FPS. Left column: >10 years old uncoated material with several agglomerations. Right column: new material; the picture was taken a few weeks after delivery by the distributor and shows no agglomerations.

Figure 2.4 shows scanning electron microscopy (SEM) images of the uncoated (left column) and coated (right column) Q-CEL® 5020FPS at two different magnification levels in comparison. Figure 2.4a and 2.4b show the uncoated and coated HGMs at a magnification level of 300. In both images we detect large, irregular shaped agglomerations of particles. several HGMs below the size of 25 µm accumulate around one 70 µm and several 35 µm sized particles. This phenomenon appears, slightly less pronounced, on several spheres. Most particles up to 40 µm host at least one small sojourner particle. Particularly noteworthy is a prominent 85 µm particle in the upper left corner of figure 2.4b, where the cavity is filled with particles under 15 µm diameter.

Figure 2.4c shows the surface of a HGM at a magnification of 3000x. In the upper left half of the sphere, we see an elongated object on the surface. In addition, there are few areas on the surface where small particles of unknown origin also seem to adhere to the surface. Figure 2.4d shows the coated surface of an HGM at the same magnification level. We see small agglomerates spread evenly over the surface and have a size of about 300 to 400 nm. At the edge of the image, we see a small particle with a diameter of 4.5 µm next to the larger sphere.

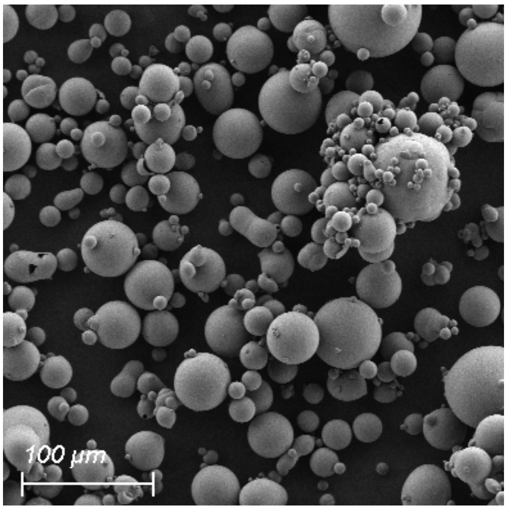

(a) Uncoated HGMs: magnification 300x.

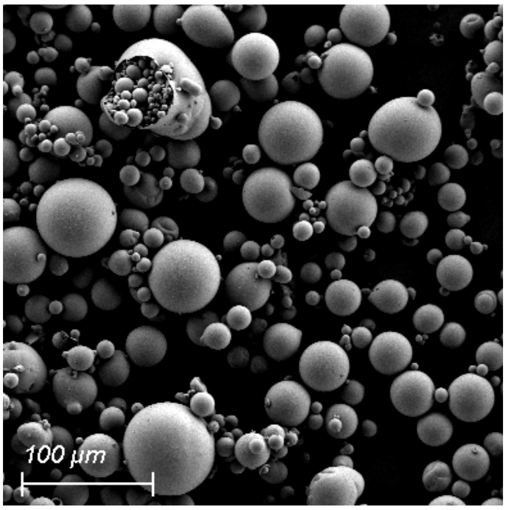

(b) Coated HGM: magnification 300x.

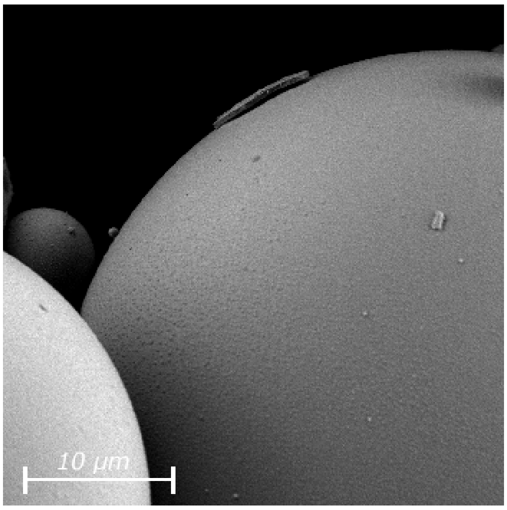

(c) Uncoated HGM: magnification 3000x.

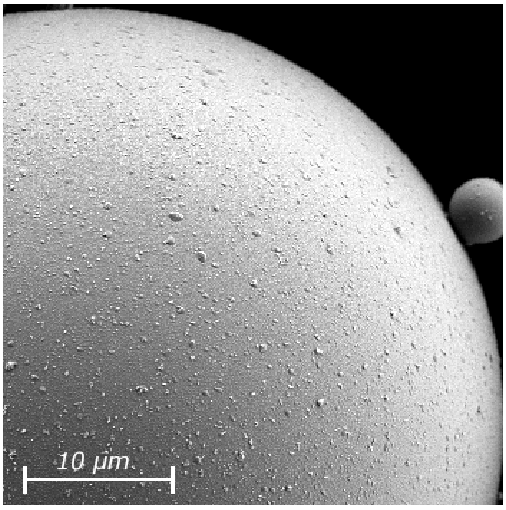

(d) Coated HGM: magnification 3000x.

Figure 2.4.: Scanning electron microscopy (SEM) images of the uncoated (left column) and the coated HGMs (right column) Q-CEL® 5020FPS at two different magnification levels. a) Uncoated sample: the particles are spherical and polydisperse; small HGMs agglomerate around a 70 µm particle. b) Coated sample: smaller particles adhere to larger HGMs. The cavity of a damaged HGM is filled with several particles under 15 µm diameter. c) Uncoated HGM: the surface is smooth; small particles of unknown origin adhere to the larger surface. d) Coated HGM: small aggregations are evenly distributed on the particle's surface.

In figure 2.5, we show two pictures of pouring Q-CEL® 5020FPS from a measuring spoon down into a glass dish: uncoated on the left and coated material on the right. The uncoated material has a grainy surface and flows in small clumps from the measurement spoon, while the coated material flows like a liquid and has a smooth surface. The coated material is sensitive to external stress and seems to compress even at the lowest pressure.

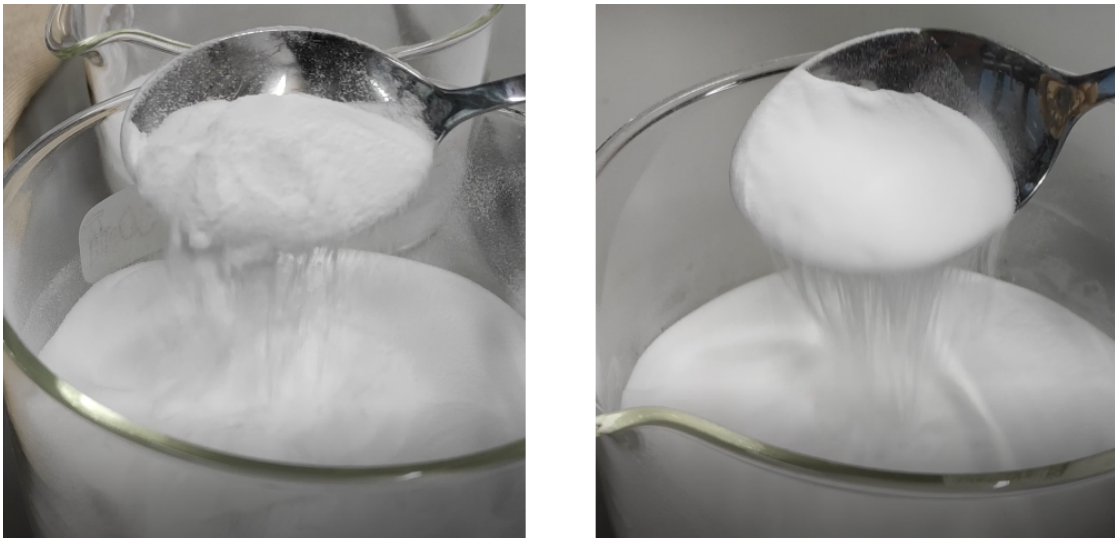

Figure 2.5.: Pouring Q-CEL® 5020FPS from a tea spoon down into a glass dish: the uncoated material (left) has a grainy surface structure and flows in clumps, and the coated material (right) flows liquid-like, exhibiting a comparably smooth surface.

In figure 2.6, we show images of the coated material in a glass dish after the sieving process; the inset gives a close-up of a fingertip over the material's surface. At the macroscopic level, we observe that the particles form a spiky surface pattern, which appears to be oriented in a joint direction. In the left image, we observe this phenomenon, especially at the glass wall and in the vicinity on the left of a centimeter-sized area. In the right image, the orientation of the particles extends over several centimeters. In the inset, we show the response of the coated material to a fingertip (without contact). We observe that the particles align themselves towards the fingertip, at an approach of a few millimeters above the surface. In addition, the particles appear to pile upward. We can see this phenomenon in the height at which the particles stretch a few millimeters above the surface.

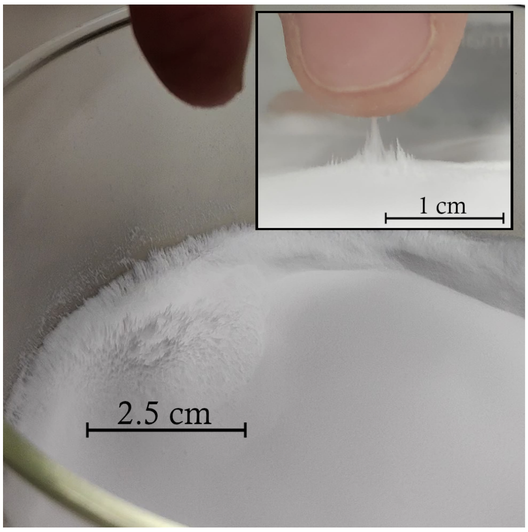

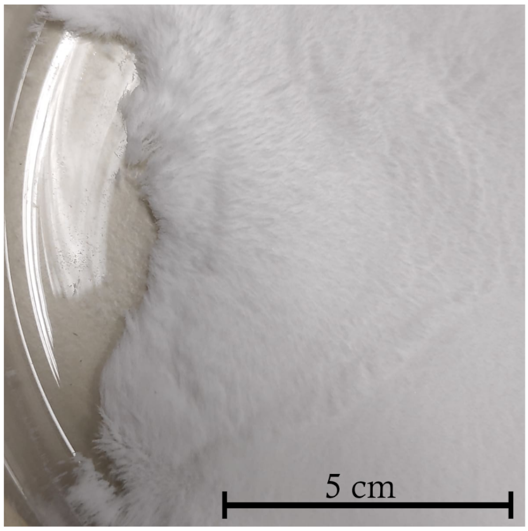

Figure 2.6.: Macroscopic alignment of the coated material: after the sieving process, we observe spiky surface patterns, which seem to align to a specific direction. We show a fingertip a few millimeters above the materials' surface in the inset. The particles stretch up towards the fingertip.

Figure 2.7 shows two light microscopy images of the same coated material on a plastic Petri dish. The scale is given at the bottom right and also applies to the inset. In both images, we see that the particles line up in chains of two to four or long particle chains, as seen in the main image.

Characteristic Parameters of the Particle System

Next, we calculate the characteristic parameters of bedform formation for the Q-CEL® 5020FPS, as we already did with estimated parameters in section 1.5.

To estimate the rebound threshold, we need the particle-fluid density ratio and the Galileo number:

$$s = \frac{\rho_p}{\rho_f} = \frac{238}{1.2} \mathrm{kg\,m^{-3}} \approx 200 \tag{2.9}$$

$$Ga \equiv \frac{\sqrt{(s-1)gd^3}}{\nu} = \frac{\sqrt{199 \cdot 9.81\,\mathrm{m\,s^{-2}} \cdot (43\,\mathrm{\mu m})^3}}{14.5\,\mathrm{\mu m^2\,s^{-1}}} = 0.86. \tag{2.10}$$

For the estimation of the rebound threshold, from which we obtain the threshold Shields number, the square-root of the particle-fluid density ratio and the Galileo number is needed:

$$\sqrt{s}Ga = 12 < 50. \tag{2.11}$$

This means for the chosen particle system the rebound threshold Θ_r^t lies between $0.1 < \Theta_r^t < 0.2$ and since $\Theta_t > 2\Theta_r^t$ for viscous bedload [53], the threshold Shields number lies between $0.2 < \Theta_t < 0.4$. From this, the required shear velocity can be derived:

$$u_* = \sqrt{\Theta_t \cdot [(s-1)gd]} \approx 0.13 \text{ to } 0.18\,\mathrm{m\,s^{-1}}. \tag{2.12}$$

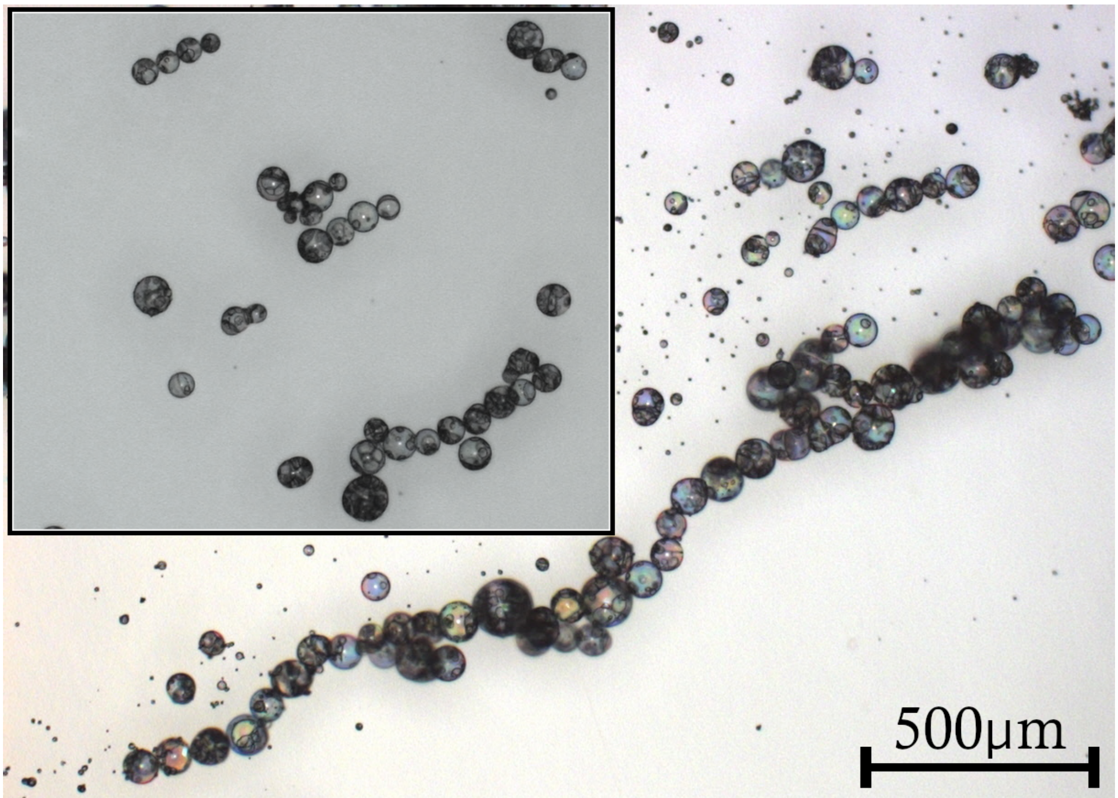

Figure 2.7.: Microscopy images of coated Q-CEL® 5020FPS from two different areas (main image and inset). The scale is valid for both images. Particles line up and form chains on different spots on the plastic petri dish.

Then, the grain-based Reynolds number Re_d is in the order of:

$$\mathrm{Re}_d = \frac{u_* d}{\nu} \approx 0.5. \tag{2.13}$$

Combining the results gives an estimate for the viscous bedload saturation length:

$$l_{sat} = \frac{a_b Re_d d}{Ga^{1.2}} = \frac{140 \cdot 0.5}{0.86^{1.2}} \cdot 43\,\mu\mathrm{m} \approx 4\,\mathrm{mm} \tag{2.14}$$

with proportionality factor $a_b = 140$ (further details in the supplementary material of reference [10]). We know that mature subaqueous ripples and aeolian dunes have a height-to-length ratio of 1/15 [12, 82, 83]. This gives a bedform size of a few centimeters and a height in the order of millimeters.

2.2.5. Discussion

We analyzed uncoated and coated Q-CEL® 5020FPS HGMs with a light microscope, SEM, and camera images. We showed that agglomerations appear after a long storage of the uncoated HGMs, which we could not observe in the newly delivered material. We deduced from surface images that the HGMs were coated, and we also showed an improvement in flow behavior when poured into a glass dish. We showed that the material aligns macroscopically in a specific direction and responds with alignment when approached with a fingertip. Using particle size analysis and density measurement, we determined the coating ratio and calculated characteristic parameters that govern bedform formation. We proved that the selected particle system matches the conditions we set in section 1.5.

Despite matching the ideal parameters such as particle size and diameter, we see the challenges of working with this material. The chosen HGMs seem to be highly hygroscopic and will tend to agglomerate over time when exposed to ambient air, a behavior which the distributor also noted in the datasheet [94]. We also notice this on a macroscopic level: the old HGM sample seems flaky, and the flow behavior also resembles moist flour. This implies that we may need higher wind speeds for bedform formation to entrain the particles due to the higher attractive interparticle forces. We can counteract agglomeration by carefully handling the HGMs: the material should be stored in tightly closed containers, with the quantities needed for experimentation stored in a smaller container to avoid contaminating the remaining portion with ambient moisture. In addition, we suggest that the (un)coated material goes through a drying process before each experiment begins.

Furthermore, the particle size analysis and the SEM images show that the HGMs are polydisperse, and there also appear to be clusters of smaller particles on larger ones. Regarding the agglomerations, it seems to make no difference whether the HGMs are coated or uncoated. Due to the polydispersity, we expect to observe deviations from the ideal calculations of the length scales for bedform formation since the characteristic parameters and equations commonly include the particle diameter. For example, our estimates give a saturation length of about 4 mm for a particle diameter of 43 µm. This value varies for larger or smaller particle diameters; however, it remains in the millimeter range.

The close-up images of the HGM surface showed in the coated case that the surface was covered with the flow control additive as expected. In contrast to our calculation of a monolayer coverage of Aerosil, it is clear from the 2.4d image that the flow control agent adsorbs in agglomerates and at relatively uniform spacings on the surface of the HGMs.

Another phenomenon we observed, especially after the sieving process, was the alignment of the material in a common direction. We even noticed thin particle columns of millimeters in size stretching out in the fingertip direction if approached with the fingertip. This effect appears to be triboelectric charging. The light microscopy image shows several particles lined up, presumably orienting themselves along charged lines on the plastic Petrie dish. These observations indicate that the HGMs charge quickly.

We cannot assess the impact this has on our experiment. In a recent study, there was evidence that tribocharged grains affect particle lift during saltation, which has implications for the initiation of saltation on Mars [95]. However, it is unlikely that the particles will saltate in our case, and we have no information about the charge distribution in our material. An enhanced attractive interparticle force due to tribocharging will have consequences for the fluid threshold, and we will need higher wind speeds to lift the particles. In practical terms, this means for our requirements that we have to take a countermeasure here as well. The absence of triboelectric charge promotes the reproducibility of our material preparation since the lack of information about the extent of the charge makes it difficult to assess the consequences. We suggest keeping the coated material in a sealed container to discharge after sieving.

2.2.6. Conclusions

We have demonstrated that working with the chosen HGMs entails challenges such as clumping during extended storage times. The coating with the flow control additive Aerosil® R812 proved successful; the material appears more flowable after coating than before. However, we observe that the material becomes triboelectrically charged, which has a yet unknown effect on the transport threshold. In addition, the HGMs are polydisperse, which leads to variations in the prediction of the saturation length. However, the calculations of the characteristic parameters with the given particle diameter and the measured density predict a saturation length in the order of a few millimeters and consequently the formation of centimeter-sized bedforms.

The reproducibility of the experiments depends highly on the preparation of the material. We note three phenomena that enhance attractive forces between the particles and thus challenge experimentation: ambient humidity, triboelectric charging, and the sensitivity to external pressure.

In summary, we have characterized a particle system that satisfies our requirements set in section 1.5. Consequently, we expect to observe bedform formation in the aeolian viscous bedload regime with this particle system.

2.3. Laboratory Low-Speed Wind Tunnel

The design and construction of a wind tunnel depends on the purpose it is intended to fulfill. For the study of aeolian processes in the laboratory there are several wind tunnels worldwide with a test area dimension typically one meter wide and high and 5 to 25 m long [96]. For an extensive review of selected saltation studies in the wind tunnel, we refer the reader to reference [96].

To observe viscous bedload transport of sediment, we need wind speeds at which the viscous sublayer is larger than the diameter of the selected particles, which we introduced in section 2.2. As the structures are estimated to be a few centimeters in size (see section 1.5), the test area should have a length of at least 45 cm downwind, so that the structures can migrate a sufficient distance. In addition, the prepared material should be placed on an area with uniform wind speed far away from the wind tunnel walls and the edges of the test plate to avoid boundary effects.

We will introduce a wind tunnel setup that fulfills these requirements in the following. After a detailed description of the wind tunnel, two different methods will be briefly outlined, used to characterize the wind tunnel. Then, we will present the wind speed measurements obtained from both methods in the results, from which we calculate dimensionless numbers. After discussing the results, the chapter will end with a conclusion.

2.3.1. Dimensions and Setup

The frame of the custom-made[1] closed wind tunnel is made of aluminum profiles and has a total size of 120 × 80 × 80 cm, with transparent sidewalls made of acrylic glass. Figure 2.8 shows a schematic view of the entire setup. The setup consists of two sections: the upper part with the experimental test area with a length of 60 cm and a width of 50 cm, where coarse sandpaper (∼ 50 µm) covers the surface, and the lower part equipped with 18 fans (Pabst, type 4112NH4)

[1] The wind tunnel was designed and built by Matthias Sperl and Stefan Frank-Richter. The setup was optimized by Philip Pütsch.

controlled by two microcontrollers connected to a laptop. We can control each fan; a user interface allows monitoring and control of the system. The speed translates into percentage, i.e., 100% fan power is the maximum rotation speed a fan can perform in the given system. With all the fans running at the maximum setting, wind speeds up to $7\,\mathrm{m\,s^{-1}}$ can be reached. The setup is completely closed, i.e.,

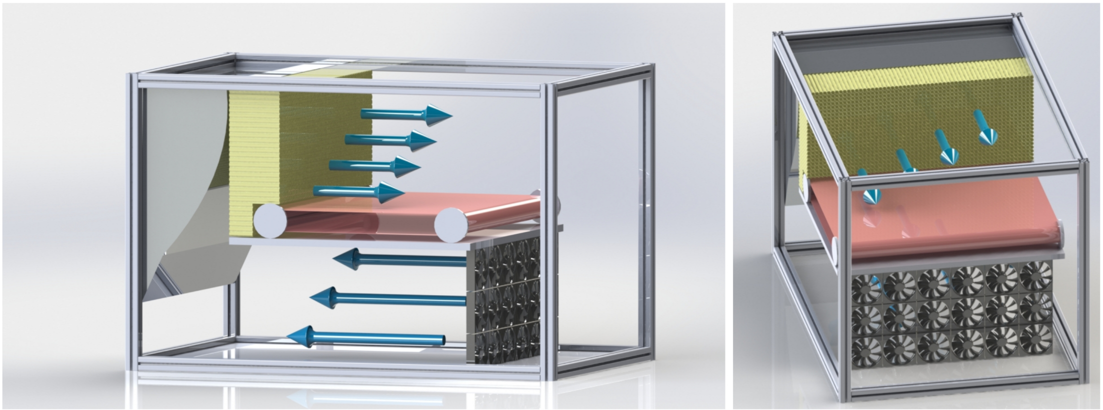

Figure 2.8.: Schematic setup of the closed laboratory wind tunnel. Airflow generated by the fans is guided through the rectifiers (yellow) via deflection plates (grey), where it reaches the experimental surface (red). [2]

the wind flow generated in the lower section is guided to the upper section via a deflector plate and reaches the airflow straightener consisting of an array of straws (diameter 6.2mm, 15cm long, Plascore). The straws ensure that a unidirectional flow enters the experimental area and reduces vortices caused in particular by the hard curvature given the rectangular structure. We placed a single-lens reflex camera (SLR, Nikon D3) outside the wind tunnel, capturing the entire experimental surface. In addition, we installed a 9 cm long line laser to calculate the height profiles of the emerging structures inside the wind tunnel via triangulation and for particle image velocimetry (PIV) measurements. Figure 2.9 shows the wind tunnel including equipment in two images: 2.9a an outside view of the setup showing the high-speed camera on a tripod and b) an inside view of an experiment in operation. The transparency of the setup walls allows observation of the running experiment from all sides. In a): on the opposite side (not shown in the picture), we attached a spotlight to the aluminum profile, which on the one hand, provides adequate

[2]CAD schematic provided by Stefan Frank-Richter.

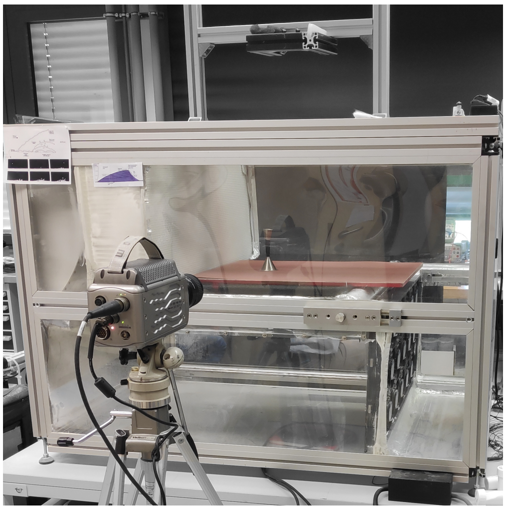

(a) The walls are transparent, the experiments can be observed from all sides. The high-speed camera (grey box on the tripod) can be moved freely.

(b) High-dynamic-range image of the test area. The line laser can be moved as needed. Here a bedform migrates towards the laser line.

Figure 2.9.: Side view of the laboratory wind tunnel: a) from outside and b) inside.

illumination of the structures being formed in the wind tunnel, as well as a high wind tunnel interior temperature. With a temperature between 25 and 30 degrees, the relative humidity inside the wind tunnel is approximately 25 percent depending on the heating time. The moderate heating of the wind tunnel provides a dry environment, which is necessary, as the material used is hydrophobic but still highly sensitive to moisture (see section 2.2). In b), the nine cm long laser line can be seen, with a bedform next to the line. To measure continuous height profiles, we had to move the laser along the migration path of the structure.

2.3.2. Experimental Methods

We measured the wind velocity with a handheld anemometer from Kaindl at different wind speeds. In addition to the momentary speed, the device gives the average wind speed as an output. The accuracy of the anemometer is $\Delta v = 0.1\,\mathrm{m\,s^{-1}}$. We compared the measurements with the wind speeds obtained from the particle image velocimetry (PIV) method. The advantage of this method compared to the anemometer is that it is a non-invasive measurement.

The PIV setup consists of a high-speed camera (Phantom v10 from Vision Research), a laptop to control the camera and analyze the images with the corresponding software (Phantom Camera Control PCC 3.6), tracer particles, and a laser, used to illuminate the particles. Figure 2.10 illustrates the experimental arrangement. We decided to use the material described in section 2.2 as seeding to exclude the

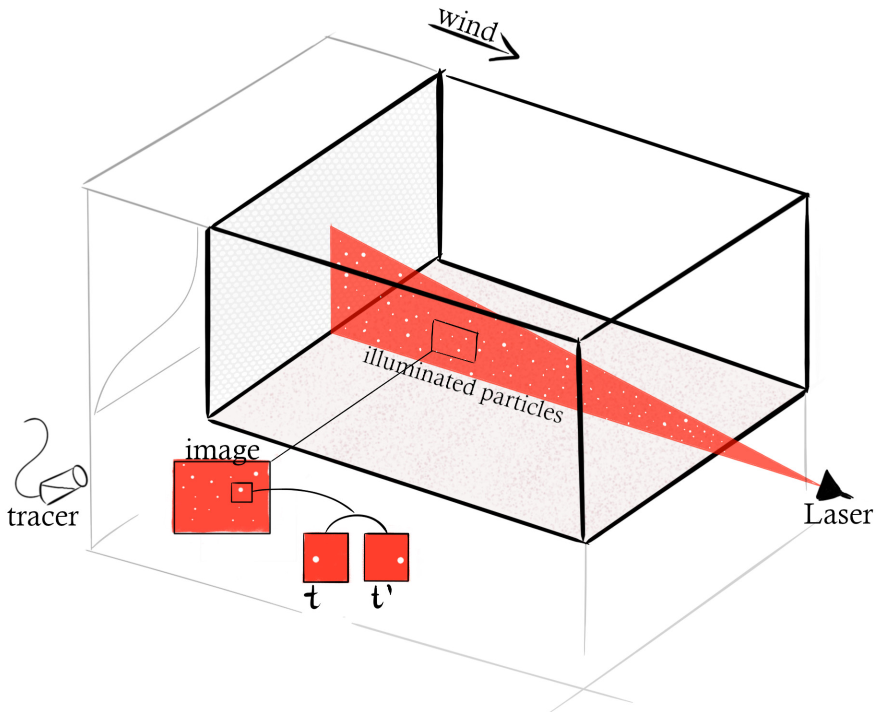

Figure 2.10.: Schematic of the PIV setup. Tracer particles (white dots) are added to the flow through a pressurized air hose at the back of the wind tunnel. The scattered light is recorded with a camera. From an image pair, the mean particle displacement is determined by a cross-correlation algorithm, giving us the the wind velocity [97].

influence of external particles on the experiments. We added the tracer particles into the flow through a pressurized air hose at the back of the wind tunnel and illuminated them with the laser sheet in the plane. We recorded the scattered light with the camera and divided a selected image pair into equally sized interrogation areas. A cross-correlation algorithm then determines the mean particle displacement by matching intensity peaks [97]. Finally, we determine the flow velocity with the time difference and the mean displacement known. We averaged the results for ten sequential image pairs of the PIV measurement to obtain a mean wind velocity profile above a chosen point in the test section. We calculated each velocity measurement as the mean of over 70 independent measurements; the uncertainty was taken as the standard deviations of these measurements. For the evaluation of the wind speed, we assume that the seeding particles follow the flow, show only minimal out-of-plane motion and do not influence or disturb the flow. Furthermore, it is necessary that the density of the seeding particles is uniform across the frames and that there are more than 15 particles in each interrogation window. The time between two consecutive frames is 1/1000 s with the available camera. The resolution has been determined from a calibration image and is 12.300px/m. At a wind speed of $4\,\mathrm{m\,s^{-1}}$, the window size is therefore approximately 200 pixels. This means that the first measurement point is approximately 8 mm above the surface, and the following positions are vertically displaced by 2.4 mm.

2.3.3. Results

We measured the wind speed with an anemometer placed in the middle of the test area during an initial test run of the different fan speeds. The fan setting of 50% corresponds on average to a wind speed of about $U = 3.5\,\mathrm{m\,s^{-1}}$; a value that is above the fluid threshold and thus fulfills the requirements for the transport of the chosen particle system described in section 1.5.

Figure 2.11 shows the results of the wind speed measurements 1 cm above the test surface at a setting of 40%, 50% and 60% in a three-dimensional (3D) plot measured with the anemometer. One rectangle corresponds to one measuring point, i.e., we create a horizontal velocity matrix distributed over the entire test plate. The distance between two measurement points is 5 cm. On the left and right, the walls of the wind tunnel are each about 15 cm away from the test surface.

In the 3D plot in figure 2.11 the rectifiers are on the left-hand side, and the black arrow shows the direction of the flow. The color code indicates the measured wind speed. A gentle parabolic wind gradient forms towards the corners of the test area, while the speed in the middle part remains relatively uniform downwind. This applies to all three settings. We see that at each measured point, an increase of 10% corresponds to an increase in wind speed of $1\,\mathrm{m\,s^{-1}}$.

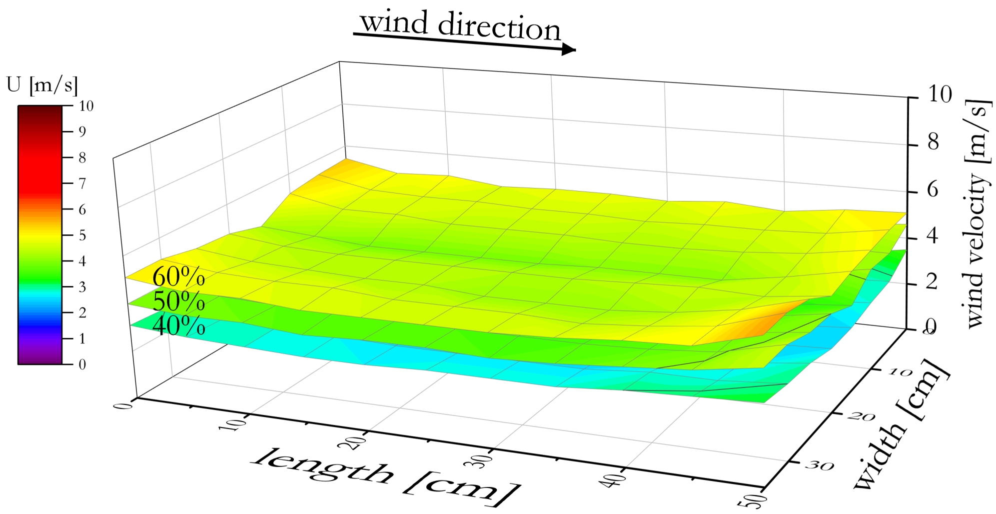

Figure 2.11.: 3D representation of horizontal wind speed above the test area at 40%, 50% and 60% fan power 1 cm above the test surface. The anemometer measurements of the wind speed are colored (see color code). The wind speed increases linearly with increasing fan power, i.e. at each measuring point an increase of 10% equals an increase in wind speed of $1\,\mathrm{m\,s^{-1}}$.

Figure 2.12 shows a wind speed matrix of the 50% fan power data set, this time with a view from the top. Near the left side of the wall, which is 15 cm away from the leftmost measurement point, the wind speed appears to be higher than on the right side but is comparable within the error limits. We find the highest wind speeds at the rectifier's exit (bottom) and end of the test area (top).

From both plots, we observe a wind speed gradient transversely and longitudinally to the wind direction over the entire test area, which in each case has a higher speed towards the outer edges. The wind velocity is uniform in the middle of the test section in a 35 cm long and 10 cm wide strip downwind.

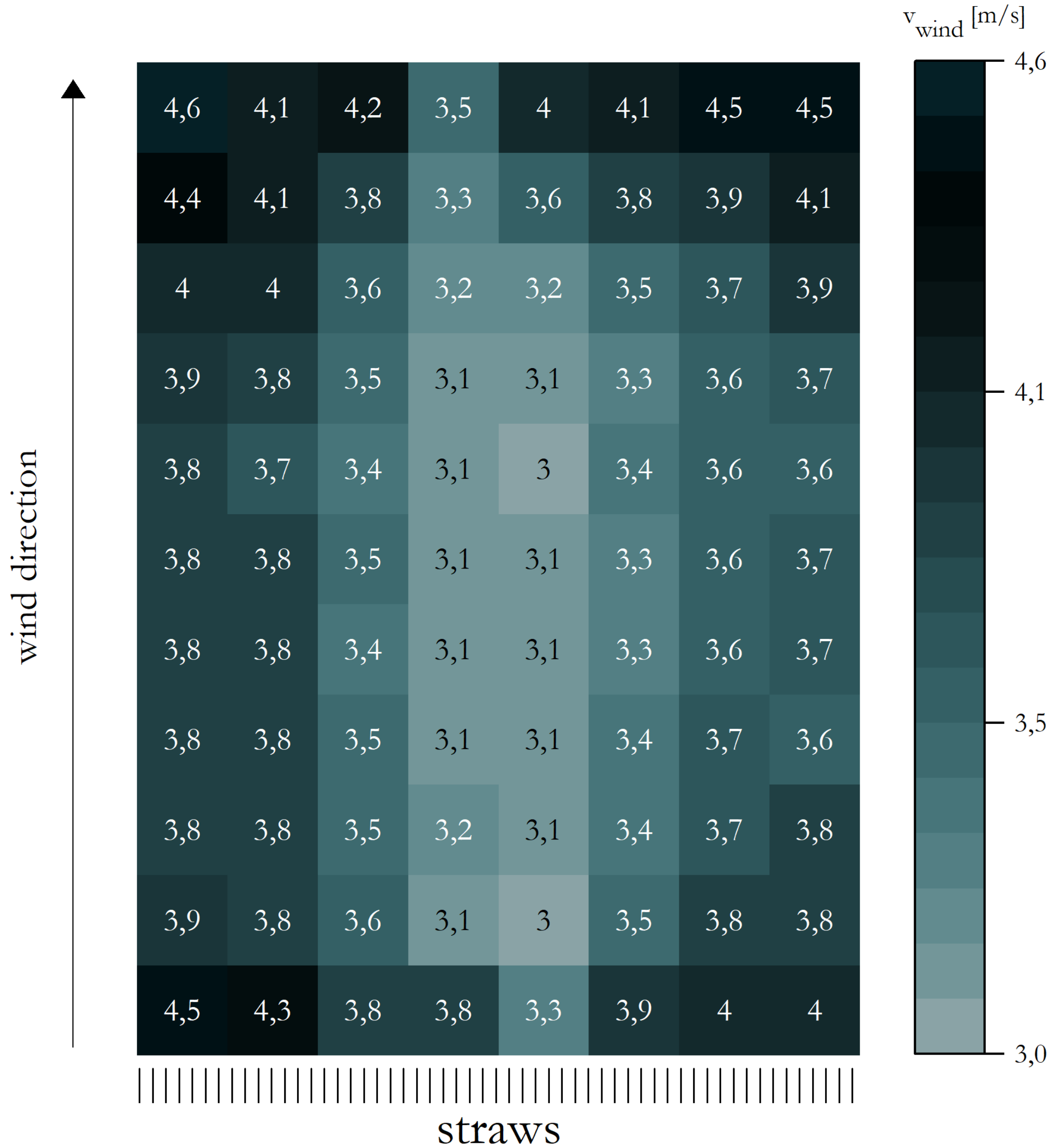

Figure 2.12.: Matrix of wind speed at 50 % fan power. Top view of the test area: at the bottom the flow enters the test section through the honeycomb straws. The black arrow on the left indicates the wind direction; the color code shows the respective wind speed. The wind speed was measured every 5 cm.

Based on these results, the vertical velocity was measured with the anemometer on the central line downwind, at a distance 15 cm from the rectifiers, as shown in the inset of figure 2.13. In addition to this measurement, we used the vertical wind speeds obtained from a PIV study at the same vertical point for comparison (details see section 2.3.2). Figure 2.13 shows the wind velocity plotted against the height above the test surface obtained from both measurement methods. The black rectangular data points represent the anemometer measurements, and the red round data points correspond to the wind speed from the PIV measurement. The top lid of the wind tunnel is about 10 cm above the topmost data point, the maximum height of the initial particle heap has been estimated to be approximately 1 cm and is indicated at the bottom right. The vertical measurement of the wind speeds shows that both measurement methods agree well with the results within the error limits. The velocity increases from the bottom up to a height of about 4 to 5 cm above the test surface. At increasing heights, the wind speed decreases further, with the result that at the highest accessible point, the velocity is $1\,\mathrm{m\,s^{-1}}$ lower than 1 cm above the ground. We performed the PIV measurements up to a height of 5 cm. The resulting error of the PIV data points can be found in the methods section 2.3.2.

From 12 data points of the PIV wind speed velocities, the shear velocity u_* and the roughness length z_0 is obtained using the law-of-wall (eq. 1.5) (see figure 2.14).

$$\ln(z) = \frac{u(z)\kappa}{u_*} + \ln(z_0) \tag{2.15}$$

with the height z, the measured wind velocity $u(z)$, the Kármán's constant κ. The slope of a linear fit to the measured data gives the shear velocity:

$$u_* = 0.207 \pm 0.012\,\mathrm{m\,s^{-1}} \tag{2.16}$$

and the roughness length:

$$z_0 = 35 \pm 14\,\mathrm{\mu m}. \tag{2.17}$$

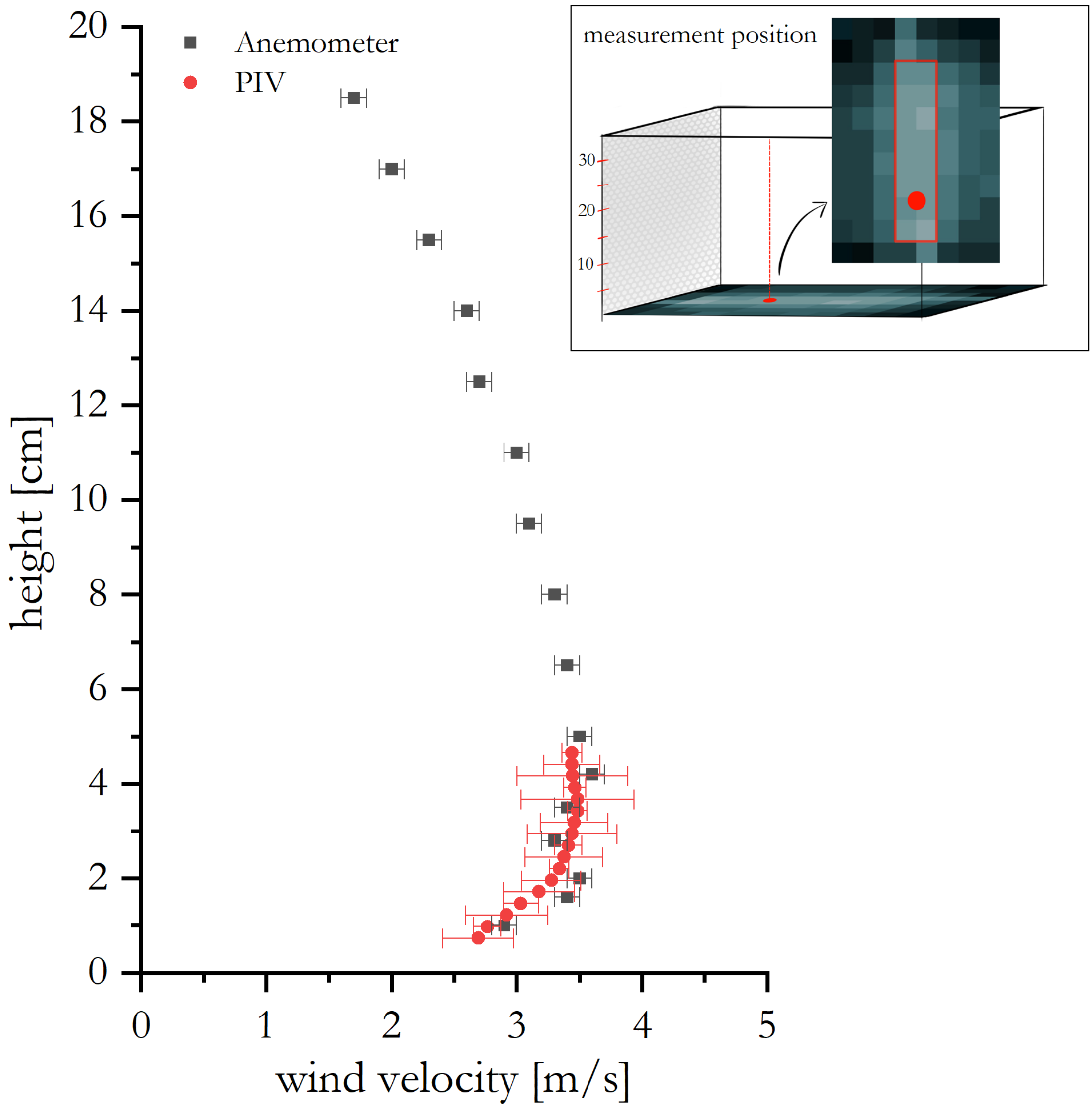

Figure 2.13.: Wind velocity above test area measured with an anemometer and particle image velocimetry (PIV). Inset: measurement position marked on the wind velocity matrix shown in fig. 2.12. The velocity increases up to a height of 4 to 5 cm above the test surface. With increasing height, the velocity decreases towards the top lid of the wind tunnel.

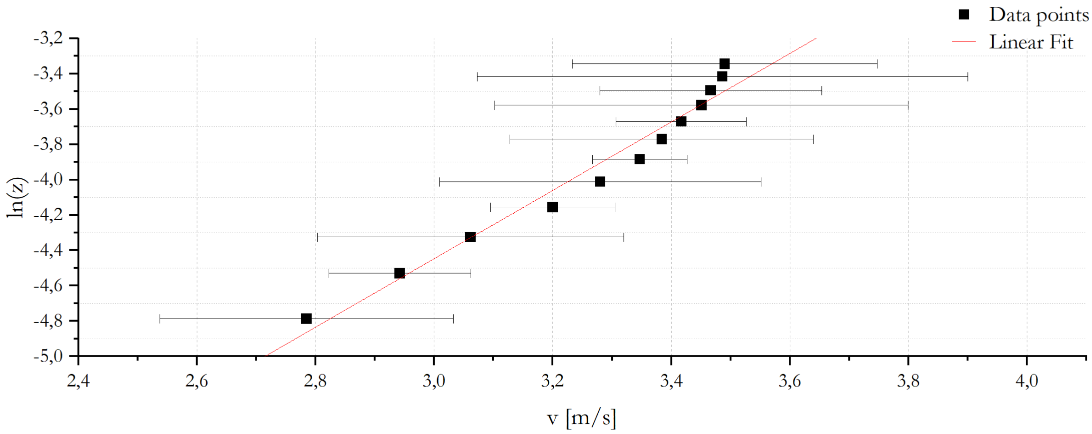

Figure 2.14.: Determination of the shear velocity using the law-of-wall (eq.1.5); logarithmic height vs. the wind speed. From the Particle Image Velocimetry (PIV) method obtained 12 data points, fitted to obtain the shear velocity u_* and the roughness length z_0.

We use these values to calculate dimensionless quantities to characterize the wind tunnel. For the calculation of the Reynolds number, we insert the total height above the test surface of about 30 cm. The mean wind speed is $U = 3\,\mathrm{m\,s^{-1}}$ at 50% fan power, the kinematic viscosity of air is $1.45 \times 10^{-5}\,\mathrm{m^2\,s^{-1}}$. The Reynolds number of the wind tunnel is calculated according to equation (1.2):

$$\mathrm{Re} = \frac{LU}{\nu} \approx 6 \times 10^4. \tag{2.18}$$

With the same parameters, the Froude number is given according to equation (1.4):

$$Fr = \frac{U_\infty^2}{gL} = 0.3. \tag{2.19}$$

The thickness of the viscous sublayer can be estimated by equation (1.7) and gives:

$$\delta_\nu \sim \frac{\nu}{u_*} \approx 70\,\mu\mathrm{m} \tag{2.20}$$

The dimensionless roughness of the surface in the absence of grains in the wind tunnel equals:

$$\mathrm{Re}_d = \frac{u_* d}{\nu} = \frac{0.207 \cdot 43\,\mu\mathrm{m}}{1.45 \cdot 10^{-5}} = 0.6. \tag{2.21}$$

This corresponds to a hydrodynamically smooth regime, as defined in section 1.2. We performed an initial test run with the coated particle system introduced in section

2.2. Figure 2.15 shows a superimposed image of the 50% wind speed matrix (figure 2.11) and three particle heaps with the same volume placed approximately 15 cm downwind from the rectifiers. In a) we see that every heap is in a different velocity zone approximately 10 cm apart. The bright stripe in the middle corresponds to the area with the uniform wind speed described above. In b), the wind direction is

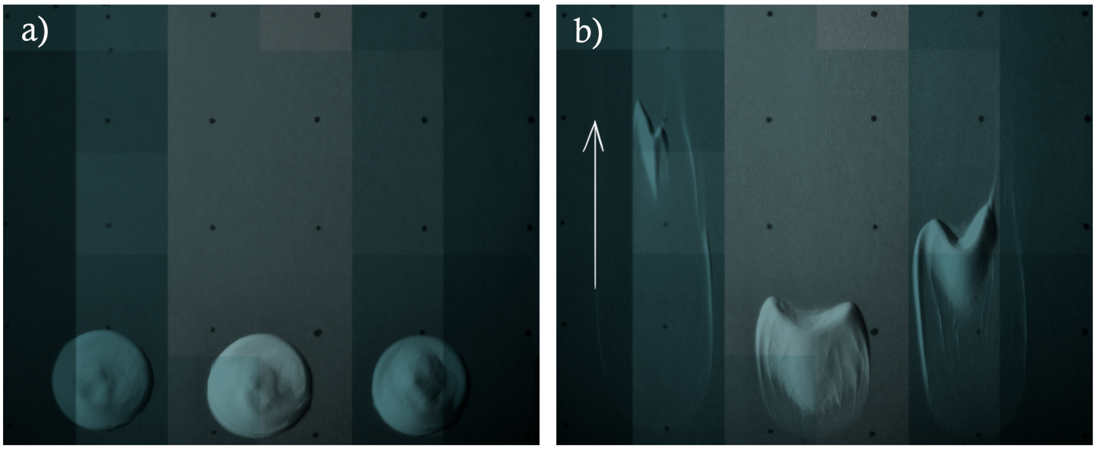

Figure 2.15.: Superimposed images of the wind speed matrix (figure 2.12) and top view of three particle heaps placed at the same starting position. a) Initial heaps are placed at the same distance 15 cm from the rectifiers with approximately the same volume on different velocity zones. b) A few minutes after the start of the experiment, each of the three heaps is in a different position downwind. The white arrow indicates the wind direction; the color code shows the wind speed. The bright color corresponds to lower wind velocities (for detailed map see figure 2.12).

indicated by the white arrow. A few minutes after switching on the airflow, the heaps are in a different downwind position, despite initially equal starting positions. According to the velocity matrix, a higher wind speed acts on the left structure compared to the middle structure.

2.3.4. Discussion and Conclusions

The wind speed measurements show a horizontal wind gradient on the test surface across all three fan speeds. We assume that the main reason for this gradient is that the flow in the wind tunnel encounters several edges due to the rectangular design, which is the primary source of turbulence and can create inhomogeneities in the wind profile. In addition, the test surface is not contained in a separate chamber, is narrower than the total width of the wind tunnel, and was positioned directly in front of the rectifiers. These conditions favor the formation of a wind gradient, as the wind exiting the rectifiers impacts both the walls of the wind tunnel and the edges of the test section. The deflector plate positioned just before the rectifiers has the purpose of minimizing turbulence, but its dimensions and close placement to the rectifiers are likely to be the main reason for the reduced wind velocity of $1\,\mathrm{m\,s^{-1}}$ at the topmost point. In the vertical wind profile in figure 2.13, this is reflected in a lower wind speed in the upper part of the setup. In addition, the flow exiting the straws hits the upper boundary of the wind tunnel, an area that also has several edges, leading to a reduced wind velocity.

The shear velocity and roughness length obtained from the measurements correspond well with expectations (see section 1.5). From equation (1.2) we obtain a Reynolds number in the order of 10^4 for an average wind speed of $3\,\mathrm{m\,s^{-1}}$, resulting in a turbulent boundary layer flow (see section 1.2) with viscous sublayer thickness of approximately $70\,\mathrm{\mu m}$. The low Froude number indicates that we can neglect inertial effects at the free surface with respect to gravity.

A narrow corridor downwind is particularly suitable for experiments because 1) the wind speed is uniform and 2) the central line is furthest away from the walls to minimize boundary wall effects. A test run shows that we can use the test area in the center and that various positions transverse to the wind direction are also suitable for performing experiments. There is no dependence of the aeolian transport and the structure formation on the position. The structures undergo the same morphological development on every spot, which is not directly visible in figure 2.15, but will be discussed in part 4. We did not perform turbulence intensity measurements, but have to keep in mind, that any fluctuation in wind speed will affect the thickness of the viscous sublayer and consequently on the transport mechanism we wish to observe.

In conclusion, we show that the velocities accessible in the wind tunnel are sufficient to transport the particles described in section 2.2. With a viscous sublayer thickness of approximately 70 µm, particle transport in the viscous sublayer should be possible according to our calculations in section 1.5. Fluctuations in wind speed can change the thickness of the sublayer. Despite the wind gradient, we have an area on the test surface with homogeneous wind velocities.

2.4. Conclusions for the Characterization of the Experimental Setup

We characterized a particle system that satisfies the conditions specified in section 1.5. We showed that the selected material is sensitive to ambient humidity and tends to clump during extended exposure to air. Furthermore, we found that the particles charge triboelectrically, which possibly leads to increased attractive forces between the particles. Moreover, the material is polydisperse, leading to potential variations in the saturation length. Despite these limitations, the selected material appears to be suitable to form centimeter-sized bedforms having a saturation length of a few millimeters.

With the characterization of the wind tunnel, we show that our setup can achieve the necessary velocities to transport particles. Despite a wind gradient over the test section, we have identified an area where homogeneous wind speeds prevail. Furthermore, with about 70 µm, the viscous sublayer is close to the particle diameter but still large enough to allow us to observe the viscous bedload transport regime. Possible challenges in experimentation may include potential fluctuations in wind speed that affect the thickness of the viscous sublayer.

In conclusion, we present a particle system and a wind tunnel that allows us to study the aeolian viscous bedload transport regime in the laboratory. To be precise, we expect to observe the formation of bedforms on our test section with the present setup.

In table 2.1, we list characteristic parameters of our experimental setup, along with estimates for bedform formation such as saturation length and dimensions.

In the next chapters we want to tackle the following questions:

1. Does the particle flux of the selected particle system saturate on the length scales available to us, and if so, does it result in the formation of bedforms?
2. What are the morphological characteristics of these structures, and how can we classify and compare them with other sedimentary bedforms?
3. What transport mechanism and hydrodynamic response is responsible for the formation of the bedforms that may develop?

Parameters	Notation	Value	Unit
Fundamental parameters			
Gravitational acceleration	g	9.81	$\mathrm{m\,s^{-2}}$
Fluid density	ρ_f	1.2	$\mathrm{kg\,m^{-3}}$
Kinematic viscosity	ν	$1.45 \cdot 10^{-5}$	$\mathrm{m^2\,s^{-1}}$
Measured/Derived parameters			
Particle density	ρ_p	238	$\mathrm{kg\,m^{-3}}$
Particle diameter	d	43	µm
Measured shear velocity	u_*	0.207 ± 0.012	$\mathrm{m\,s^{-1}}$
Shear velocity threshold	u_t	0.13-0.18	$\mathrm{m\,s^{-1}}$
Roughness length	z_0	35 ± 14	µm
Viscous sublayer thickness	δ_ν	≈ 70	µm
Dimensionless parameters			
Particle-fluid density ratio	s	~ 200	
Grain-based Reynolds number	Re_d	0.6	
Galileo number	Ga	0.85	
Stokes-like number	$\sqrt{s}$Ga	12	
Threshold Shields number	Θ_t	0.2-0.4	
Wind tunnel Reynolds number	Re	$6 \cdot 10^4$	
Wind tunnel Froude number	Fr	0.3	
Predicted parameter			
Saturation length	l_{sat}	≈ 4	
Wavelength	λ	$\approx 4 - 5$	cm
Height	h	$\approx 2 - 3$	mm

Table 2.1.: Overview of the characteristic parameters of the experimental setup: fundamental parameters relevant for calculating the dimensionless and predicted parameters and measured/derived values from section 2.2 and 2.3.

3 Longitudinal and Transverse Instability of a Flat Particle Bed

A chain of centimeter-sized barchan-ripples evolved in the wind tunnel

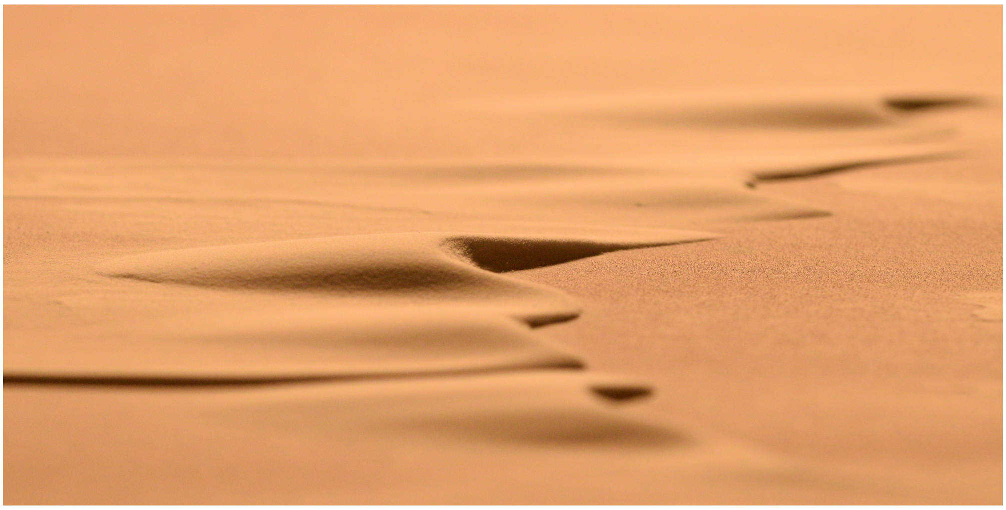

'If this is true [that the movement of sand is a surface effect] it is clearly possible to reproduce in the laboratory the complete phenomena of sand-driving, together with all small-scale surface effects, such as ripples and the like, associated with it.'

R.A.Bagnold (1941)

Bedforms such as dunes and ripples grow on sediment beds exposed to fluid-flow-induced shear forces of suitable magnitude. Here we show that a flat particle bed under unidirectional wind forms transverse bars and decays into individual, centimeter-sized barchan-ripples. We measure the particle flux over a flat bed calculated from the bed's height changes, which exhibits a non-trivial saturation behavior. We derive a local saturation length of a few millimeters, in agreement with the bedform sizes evolving from the flat bed. The morphological comparison with numerical simulations and subaqueous experiments confirms that our experimental results show the same longitudinal and transverse instability. Our results introduce a new approach for small-scale experiments under aeolian conditions in a transport regime previously unexplored in the laboratory.

3.1. Introduction

The formation of dunes from onset to mature bedform includes characteristic time and length scales originating from the interaction between hydrodynamics, topography and sediment transport [2, 70]. The bedform evolution is driven by a longitudinal instability caused by the topography, impacting the interaction between the flow and sediment transport [12]. The origin of this instability lies in two contributions: the upwind shift of the shear stress located before the crest [25, 26, 29] and a characteristic length that the particle flux needs to adapt to the spatial change in shear stress, known as saturation length l_{sat} [29, 42, 46, 47, 50]. This spatial lag leads to the growth and formation of ripples and dunes underwater and in air.

Two types of bedforms can form under unidirectional fluid exposure depending on the availability of sand: Barchans form under low sand availability, and transverse dunes evolve when high amounts of sand are on the ground [1, 2, 98]. We know that transverse dunes destabilize and decay into barchan chains, a finding that has been shown by the results of numerical simulations and has been validated by linear stability analysis and water-tank experiments [99–101]. This transverse instability, which arises due to crosswind sediment transport, implicates that transverse bedforms are not stable on bedrock [100] and explains why barchans are the dominant bedform in areas of low sand availability [99].

Today we know that subaqueous ripples and aeolian dunes are governed by the same instability, the longitudinal and the transverse, although the transport mechanisms are different, and we can predict the formation of bedforms across planets with the help of numerical models [10]. This understanding is currently being put to the test as structures have been discovered on Mars whose physical origin is still being debated [8, 10, 11, 102]. Are these mid-sized Martian structures similar to subaqueous ripples or aeolian impact ripples? The formation of impact ripples and subaqueous ripples are caused by different physical mechanisms, so the topic recently provoked discussions about their origins.

Laboratory experiments contribute significantly to the understanding of these complex phenomena and are indispensable to calibrate numerical models. Previous laboratory studies have focused on subaqueous experiments, where viscous bedload transport has been studied extensively [44, 66, 67, 72, 74, 77–79], while saltation processes, related to the turbulent transport regime, have been investigated in wind tunnels [1, 35, 39, 47, 96, 103–109]. So far, the regime of aeolian viscous bedload transport has not been investigated in the laboratory [8]. However, access to the viscous bedload transport regime under aeolian conditions in laboratories requires choosing a well-tailored particle system, as the particles need to be transported within the viscous sublayer without going into suspension. In section 2.2 we introduced a particle system, coated hollow glass microspheres, characterized by a low density of $238\,\mathrm{kg\,m^{-3}}$ and diameters of $43\,\mathrm{\mu m}$, which is expected to be transported within the viscous sublayer, according to our calculations (see section 2.2.4). Thus, the questions we address in this chapter are: does the particle flux saturate on the length scale available to us, and if so, does it result in the formation of bedforms?

Here we will show that a flat particle bed under unidirectional wind forms transverse bars and decays into smaller individual, centimeter-sized barchan-ripples. For this, we will follow the onset and evolution of the flat bed by analyzing time-lapsed images and measure the emerging length scales of the bedforms along with the transverse bars' destabilization length L_∞, a characteristic length at which transverse dunes decay into barchan chains. We measure the particle flux over a flat bed derived from the beds' height changes. The flux shows a non-trivial saturation behavior and follows an oscillating curve with local saturation plateaus. From this, we derive a local saturation length of a few millimeters, which agrees with the bedform sizes evolving from the flat bed, and presume from the measurements, that two transport mechanisms seem to be at work in our experiment. The morphological comparison with numerical simulations and subaqueous experiments confirms that our results show the same longitudinal and transverse instability.

3.2. Experimental Methods

Setup

We will briefly list the necessary steps for material preparation and refer to section 2.2.3 for a more detailed description of the equipment used. We coated the hollow glass microspheres (HGMs) Q-CEL® 5020FPS with the flow control additive Aerosil® R812. The preparation includes the following steps.

1. The HGMs and the glidant are mixed for 5 min (for ratio calculation see section 2.2.3).
2. After drying the coated material in the vacuum oven at 200 °C for 30 min, we remove larger agglomerates by sieving.
3. The sieving process induces triboelectric charges. We leave the coated material in a sample container for at least three days to discharge.
4. Before the start of the experiment, we heat the coated material again for at least 30 min in the vacuum oven at 200 °C.

For the flat particle bed, we used a 25x10cm template, which we filled to a height of 1 cm with coated material. Because of the material's high sensitivity to external stresses, we omitted to smoothen the bed, which results in the appearance of small impact craters and surface spots left by the impacting particles during the placement on the bed. Consequently, the particle bed is not entirely flat and smooth at the onset.

Height Measurements

The entire test section is imaged with a Nikon D3 camera from the top in a 10 sec interval. A spotlight illuminates the test area from the side. Alternately we can switch the line laser on to record an image of the structure for the height profile measurement. With an image analysis program (GIMP) [110], we analyze the lengths and widths of all bedforms. We obtained the height profiles of the flat particle bed from simple intensity peak picking of the images and triangulation. The line laser's angle of incidence α with respect to the test section and the distance to the baseline x gives us the height at a specific point:

$$h = \tan(\alpha) \cdot x \tag{3.1}$$

from which we obtain a height profile along the line in wind direction. The workflow is shown in figure 3.1. We analyze the intensity peak and the height profile for each image (upper panel). Then, by applying a Savitzky-Golay filter [111], the profile is smoothed, which can be checked via the intensity peak, and as a result, the pixel noise is removed. Finally, in the lower panel on the right, we show the result of the baseline determination. We evaluate each measurement individually,

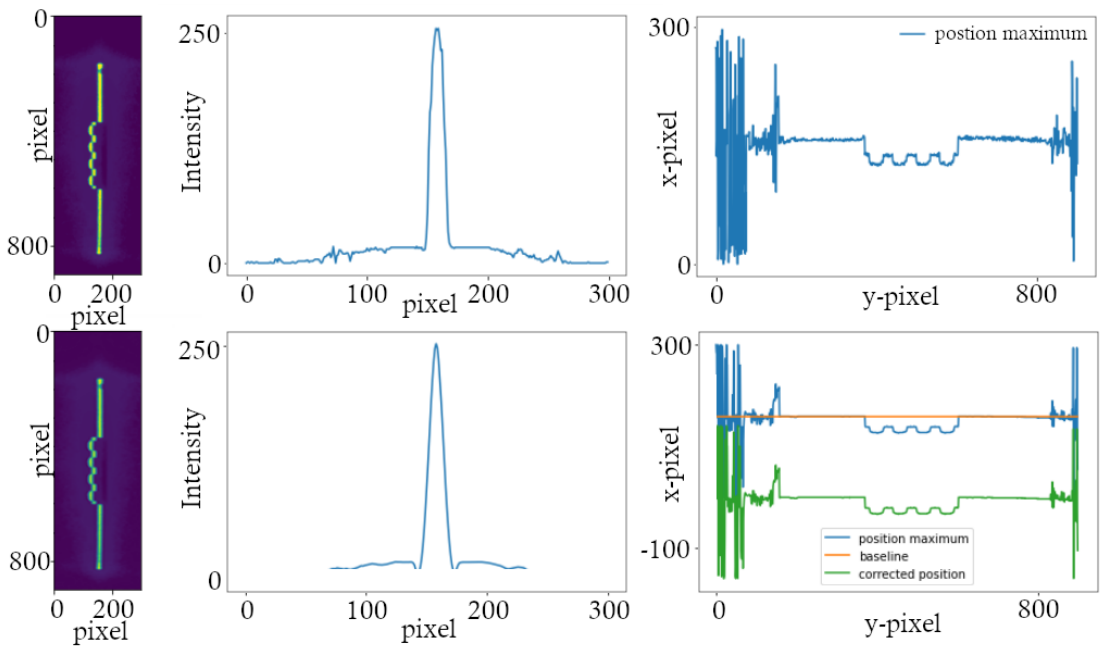

Figure 3.1.: Workflow of height determination. Before smoothing: the upper panel shows the original image, the intensity peak plot, and the resulting profile (only pixel values, no heights). After applying the smoothening function, we get a sharp intensity peak and a noise-free profile. The last plot shows the baseline determination. Finally, we calculate the height via triangulation (see equation (3.1)).

i.e., we visually compare the original with the smoothed profile. In this way, we avoid averaging out possible important features and at the same time ensure that artifacts are minimized. The angular displacement of the laser can result in a height error. The inaccuracy is $\Delta h = 0.2\,\mathrm{mm}$ for a deviation of one degree.

We calibrated the laser line method with a small brick, as its dimensions are well known [112]. Figure 3.2 shows the result of this measurement. In the inset on the top left, there is a CAD drawing of the brick marked with a red line to show the position of the laser line. The CAD images on the right show the dimensions of the brick [112]. The total length differs by 0.2 mm, as does the length of the bricks' mounds. The source of the deviation stems from the smoothing filter being applied, which reduces noise but smoothes out sharp edges. However, this should be negligible for the measurements on the bedforms, whose slopes do not show any sharp edges. We set the fan settings to 50%, which corresponds to a prevailing wind speed 1 cm above the surface of $3.1\,\mathrm{m\,s^{-1}}$.

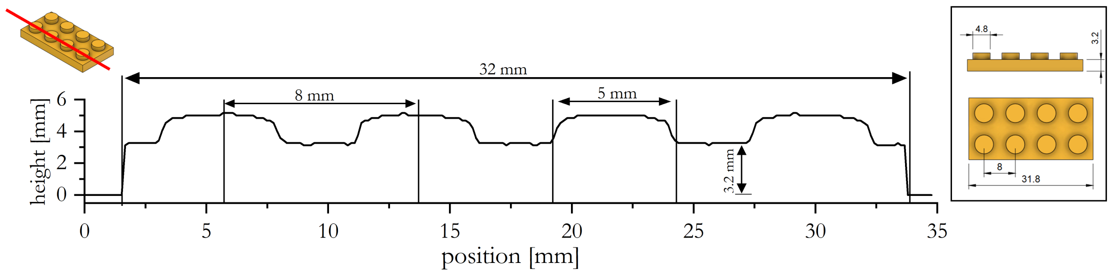

Figure 3.2.: Calibration of the laser line using a small brick. The position of the laser line is indicated on the left yellow brick. The inset on the right shows a CAD image and the dimensions of the brick. The height profile deviates by 0.2 mm from the original size in the measured length. CAD image: reused and modified with permission from Christoph Bartneck [112].

Flux Measurement and Saturation Length

The change of the height profile of the flat particle bed with time is used to derive the saturation length l_{sat} as described by Andreotti et al. [47]. In this case, the particle bed is height matched with a flat metal plate upwind to minimize changes to the wind profile from the height profile of the particle bed. The experimental setup is shown in figure 3.3. Using mass conservation, the particle flux q(x) at a distance x from the onset of the particle bed can be approximated from the height changes Δh with time Δt upwind from x:

$$q(x) = -\int_0^x \frac{\Delta h(\xi)}{\Delta t} d\xi. \tag{3.2}$$

The flux profile can be fitted with:

$$q(x) = q_{sat}\left[1 - e^{-(x-x_0)/l_{sat}}\right] \tag{3.3}$$

to obtain the value of the saturated flux q_{sat} and the saturation length l_{sat}, where x_0 is a freely adjustable parameter [47]. The flux evaluation is based on two height profiles, which are a minute apart. We performed the flux measurement multiple times to ensure its not a transient feature.

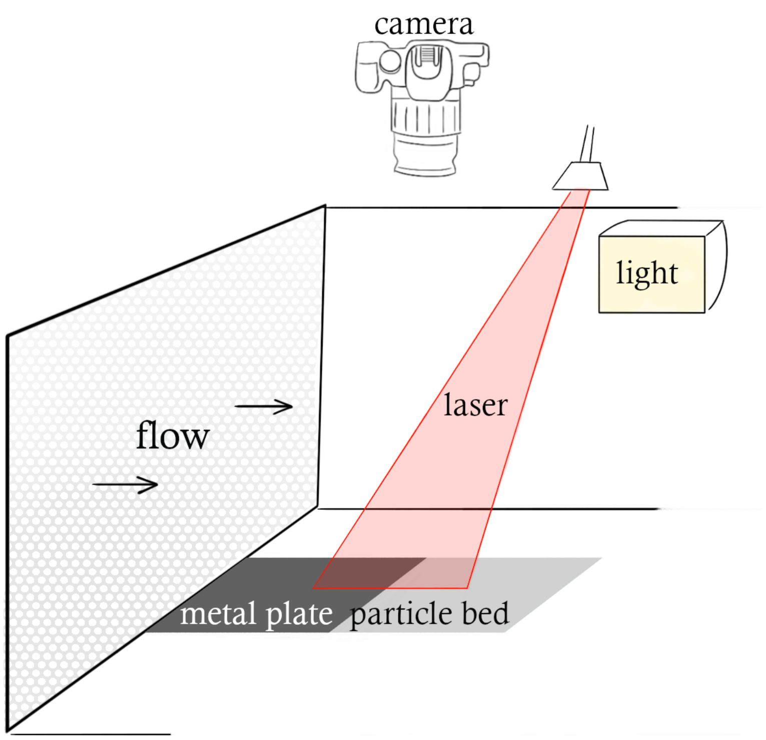

Figure 3.3.: Setup for the flat bed particle flux measurement: Scheme sketching the measurement principle. A flat particle bed with 1 cm height, matched to the height of the metal plate ahead. We determine the baseline from the part of the laser lying on the metal plate.

Furthermore, we aim to compare the result of our particle flux measurement with theoretical predictions for the saturated flux of bedload. Duran et al. [113] provide the expression for this in their work on the numerical approach for sediment transport:

$$q_{sat} \propto \Theta^{3/2} \sqrt{\left(\frac{\rho_p}{\rho_f} - 1\right) g d^3} \tag{3.4}$$

with the Shields number Θ, the densities of the particle ρ_p and fluid ρ_f respectively, the gravitational acceleration g and particle diameter d.

Comparison to Numerical Simulation and Subaqueous Experiment

We shall classify our results by comparing them to numerical simulation results by Parteli et al. [99] and the results of water-tank experiments performed by Reffet et al. [101], shown in figure 3.4. The numerical simulation results by Parteli et al. [99] and the linear stability analysis of transverse dunes performed by Melo et al. [100] show that transverse dunes with respect to any along-axis perturbation are not stable [99, 100]. The transverse instability is due to lateral sand transport by avalanches at the slip face [99, 100]. Thus, a transverse sand bar migrating on bedrock in an area of low sand availability breaks completely into chains of barchans [99, 100]. We will compare our results with the results shown in figure 3.4.

In addition, we will analyze the measured lengths and widths of the bedforms to estimate the saturation length. For this, we use the equation (1.28) introduced in section 1.4, where the maximum wavelength $\lambda_{max} \sim 12 l_{sat}$ was estimated from the maximum growth rate of authors Elbelrhiti et al. [55] and an estimate of the minimum width $W_{min} \sim 12 l_{sat}$ of a dune from authors Parteli et al. [62].

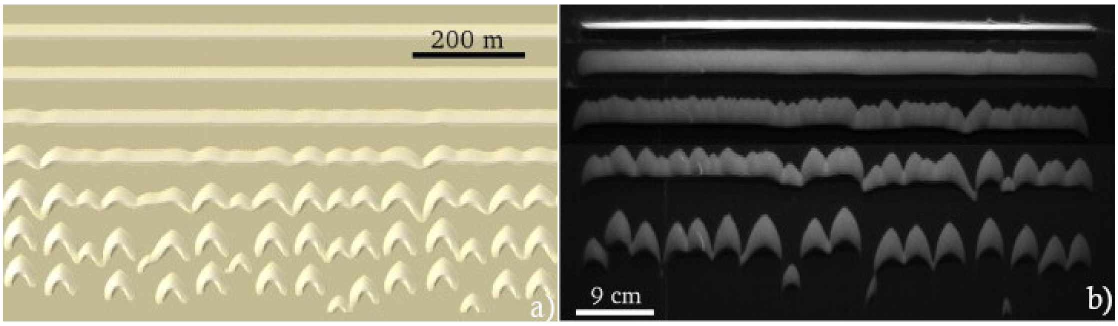

Figure 3.4.: Transverse instability of dunes from (a) numerical simulations [99]: the evolution of a transverse dune at different times evolving under unidirectional wind, decaying into a chain of barchans. b) water-tank experiments [101]: a transverse dune decaying into barchan chains. Images credit: Sylvain Courrech du Pont; Laboratoire MSC (Matière et Systèmes Complexes), UMR 7057, Université Paris Diderot, Paris, France. Reused with permission from Ref [100]. Copyrighted by Elsevier.

3.3. Results

3.3.1. Incipient Bedform Growth under Unidirectional Wind

Figure 3.5 shows the evolution of a rectangular flat particle bed of coated hollow microspheres into two transverse bars under wind exposure. The white arrow gives the wind direction; we note the experiment time in the left corner of each image. The black dots on the test surface are each 5 cm apart and help to evaluate migration distances during an experimental run.

After turning on the airflow, structures emerge from the flat particle bed, forming sinuous crests transverse to the wind direction. Within 20 seconds, three parallel fronts develop (t= 60 s): the first, corresponding to the rearmost front, has a regular gentle crestline; the second central front, which has a stronger sinuous crestline; and the third, corresponding to the leading edge of the flat particle bed, which shows a jagged crestline.

Starting with the fourth image, the bed breaks up along the crestline, and centimeter-sized bedforms detach from the leading front. The morphological characteristics of the single bedforms are a crescent-shaped body and crest, preceding horns that face downwind. Based on the morphological similarity to barchan dunes and the centimeter-sized dimensions of a ripple, we referred to the resulting individual bedforms as barchan-ripple (see section 1.5). Within 20 seconds, the barchan-ripples still attached to the central front detach and migrate downwind, first as barchanoids and then as individual barchan-ripples. At the same time, two transverse, parabolic bars form along the back two crests, developing a distinct zone without particles. At the leading edges of the bars, barchan-ripples detach and migrate downwind. Almost all these individual barchan-ripples have either trailing arms (wings) pointing upwind or a slightly extended arm pointing downwind. The rearmost edge of the initially flat bed features several millimeter-sized indentations on the surface over 160 seconds; the last bar is still in its initial starting position in the last image.

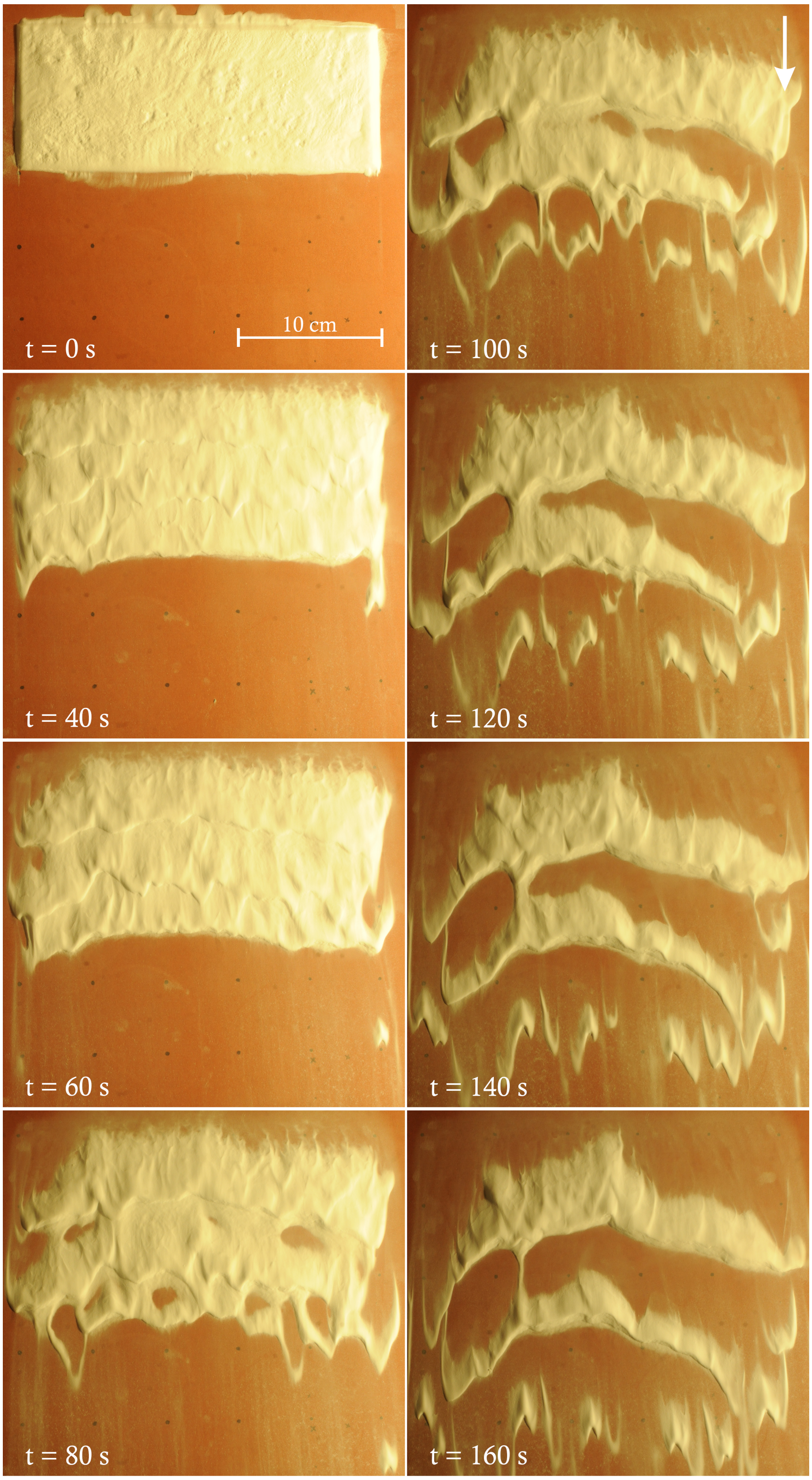

Figure 3.5.: Evolution of a rectangular flat particle bed of coated hollow microspheres into two transverse bars under wind exposure. The white arrow indicates the wind direction; experiment time is noted in the respective lower left corner. Three parallel fronts develop: barchan-ripples detach from the leading front and migrate downwind, while the other two fronts transform into transverse bars.

3.3.2. Formation of Aeolian Barchan-Ripples

Figure 3.6 focuses on the decay of the central transverse bar into barchan-ripple chains and finally into individual barchan-ripples. In the inset, the redrawn contours represent the bedforms shown in the main image, color-coded corresponding to their timeline. The topmost image shows a mixed form of transverse bar and various broad barchan-ripple chains, which decay after 100 seconds into two barchan-ripple pairs and three single ones.

Figure 3.7 shows an enlarged version of the inset in figure 3.6 with an additional position of the transverse bar (in dark green) to detect and measure the migrated distance at the onset. In the background of the bedforms, we see the wind speed matrix from section 2.3. The total width of the transverse bar stretches across different speed zones, which we discussed in detail in section 2.3.3.

Parteli et al. [99] propose an upper boundary for the length at which the transverse dune destabilizes:

$$L_\infty \leq cL_0 \ln(H/z_0) \tag{3.5}$$

with L_0 the length from the barchan's back to the slip face, the width-to-length ratio $c = W/L_0$, the barchan's height H, and the roughness length z_0. We measured a roughness length for our system in section 2.17 of 35 µm. With the laser method, we measured the maximum height of a single barchan-ripple, which is approximately 3 mm. From figure 3.6 we obtain approximately a width of 2 cm and a length L_0 of 3.5 cm, i.e., $c \approx 0.57$. From these values, we can estimate an upper boundary for the destabilization length of:

$$L_\infty \leq 0.57 \cdot \ln\left(\frac{3\,\mathrm{mm}}{35\,\mu\mathrm{m}}\right) \approx 2.6L_0 = 9\,\mathrm{cm}. \tag{3.6}$$

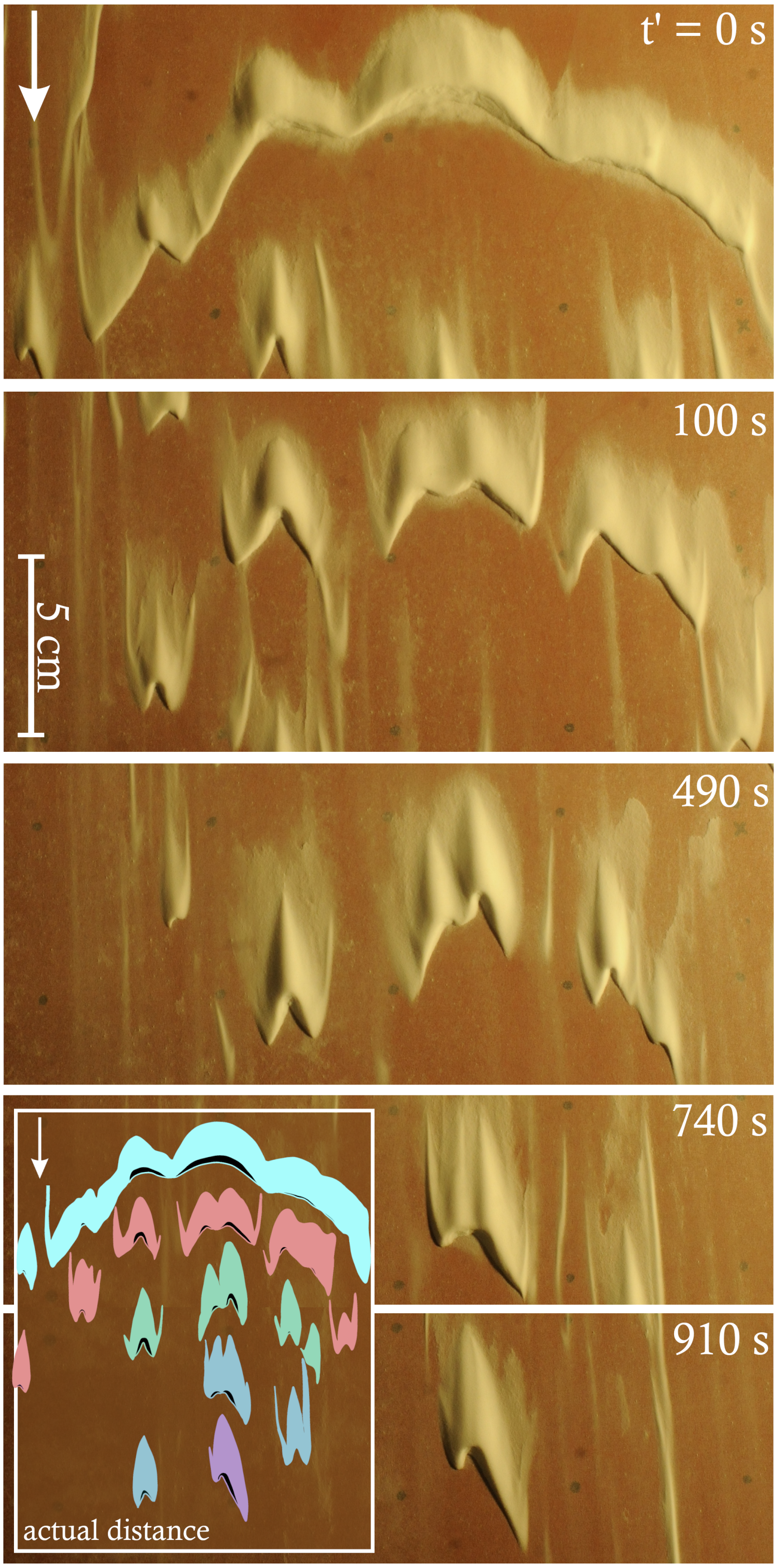

Figure 3.6.: Central transverse bar breaks into barchan-like chains; a single barchan-like bedform is left after 910 s. The time difference between successive images corresponds to one turnover time. The inset shows the bedforms actual distance and is color-coded to distinguish their timeline. The time t' corresponds to $t = 160 + t'$.

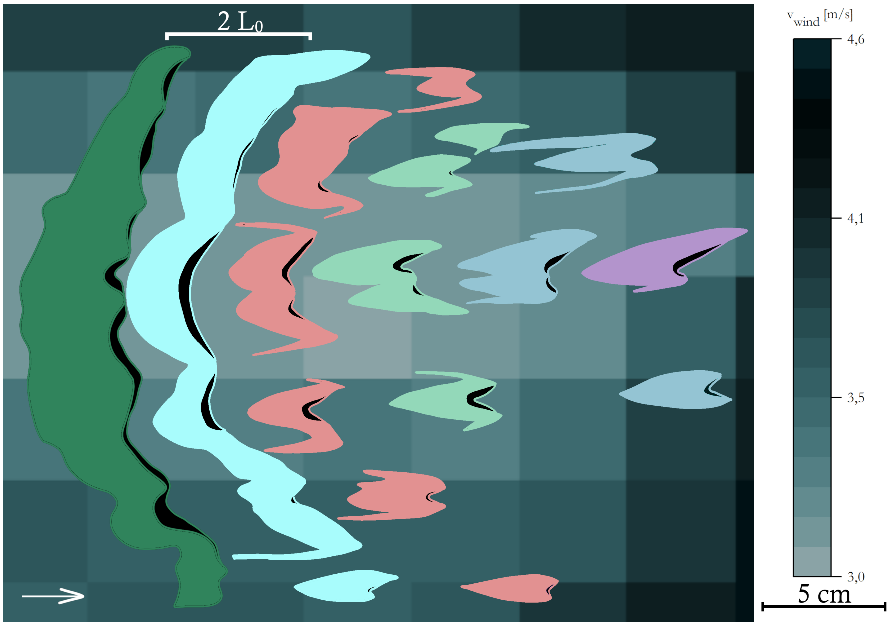

Figure 3.7.: Outlines of bedforms with the wind speed matrix in the background (from section 2.3); the right bar gives the color-coded velocities (one square is $\sim 5\,\mathrm{cm}$) and the white arrow the wind direction. The transverse bar is located in different speed zones and travels approximately $2L_0$ before breaking into barchan-ripples, where L_0 is the distance from the barchans' back to the crest.

Figure 3.8 shows the evolution of the center of the rearmost transverse bar into a chain of three barchan-ripples. The time t^* corresponds to $t = 140\,\mathrm{s} + t^*$; the inset is used to estimate the distances and corresponds to the first and the last two images. Within 15 min, the bedform migrates a total of 15 cm downwind. In these six images, we can follow the onset of barchan-ripple evolution: from an irregular transverse bar, a roundish, broad barchan-ripple develops at first, with narrow horns and a small slip face, subsequently broadening by a factor of three. Within a minute, the broad transverse arm attached to the right side of the body detaches and evolves into a smaller barchan-ripple with an elongated right arm. The last two images show the decay into a two-chain barchan-ripple, catching up with the preceding one at the edge and then merging into a chain of three barchan-ripples, all of approximately 4 cm length.

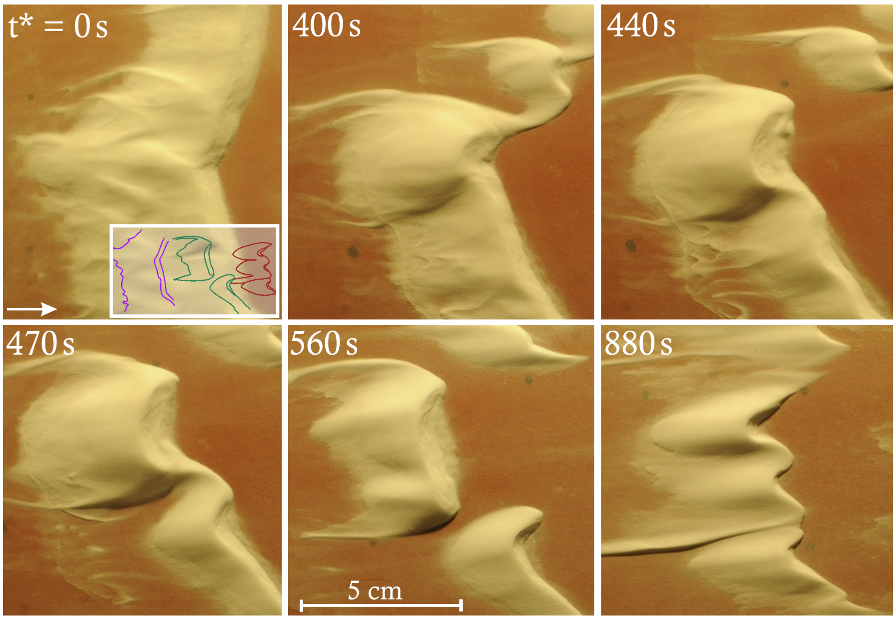

Figure 3.8.: Evolution of the central rearmost transverse bar into a chain of three barchan-ripples. The time t^* corresponds to $t = 140\,\text{s} + t^*$; the inset shows the outlines of the first and last two bedforms to simplify the estimation of distance. The white arrow gives the wind direction, and the scale is valid for all images. We can follow how the transverse bar breaks successively into a chain of barchan-ripples, migrating a total of 15 cm downwind.

A comparison between chains of barchans, all evolved from a transverse bar in (a,b) our wind tunnel, (c,e) in a water tank experiment, (d,f) as a results of numerical simulations is shown in figure 3.9. The morphology of all three results is comparable. We know, that the maximum wavelength λ_{max}, derived by the maximum growth rate [55] (see section 1.4), is proportional to the saturation length l_{sat}:

$$\lambda_{max} \sim 12 l_{sat}. \tag{3.7}$$

From this equation we estimate $l_{sat} \sim 2.5\,\text{mm}$ for our system. This estimation can also be made by using the width W of the bedforms, as suggested by Parteli et al. [62]. There, the width of the smallest barchan, W_{min}, is approximately $12 l_{sat}$. Since the barchans shown in figure 3.9 are not the smallest bedforms we observe, we have to measure the width of the smallest migrating bedform with horns [62]. With a width of $W_{min} \sim 1.5\,\text{cm}$ we obtain a saturation length of about 1.3 mm.

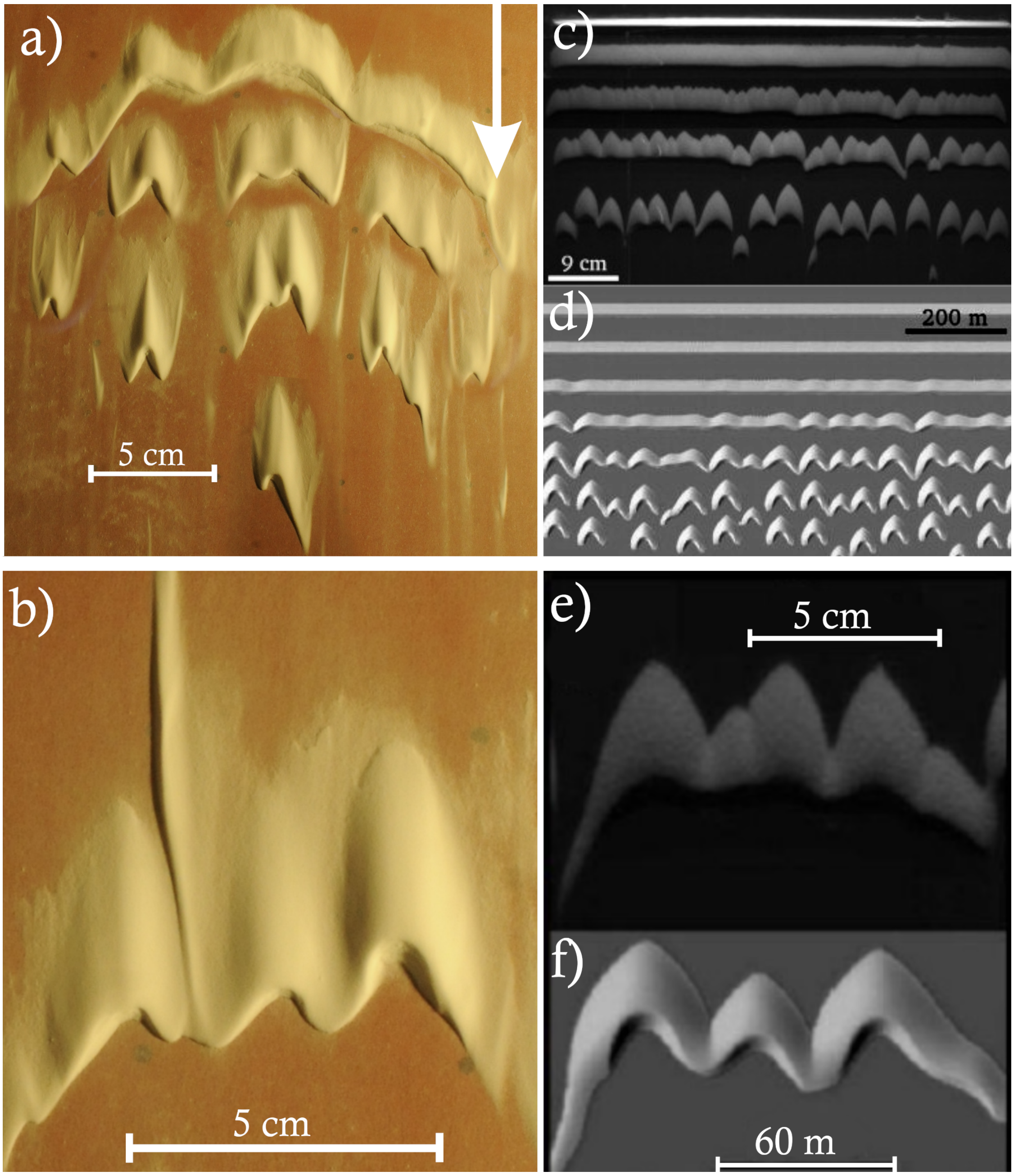

Figure 3.9.: Transverse bars decaying into chains of barchans: in the wind tunnel (a,b), a water tank experiment (c,e), and numerical simulation (d,f). The results from two laboratory experiments under aeolian and subaqueous conditions and a numerical simulation result show the same morphological evolution. Figures from the right column are adapted with permission from Ref. [99].

3.3.3. Particle Flux Measurement

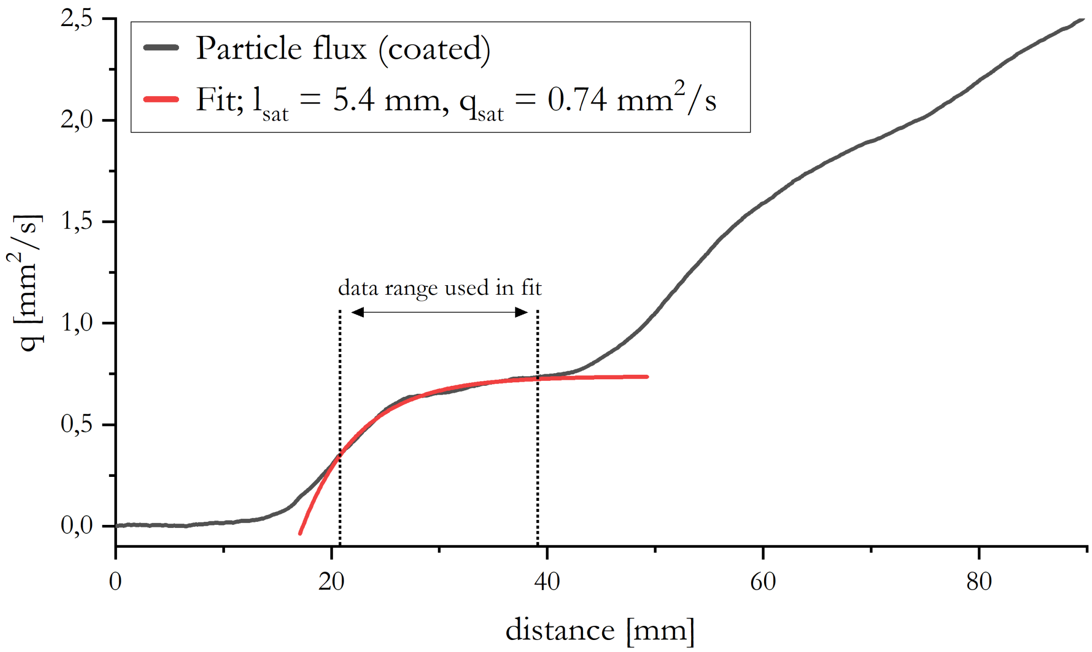

Figure 3.10.: Particle flux $q(x)$ over a flat particle bed of coated hollow microspheres as calculated from the bed height changes using eq. 3.2. Solid red line gives the best fit to the data range (dotted lines) up to the first saturation of the particle flux; the particle bed starts at $x \approx 15\,\text{mm}$. A saturation plateau of 10 mm width is followed by a slightly oscillating behavior of the flux curve. From the fit we obtain a saturation length of 5.4 mm with a local saturation flux of $q_{sat} = 0.74\,\text{mm}^2\,\text{s}^{-1}$.

Figure 3.10 shows the particle flux $q(x)$ over a flat particle bed of coated hollow microspheres as a function of the distance from the windward edge of the particle bed. We calculated the particle flux from the bed height equation (3.2); the solid red line gives the best fit to the data using equation (3.3) up to the first saturation of the particle flux. The dotted lines show the data range we used for the fit; the particle bed starts approximately at x=15 mm. The flux increases in the first 10 mm after the leading metal plate and reaches a plateau of approximately 10 mm width. After that, the flux increases further; overall, we observe a slightly oscillating behavior of the flux curve. The obtained values for the saturation length l_{sat} show the wind saturates within 5.4 mm over the particle beds used in the experiments, with a saturation flux of $q_{sat} = 0.74\,\text{mm}^2\,\text{s}^{-1}$.

We shall compare this value with a prediction of the saturated flux in the bedload regime. For our particle system, equation (3.4) yields:

$$q_{sat} \propto \Theta^{3/2}\sqrt{\left(\frac{\rho_p}{\rho_f}-1\right)gd^3} = 0.2^{3/2}\sqrt{196\cdot 9.81\frac{m}{s^2}\cdot 43\,\mathrm{\mu m}^3} \sim 10^{-6}\mathrm{m}^2\,\mathrm{s}^{-1} \tag{3.8}$$

with the Shields number Θ, the densities of the particle ρ_p and fluid ρ_f respectively, the gravitational acceleration g and the particle diameter d [113]. The predicted saturation flux order of magnitude agrees with the measured local saturated flux.

3.4. Discussion

Starting with a 1 cm high flat particle bed of coated hollow glass microspheres, we observe the instability of the entire bed under aeolian conditions. First, the bed destabilizes into two transverse bars that migrate downwind, decay into multiple barchan chains, and finally into individual migrating barchans.

The parabolic shape of the transverse bars results from the lateral wind gradient on the test surface; consequently, the edges are located in velocity zones with slightly higher wind speeds and migrate downwind faster, as can be seen in figure 3.7. We observe the transverse instability from the decay of the transverse bars into barchan chains. For the predicted upper boundary of the destabilization length we obtain:

$$L_\infty \leq 9\,\mathrm{cm} \sim 2.6L_0 \tag{3.9}$$

which is in agreement with our measurements of approximately $L_\infty \sim 2L_0$.

Our results indicate a millimeter-sized saturation length l_{sat}. We know that l_{sat} defines the minimum length scale below which a heap will erode [56]. The maximum sediment flux must be positioned upstream of the crest for a heap to grow, where sediment deposition occurs. The formation of bedforms from a flat particle bed migrating downwind independently and self-organized suggests a saturation length of several millimeters. The barchan-ripples seem to maintain their lengths and widths and have a distinct body shape. Estimating the saturation length from the maximum wavelength and minimum width also indicates a millimeter-sized value for l_{sat}.

We measured the particle flux over a coated flat particle bed derived from height changes and showed that the flux exhibits a non-trivial saturation behavior. Overall, the flux did not saturate within the length scales accessible in our experiment. Instead, we observe an oscillating behavior with local saturation plateaus. The saturation length resulting from these plateaus is in the order of a few millimeters. Comparing the measured saturation flux values with the predicted saturated flux for bedload shows that the orders of magnitude of the saturated flux and the calculated theoretical value are comparable.

The origin of this non-monotonic saturation still needs to be clarified and may be related to details of the setup used. However, the measured data clearly show that the particle flux has a saturation plateau along an unsaturated overall flux curve. We suggest that this flux behavior indicates two transport mechanisms at work in our experiment: suspension and bedload transport. From our calculations in section 1.5 and our results in section 2.3, we found a viscous sublayer thickness of about $\sim$ 70 µm for our particle system at a wind speed of approximately $3\,\mathrm{m\,s^{-1}}$. In these sections, we also argued that we should observe viscous bedload transport based on the calculations since our particle diameter is smaller than the viscous sublayer thickness, and thus bedload transport should be possible. The potential cause for the occurrence of suspension could be fluctuations in wind speed, which have a strong effect on the thickness of the viscous sublayer. A minimal change in wind speed may already decrease the thickness of the viscous sublayer to the particle diameter, which means that the particles are directly entrained in suspension due to their properties (low density, small diameter). Therefore, we assume that the unsaturated flux, which increases steadily and does not saturate in our wind tunnel scales, corresponds to the suspension flux. Direct measurements of the saturation length for the transport mechanism bedload are challenging since the length is typically comparable to the grain size [10]. Nevertheless, the estimates of the saturation length from the morphological observation and the direct measurement suggest an order of magnitude of millimeters, and thus a longitudinal instability observable in the length scales available to us.

Finally, the morphological similarity of the barchan chains and the agreement of the predicted length scales at which the transverse bars decay into barchans strongly supports that our bedforms are subject to the same longitudinal instability and transverse instability as subaqueous ripples and aeolian dunes.

Our results also highlight the need for further investigation to confirm and test several hypotheses. For example, the denotation of the bedforms as barchans misses a more precise characterization of the centimeter-sized bedforms. Similarly, the question arises as to which transport mechanism dominates in our wind tunnel and is responsible for particle transport. The flux measurements give first indications but are challenging to interpret and require confirmatory measurements.

3.5. Conclusions

In conclusion, we showed that a flat particle bed of coated hollow microspheres is unstable under aeolian conditions, and transverse bars form and decay into barchan chains after a length of approximately $2L_0$, where L_0 is the barchan's length up to its crest. We show the onset of two transverse bars decaying into barchan chains within a length that is predicted by authors Parteli et al. [99], supporting numerical simulation results that predict this transverse instability. We derived a saturation length in the order of millimeters from the dimensions of the barchan-ripples using two different theoretical expressions.

Furthermore, we compare the barchan chains evolved in our wind tunnel with the results of subaqueous experiments and numerical simulations to show a remarkable morphological similarity. Our results support that barchan bedforms are subject to two different types of instability: the longitudinal and the transverse instability.

Finally, we measured the particle flux over a bed of coated hollow glass microspheres and found an unexpected non-trivial saturation behavior. We identified a local saturation from the oscillating flux curve and derived a saturation length of several millimeters, which agrees with our previous results and calculations. Furthermore, we suggest that the particle flux curve indicates two transport mechanisms prevalent in our experiment: bedload transport and suspension.

The challenging interpretation of the complex particle flux curve underlines the necessity to study the transport mechanism in more detail. In addition to a particle transport near the bed, the particles also appear to go into suspension, an observation that measurements will further illuminate in the next chapters. With a size of a few centimeters, single bedforms should also emerge from small heaps, which we will examine in the next chapter. Earlier experiments starting from a spherical particle bed are shown in the outlook of this work.

4 Evolution of a Migrating Aeolian Barchan-Ripple

A centimeter-sized barchan-ripple that evolved in the wind tunnel

'The geomorphologist, aware of the vast periods of time during which his processes have acted, is rightly doubtful of the ability of the physicist and the chemist to imitate them usefully in their laboratories.'

R.A.Bagnold (1941)

The study of sedimentary bedform formation in the laboratory presupposes a saturation length that is on the order of the accessible length scale. Under aeolian conditions the saturation length ranges typically from 50 cm to 1 m. Here we show that a particle heap of coated hollow microspheres evolves into a self-organizing, migrating barchan-ripple under aeolian transport and is governed by the same instability mechanism as subaqueous ripples and aeolian dunes. We show the evolution from a transient onset to a steady state, in which the morphology of the barchan-ripple remains unchanged over several turnover times. Height measurements show growth during the transient phase, which is an indicator for a saturation length of a few millimeters. The height profiles along the central line verify the stability of the barchan-ripple as soon as it reaches a steady state. The calculations of characteristic parameters of the centimeter-sized structures are in agreement with theoretical predictions and underline the validity of current transport and bedform formation models.

4.1. Introduction

In section 2.2, we introduced a particle system, which we used to form flat particle beds in chapter 3, and observed the onset of instability and the formation of bedforms under wind exposure. We determined the saturation length using two measurement methods: indirect, via length and width measurements and the comparison to predictions and direct measurement of the local saturated particle flux. A reduction of the saturation length to a millimeter scale and the appearance of barchan-ripples over the entire test area suggest that the centimeter-sized bedforms may also arise from single heaps.

After introducing the experimental methods, we will follow the evolution of a particle heap of coated hollow microspheres in detail. For this purpose, we first show superimposed images in a time-lapse sequence and follow the evolution steps of the barchan-ripple from the onset. Then, we map the dimensions of the structure, measure the maximum height, and show the evolution of the height profile up to its steady state form. Furthermore, we will show that even from an irregularly shaped initial pile, a barchan-ripple eventually emerges again. Finally, we relate our bedforms to subaqueous ripples and aeolian dunes by comparing characteristic length predictions with our results.

4.2. Experimental Methods

We prepared coated hollow glass microspheres (HGMs), following the protocol in section 2.2.3, which includes mixing the HGMs with the flowing agent, vacuum oven treatment at 200 °C for 30 min, sieving, resting for three days, reheating for 30 min before an experimental run. The particles were placed on the test surface through an hourglass-shaped double-funnel, as sketched in figure 4.1. This has two advantages: we can place a precise heap and avoid a high flow rate of impacting particles on the heap. With this technique, we placed particle heaps with an initial diameter of 5 cm and a volume of approximately 8 mL onto the test section.

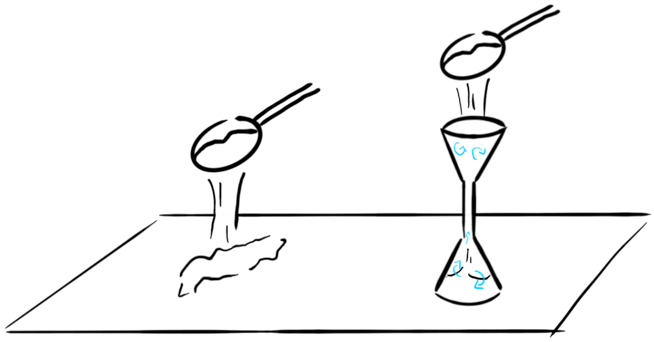

Figure 4.1.: A comparison between two different placement techniques. Left: pouring the material with a measurement spoon will lead to a high flow rate of impacting particles on an irregular heap. Right: an hourglass-shaped double-funnel simplifies a precise placement and helps maintain a low flow rate while pouring the material from the measurement spoon.

We image the entire test area with a Nikon D3 camera from the top in a 5 sec interval. A spotlight illuminates the test area from one side. Alternately we switch the line laser on every 10 sec to record a laser image of the structure for the height profile measurement. The setup is sketched in figure 4.2.

With an image analysis program (GIMP) [110], we analyze the lengths and widths of all bedforms. We obtained the height profiles of the central line from simple intensity peak picking of the images and triangulation, as described in the method section in chapter 3. The line lasers' angle of incidence α with respect to the test section and the distance to the baseline gives us the height at a specific point, see equation (3.1), from which we obtain a height profile along the line in wind direction. During an experimental run, we move the laser along the migration path of the bedform. This can lead to an angular displacement of the laser, which results in a height error. The inaccuracy is $\Delta h = 0.2\,\mathrm{mm}$ for a deviation of one degree.

The initial position of the particle heap corresponds to the position chosen in section 2.3.3 for the vertical velocity measurement and is marked in the inset of figure 2.13 (red dot). The prevailing wind speed 1 cm above the surface was $2.6\,\mathrm{m\,s^{-1}}$ (45% fan setting), the flow being neither stopped nor interrupted for the entire duration of the experiment ($\sim$57 min).

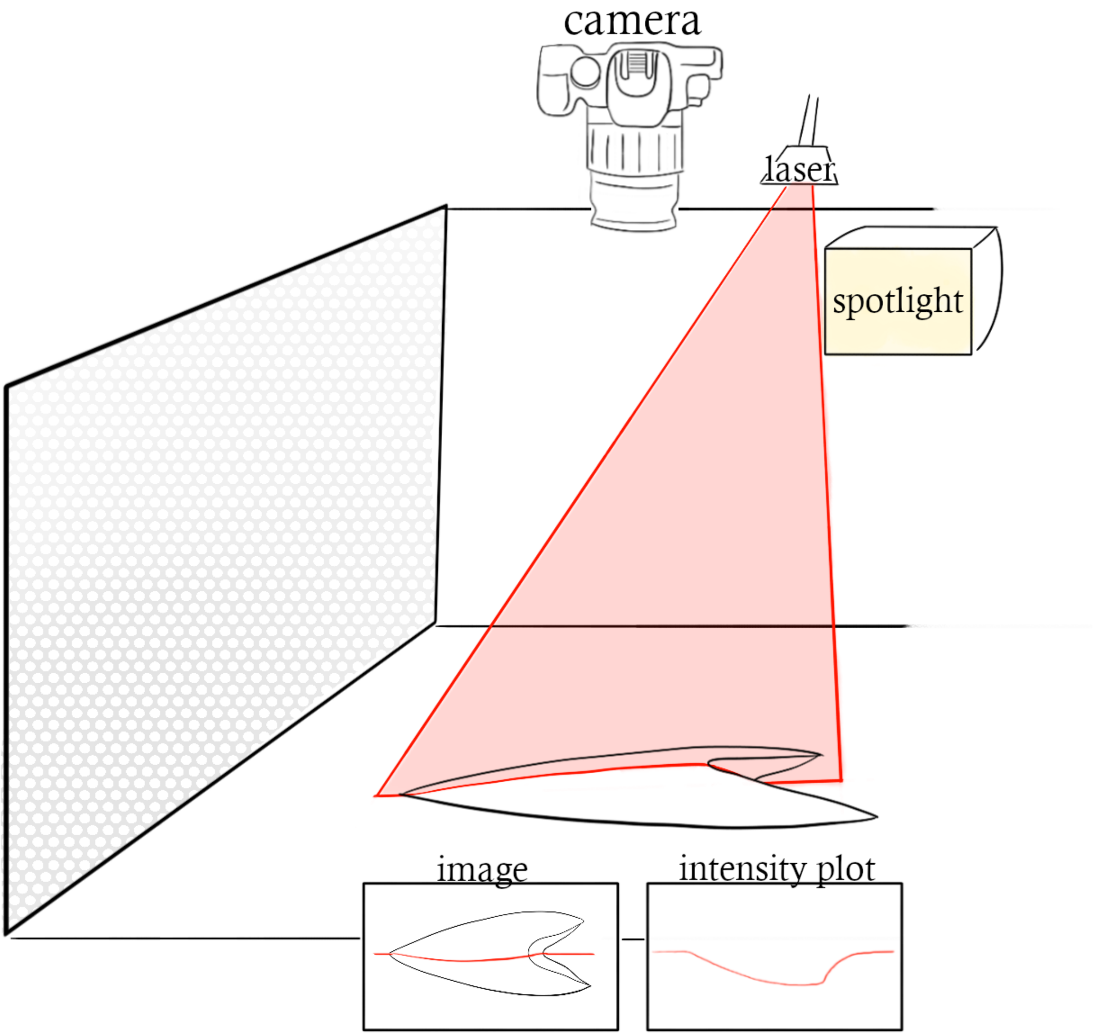

Figure 4.2.: Sketch of setup in the wind tunnel and the placement of the line laser on the heap. We obtain the structures' height by image analysis, intensity peak picking, and triangulation. Dimensions are not to scale. The inset shows a scheme of the image we obtain and the intensity plot.

4.3. Results

4.3.1. Morphology from Transient Onset to a Steady State

Figure 4.3 shows superimposed, time-lapsed images of a single particle heap, which evolved into a self-organized bedform under aeolian conditions. The white arrow indicates the wind direction. The turnover time, i.e., the time the particle heap needs to leave its initial position, is indicated below the image. The images are shown in actual distance, and the scale is given in the upper right corner. The

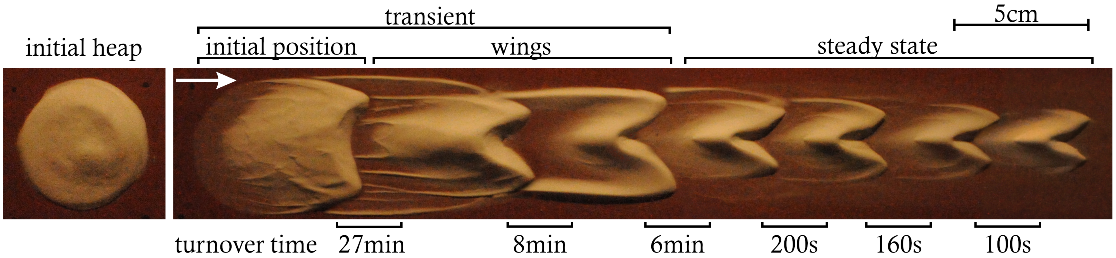

Figure 4.3.: Superimposed images of a single particle heap evolving into a self-organized bedform under aeolian conditions at a wind speed of $2.6\,\mathrm{m\,s^{-1}}$. The initial heap before wind exposure is shown on the left side, separate from the images taken after wind exposure. The white arrow indicates the wind direction; the turnover time is the time in which the barchan travels its own length. The scale is given in the upper right corner, all images, except the initial heap, are shown in real distance. The initial heap has an diameter of 5 cm; the barchan has a total length of 3 to 4 cm. The bedform enters a steady morphological state after leaving the transient phase, where its shape undergoes two significant changes (see text).

particle heap left its initial position after 27 minutes. The turnover time decreased successively and equaled 100 seconds at the end of the experiment. The bedform has a crescent-shaped body and crest; at first roundish and after one turnover time V-shaped. We see leading horns on the left and right sides of the body, and after the third image from the left, trailing arms (wings) pointing upwind extend beyond the bedform's body, leaving material deposits attached to the horns. The wings already developed after we took the second image from the left, which is why we assigned the bedform to the wings phase. After the crescent crest, we see an area with particles on the downwind side in between the horns. Up to this point, we classify the bedform as transient. After this, the bedform loses its wings, although some residual material remains attached to the horns. We refer to the second phase of the experiment as steady state, so far, only because its morphology does not change across three bedform lengths. This chapter will present further results that underline that this is a steady state.

In figure 4.4 we introduce the bedform's characteristics in a scheme. The laser line is placed on the bedform's central line to obtain a height profile. We distinguish between the total length L, which includes the length of the horns, and the length from the bedform's back to the crest. The total width W includes the wings; we

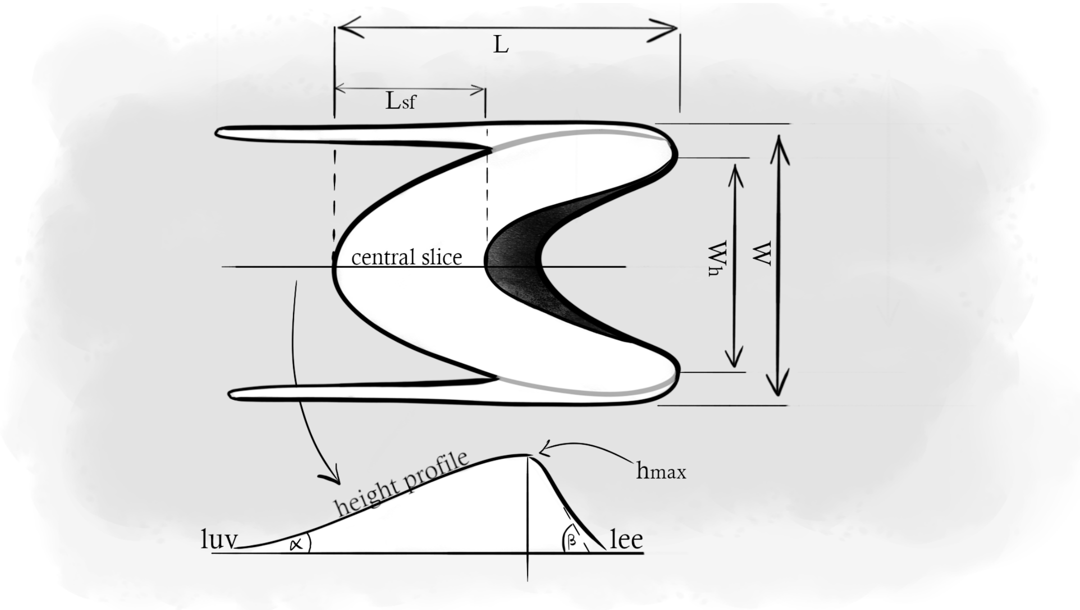

Figure 4.4.: Schematic drawing of bedform's characteristics: the total length L, the length from the barchans' back to the crest L_{sf}, the total width W and the horn width W_h. The laser line is placed on the central slice for the height measurements.

do not take them into account for the horn width W_h. We get the luv (upwind), and lee (downwind) angles from the elevation profiles. The maximum height h_{max} corresponds to the highest elevation measured from the height profile. The slip face is on the leeward side, and the slope corresponds to the material's angle of repose.

Figure 4.5 shows the bedform's lengths and widths measured from the captured images over the entire duration of the experiment. The measured dimensions are introduced in figure 4.4. The measurement error is Δ =2 mm and on the order of the symbol sizes. The first vertical line in figure 4.5 (t =35 min) marks the time at which the bedform leaves its initial position for the first time, which corresponds to the second image from the left in figure 4.3. The bedform's total length increases

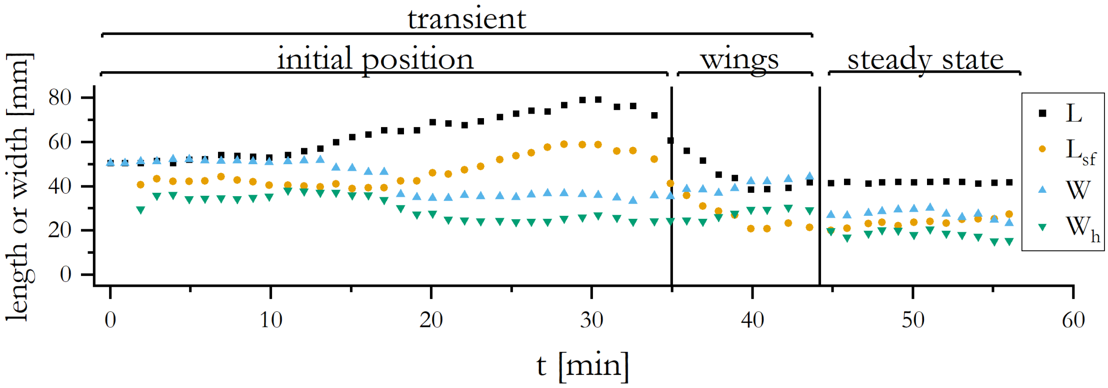

Figure 4.5.: The bedform's lengths and widths over the entire duration of the experiment. The bedform's body length increases while it is still in its initial position and remains constant in the last 20 minutes of the experiment. The width decreases slightly after 20 min, fluctuates, and remains constant as soon as the bedform is in the steady state. The errors are on the order of symbol size.

during the course. As soon as it leaves the initial position, the length of the bedform shortens and then remains constant until the end of the experiment. The same course is observed for L_{sf}. The total width W does not change in the first phase of the initial position, then decreases by a few millimeters, remains constant in the further course until it loses the wings shortly before t =45 min, where its width decreases. W_h has a similar evolution.

4.3.2. Height Profiles of the Central Slice

Figure 4.6 shows the maximum height of the bedform plotted against time. The markings and labels are the same as in figure 4.5; the yellow dots show the bedform's height corresponding to the images shown in figure 4.3. As described in the methods section, the measurement uncertainty is Δh = 0.2 mm. The height of the initial heap was 5.15 mm. The first data point corresponds to the height of the initial pile

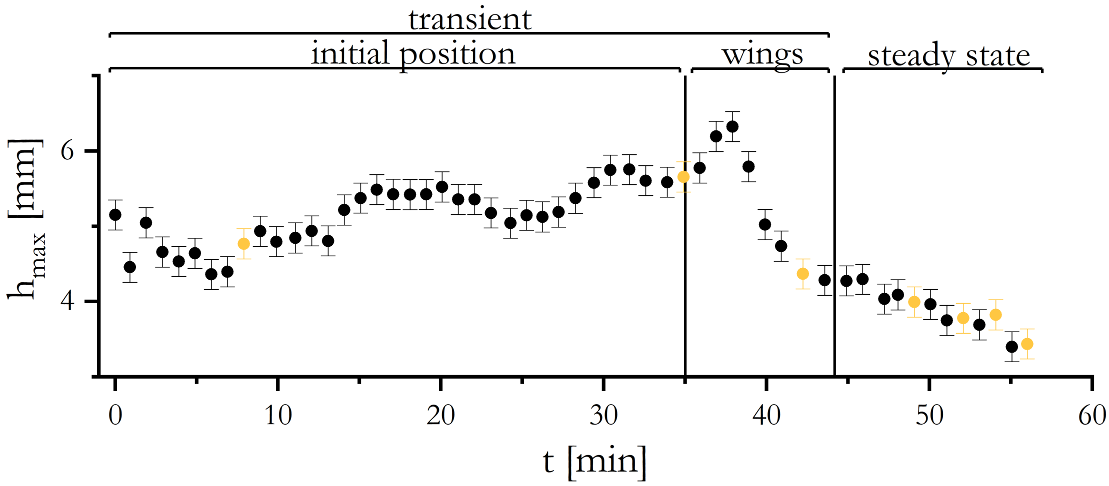

Figure 4.6.: Maximum heights h_{max} of the bedform throughout the experiment. Yellow dots correspond to the bedform's height shown in figure 4.3. The height fluctuates and reaches its total maximum of 5.54 mm after the bedform has left its initial position. The bedform's height then decreases rapidly by about 1.5 mm in under 5 minutes. In the steady state, the decrease in height continues slowly.

before wind exposure. We observe a reduction in height shortly after turning on the flow to 4.45 mm within one minute. In the initial position, the height fluctuated and reached its total maximum of 5.54 mm in the wings-phase just before $t = 40$ min. At this point, the bedform grew by 20% of the height it had one minute after the start of the experiment. After the total maximum is reached, the height decreases slowly without fluctuations to a value of approximately 3 mm.

Figure 4.7 shows three height profiles of the bedforms along the central line, as indicated in figure 4.4. A superimposed, time-lapsed image in the background shows the bedforms five seconds before the laser image. The horizontal line marks the first bedform's maximum height of 4.5 mm. The height fluctuates slightly upwind in the first height profile and is followed by a 1 cm long plateau. The angles α and β measured from the elevation profiles (see fig. 4.4) yield a gentle slope of $\alpha = 8.2°$ and a steeper slope upwind of $\beta = 30.1°$ degrees. The central height profile shows a similar course, but the bedform grew in height; the maximum height equals 5.5 mm. The slope upwind changed to $\alpha = 9.8°$; the steeper downwind slope is still $\beta = 30.1°$. While the first two height profiles show a distinct asymmetrical shape, the third is more symmetrical in comparison. The laser line in the last profile lay partially on the narrow horns downwind, which results in a slight dip in height at the end of the profile. We constructed a straight line to avoid biasing the result (see dashed line in figure 4.9). With this method, we obtain an angle of repose of 31 degrees. The images in the background show the difference in surface texture

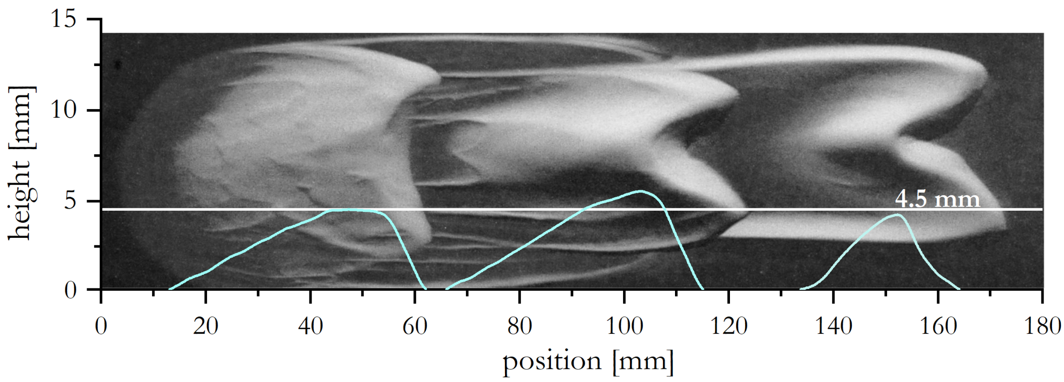

Figure 4.7.: Height profiles of the bedform along the central line in the transient regime. A superimposed image in the background shows the corresponding bedform shape (W $\sim$ 4 to 5 cm). The vertical line depicts the maximum height of the first profile. After a first height growth, the bedform decreases to its initial height.

between the first bedform and the other two. In the first image, we can see small indentations at irregular intervals on the surface, causing a shadow resulting from the illumination. As soon as the bedform leaves its initial position, we can no longer observe this phenomenon. The middle bedform seems to be surrounded by material deposits, and the back also shows small remnants of surface indentations. In the last image, the surface of the bedform is uniformly smooth. The wings attached to the horns have a sharp edge where the material deposits on both sides perpendicular to the wind direction.

In figure 4.8, we applied the same plot concept as in figure 4.7 with the bedforms in the steady morphological state. The vertical line marks the maximum height of the first bedform, which is 4.1 mm. After that, the overall height decreases, but the profile remains nearly unchanged. The maximum height of the last two bedforms is 3.4 mm. The four profiles result in mean luv slopes of 11.1 degrees and an angle of repose on the leeward side of 31 degrees. Table 4.1 summarizes the measured values and gives the central slice area, which we obtained from integrating the

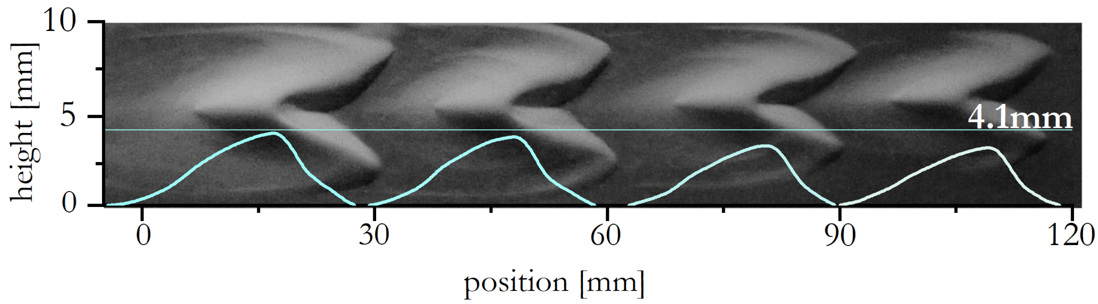

Figure 4.8.: Height profiles of the bedform along the central line in the steady state regime. A superimposed image in the background shows the corresponding bedform shape (W $\sim$ 3 cm). The bedform loses height while maintaining its height profile shape.

area under the height profiles' curve. Figure 4.9 shows the four steady state height

profile	luv angle α [°]	lee angle β [°]	central slice area [mm^2]
transient			
1	8.2	30.1	130
2	9.8	30.1	145
4	16.8	29.6	60
steady state			
1	12.1	32.3	52
2	11.3	32.9	50
3	11.0	29.2	42
4	10.1	29.6	42

Table 4.1.: Luv and lee slopes, and the integration area of the central slices measured and obtained from the height profile data. The measurement error for the slopes is $\Delta\alpha = \Delta\beta = 0.5°$.

profiles, rescaled by the maximum height and its position. We see, that the height profiles match apart from minimal deviations on the upwind and downwind edges and follow the same curve.

4.3.3. Evolution of a Larger, Irregularly Shaped Heap

Figure 4.10 shows a superimposed image of an experiment evolved from an irregular-shaped, large initial pile. The actual distances are shown in the scheme. The available

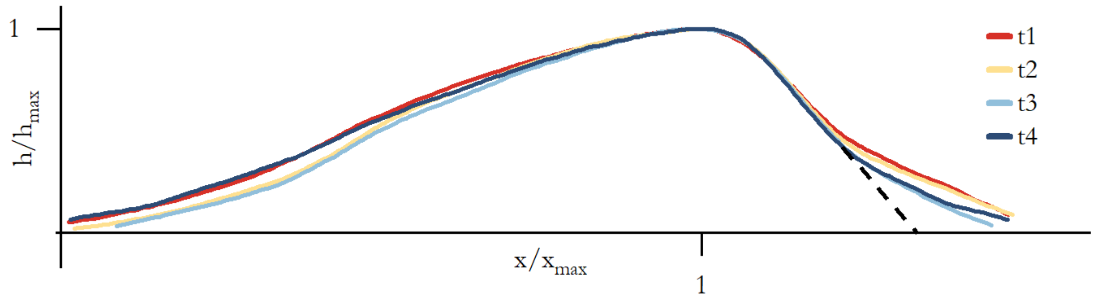

Figure 4.9.: Rescaled steady state height profile curve. t1 corresponds to the first height profile. Apart from minimal deviations on the upwind and downwind edges, the height profiles follow the same curve. The dashed line indicates the line we draw to calculate the angle of repose.

quantity of material is about ten times as much as in the previously presented experiment, and the wind velocity is $4.1\,\mathrm{m\,s^{-1}}$ (60% fan setting). In the first picture,

Figure 4.10.: Bedform evolving from an irregular-shaped, large initial pile under a wind velocity of $4.1\,\mathrm{m\,s^{-1}}$. The inset shows a scheme of the bedform's actual distances. The white arrow indicates the wind direction. The initial volume is approximately ten times higher than in the previous experiment (figure 4.3). A large crescent-shaped bedform evolves after the initial position is left and is followed by further significantly mass loss. In the last picture, a 4 cm long steady state bedform is shown.

we see a bedform with a smooth surface on the windward side. On the lee side, longitudinal, evenly spaced bedforms are formed, with small amounts of material detached from the ends. From this structure, a large crescent-shaped bedform evolves, with a width of 5 cm and a total length of about 9 cm. Then, the bedform loses considerable mass in a short time, the horn width increases, and the body shortens. Finally, the last picture shows a 4 cm long bedform, similar to the one previously observed.

Figure 4.11 shows close-up perspective photos of the bedform in the last photo in figure 4.10. The surface is smooth, and the V-shaped body of the bedform is more elongated than in the first experiment presented. We observe no significant deposits of material on the horns' sides. The bedform has a sharp crest, followed by a slip face. Our measurements of the slope angle at the central slice give 31 degrees.

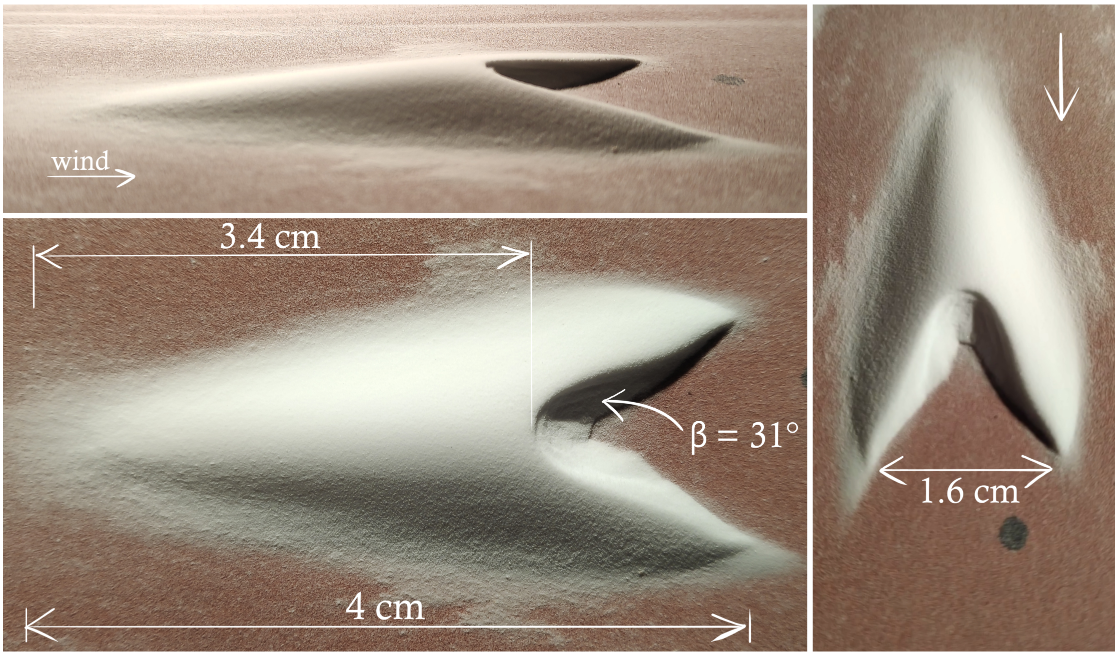

Figure 4.11.: Close-up perspective photo of the steady state bedform formed from an irregular-shaped initial heap (see the last image in figure 4.10). The white arrow indicates the wind direction. The bedform's characteristics are a V-shaped body, smooth surface, a sharp crest with well-defined horns, and an area with particles along the horns, which have an angle of repose of 31 degrees at the central line.

4.4. Discussion

Our results show the evolution of a particle heap of coated hollow microspheres into a self-organizing, migrating bedform under aeolian transport. The bedform's morphological characteristics are a crescent-shaped body and crest, preceding horns that face downwind, and an asymmetrical cross-section, with a gentle slope upwind and a steeper slope following the crest downwind. The steep slope downwind has the characteristics of a dune's slip face, which is the lee side of a dune where the slope approximates the angle of repose of loose sand. For medium-fine sands, the angle of repose varies from 30.5 to 35.45° [103], which is in agreement with our results.

Thus, our bedform features all morphological characteristics of a barchan dune, introduced in section 1.4.2 while exhibiting the dimensions of a centimeter-sized ripple. Barchan dunes evolve and migrate under unidirectional wind and low sand availability, which applies to our bedforms. We propose the name barchan-ripple to combine the bedforms' ripple-sized dimensions to its morphological similarity to barchan dunes.

This experiment demonstrates that the structure described in section 4 is not a random feature of our experimental conditions or the setup. We observe the formation of the same barchan in different sizes below 4 cm throughout the test area in the wind tunnel.

Our barchan-ripple evolves from an initial particle pile, and we distinguish between three phases of the experiment.

1. The initial position

The initial position is where we poured the particle pile. The initial barchan, or proto-barchan, shows small surface indentations and remains at this position for 2/3 of the total experiment duration. The total length L increases together with its maximum height h_{max}. The height growth indirectly proves that the saturation length l_{sat} of the system is small enough to allow particle deposition before the crest. Only the condition $\delta_\tau > l_{sat}$ allows a bedform to grow (see section 1.4).

2. Wings-Phase

As soon as the barchan leaves its initial position, the turnover time decreases significantly in the wings regime. Trailing arms (wings) pointing upwind develop shortly after the second image from the left in figure 4.3, turning the bedform's body into a shape that has a remarkable resemblance to barchan dunes, whose horns are fixed by vegetation [114]. We assume that the combination of cohesive material and the sandpaper-covered test section leads to wing development. The experimental condition is similar to an environment in which barchan dunes are surrounded by vegetation, and plants fix their horns [2, 114–116].

The barchan's surface is smooth, and we can no longer observe any indentations. The length shortens abruptly in the wings-phase, giving the impression that the barchan is relaxing into its self-organized V-form shape. The lengths, heights, and height profiles confirm this impression. The surface structure, dynamics, and morphology change as soon as the barchan leaves its initial position. However, this only occurs after the entire material has been rearranged once by the wind.

The barchan reaches its maximum height. In the transient phase, which covers the initial position and wings-phase, the bedform grows by 1 mm in height, which corresponds to 20% of the first height obtained after turning on the wind.

3. Steady State

We observe the barchan-ripple in its invariant shape, migrating several turnover times downwind with stable lengths and widths in the steady state. A sharp crest and well-defined horns characterize the stable morphology and a generally distinct body shape with a gentle slope of about 11 degrees upwind and a slip face downwind with an angle of repose of about 31 degrees. We can clearly distinguish the barchan's steady state shape from the proto-barchan, which exhibits a transient morphology. Although the height decreases slowly in this phase, the height profile shape remains stable. In addition, the initial pile is not a prerequisite for forming a steady state barchan-ripple, as shown in figure 4.10.

Comparison with subaqueous ripples and aeolian dunes

The aeolian barchan-ripple morphology is strikingly similar to subaqueous ripples and aeolian barchan dunes. We know, that mature subaqueous ripples and aeolian dunes have a height-to-length ratio of approximately 1/15 [12, 82, 83]. For a total length of the steady state dune of 4 cm the ratio gives a height of approximately 3 mm, which is in agreement with our results. If we apply equation (1.24) [10], which is the bedload saturation length predicted by Duran Vinent et al. [10], with values from our particle system and fluid, it yields:

$$l_{sat} = \frac{a_b \, \mathrm{Re}_d \, d}{Ga^{1.2}} = \frac{140 \cdot 0.6}{0.85^{1.2}} \cdot 43\,\mu\mathrm{m} \sim 4\,\mathrm{mm} \tag{4.1}$$

with the proportionality constant $a_b = 140$, the grain-based Reynolds number Re_d, the Galileo number Ga and the particle diameter d (for details see section 2.2.4). The maximum wavelength λ_{max} is derived by the maximum growth rate [55] (see section 1.4) and is proportional to the saturation length l_{sat}:

$$\lambda_{max} \sim 12 l_{sat} \sim 5\,\mathrm{cm}. \tag{4.2}$$

The prediction of approximately 5 cm as the bedform's maximum size agrees with our results. Even at higher initial volumes, as shown in figure 4.10, the barchan-ripple relaxes to a size of about 4 cm.

If we apply equation (1.20) for the saturation length with saltation as transport mechanism, we obtain approximately 4 cm for l_{sat}. This value is close to the size of the barchan-ripple, which implies that our initial 5 cm particle heap should be entirely eroded by the wind without any height growth [62].

We can conclude from the height measurements and image analysis that the barchan seems to loose particles that are not deposited at the crest. Since we did not equip our setup with a particle feeder, the barchan suffers a net loss of particles and migrates shrunken to a smaller size. Therefore, we assume that the particles go into suspension, which is qualitatively supported by the results in figure 4.10 and by the decreasing central slice area given in table 4.1. In addition, the superimposed images show a significant decrease in the bedform's length and width. However, measurements of the transport mechanisms at work are necessary to prove this hypothesis. Furthermore, we find that the barchan-ripple's steady state shape varies slightly. The comparison of figure 4.8 and 4.11 shows more pronounced wings in the first figure. The material's cohesion might be the origin of this since the test surface has the same sandpaper surface in both cases. However, this remains only a qualitative observation and should be investigated further.

4.5. Conclusions

We showed that a particle heap of coated hollow microspheres evolves into self-organizing, migrating structures under aeolian transport. The shape is that of a barchan dune, while its dimensions are ripple-sized, so we propose the name barchan-ripple. The experimental process is characterized by three phases: the initial position, the wings-phase, and the steady state.

The first phase spans 2/3 of the experiment time and is characterized by the elongation of the barchan body, height fluctuations, and small indentations on the surface. After that, the previously roundish proto-barchan evolves into an elongated barchan-ripple, with trailing arms (wings) pointing upwind. The overall length shortens, and the barchan-ripple reaches its maximum height. The barchan-ripple converges into a steady state in the final phase, with a stable morphology. While maintaining constant height profile shapes, the height slowly decreases in the last phase.

Furthermore, we observe that the barchan-ripple grows in height. This indicates a saturation length of a few millimeters since only in this case, $\delta_\tau > l_{sat}$ deposition of particles occurs before the crest [10]. A comparison with characteristic parameters highlights that the barchan-ripples observed in this study are subject to the same longitudinal instability as subaqueous ripples and aeolian dunes.

Finally, based on the predictions from numerical models and the derived quantities for bedform sizes that should appear, we suggest that the dominant transport mechanism for barchan-ripple formation is viscous bedload transport. This hypothesis motivates further detailed investigations and will be the following chapter's focus.

5 Aeolian Viscous Bedload as Transport Mechanism

Single frame image of an aeolian viscous bedload barchan-ripple

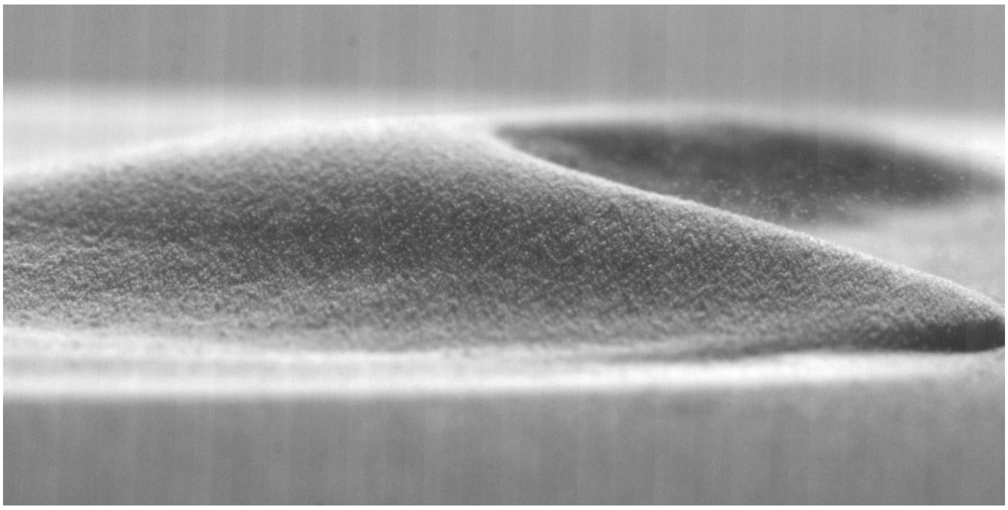

'It seemed to me, however, that the subject of sand movement lies far more in the realm of physics than of geomorphology; and if any advance were to be made in our knowledge of it, it must in the first instance be approached via the study of the behaviour of a single grain in a stream of wind.'

R.A.Bagnold (1941)

Studying the formation of aeolian bedforms in the laboratory governed by the viscous bedload transport regime requires carefully selecting the material used. Here we show that the dominant transport mechanism leading to the formation of aeolian barchan-ripples is viscous bedload transport. To do this, we compare two particle systems with similar densities and different particle diameters (43 and 80 µm). We measure the particle velocity under wind exposure via high-speed imaging and find that the velocities differ by a factor of 4, consistent with the prevailing wind velocities at the respective transport layer height. Finally, we show that a heap of 80 µm particles erodes within seconds, which agrees with the predicted saturation length and corresponds to a hydrodynamic roughening inducing a turbulent hydrodynamic response. Our results show the transition from bedload-to-suspension-transport controlled by the delicate balance of aeolian viscous sublayer thickness and particle diameter.

5.1. Introduction

In the last two chapters, we studied the formation of aeolian barchan-ripples comprised of coated hollow glass microspheres from a flat particle bed and a single particle heap, following the development from the onset to a mature bedform in its steady state. We derived a local saturation length l_{sat} of a few millimeters from the particle flux over a flat bed (section 3.3.3); however, the total flux did not saturate on the length scales available to us. From this measurement and previous considerations and calculations (chapter 2), we suggested that two types of transport must be at work: viscous bedload and suspension.

We concluded that the dominant transport mechanism responsible for the formation of barchan-ripples is viscous bedload transport and that the suspension component causes the observed bedform to lose height even in the steady state. So far, our argument is based only on calculations of numerical model predictions and derived quantities indicative of the dominant transport regime.

Here we demonstrate that the transport mechanism responsible for aeolian barchan-ripple formation is viscous bedload. To this end, we select a similar particle system to that introduced in section 2.2 that differs only in particle diameter (43 µm vs. 80 µm). In the methods section 5.2, we introduce the properties of this particle system, describe the setup we will use to determine the particle velocity on a heap, and finally introduce a theoretical expression for the saturation length derived by Pähtz et al. [46], that is directly dependent on the particle velocity. This provides us an additional l_{sat}, whose value we can compare with the saturation lengths calculated in previous chapters.

Finally, we show that an 80 µm particle heap does not grow in its height and transitions to a transient bedform before being eroded by the wind, which is in agreement with the calculated l_{sat}. We discuss the significance of our results afterward and finally classify our experiment into the numerical model of Duran Vinent et al. [10].

5.2. Experimental Methods

Material Selection

In section 2.2, we introduced and characterized the hollow glass microspheres (HGMs) Q-CEL® 5020FPS. As an additional type for the experiments in this chapter, we chose the HGMs Q-CEL® 6019, which have a particle diameter of 80 microns and a density of $190\,\mathrm{kg\,m^{-3}}$ [117], similar to the $43\,\mathrm{\mu m}$ particle density of $236\,\mathrm{kg\,m^{-3}}$.

The sample preparation includes the coating process, the oven treatment, the sieving process, and the resting time of a few days to minimize triboelectric charging, as described in detail in section 2.2.3. We calculated a ratio of 0.0033 for the Aerosil coating following the calculations presented in section 2.2.4. The time in the vacuum oven was the same for both types of particles. To exclude smaller particles than 80 microns from the heap, we sieved out all particles below 80 microns. Then, as described in section 4.2 we poured the prepared particles through a double-funnel. Finally, we exposed both heaps to a wind speed of approximately $3.1\,\mathrm{m\,s^{-1}}$.

Experimental Setup

Figure 5.1 shows the setup for determining particle velocities on the heap using high-speed imaging. We use the high-speed camera introduced in section 2.3.2. There are two techniques to illuminate the heaps for tracking: with the laser sheet on the central line (1) or by illuminating the entire test area with a spotlight (2). For the measurement of the particle velocity of the $43\,\mathrm{\mu m}$ particle system we use method 2, as the particle motion was difficult to detect with the former method, which we used for the $80\,\mathrm{\mu m}$ particles. The camera captures 1000 frames per second; from a calibration measurement, we know the scale; thus, we can calculate the particle velocity. We manually selected 50 different particles from a three-second high-speed recording window for both particle systems and measured their velocity. The average particle velocity is the mean of the 50 measurements; the error corresponds to the standard deviation. In addition, we determined the height profiles of a particle heap using the laser method, as described in detail in chapter 3.

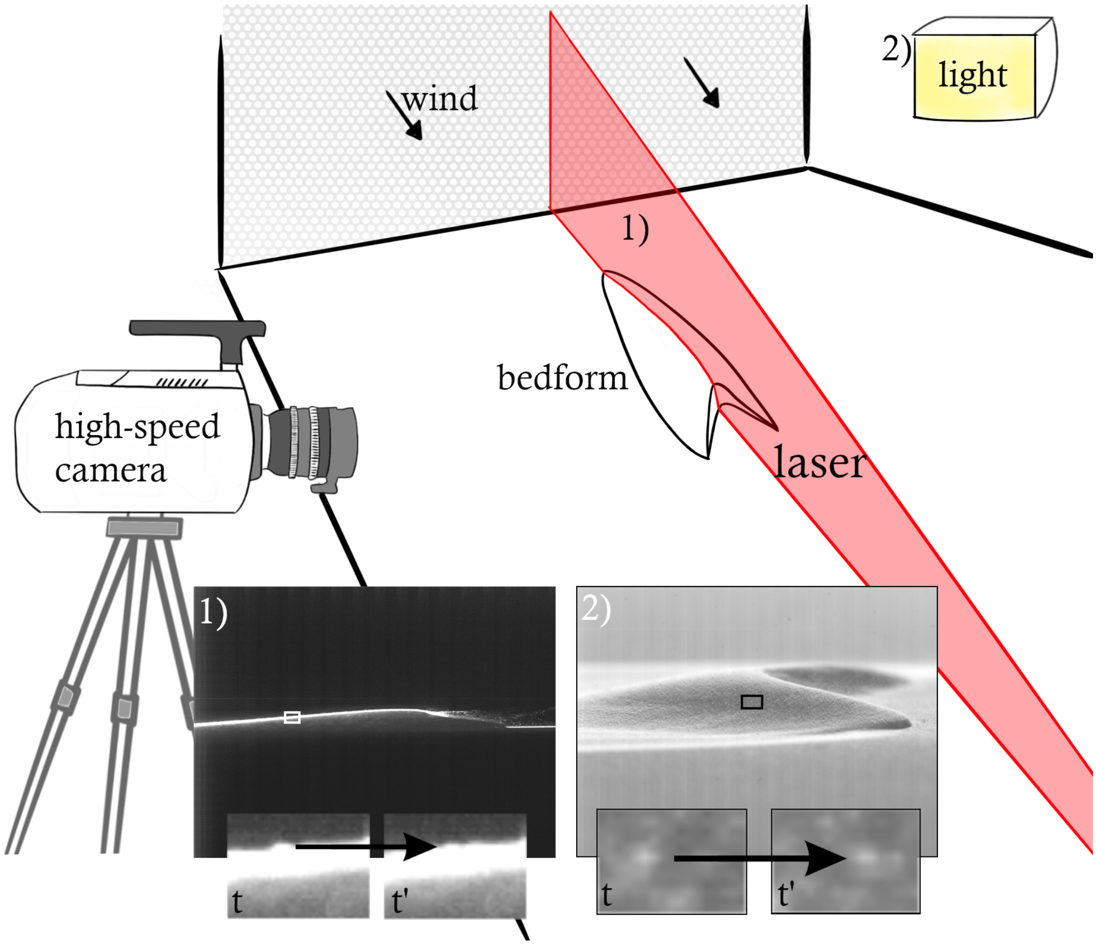

Figure 5.1.: Schematic of the experimental wind tunnel setup for the determination of particle velocities. We obtained the high-speed camera images with 1) a laser sheet on the heap or 2) spotlight illumination. The insets show the tracking principle with the two techniques; the arrow in the inset points on a particle moving between two frames.

Saturation Length as a Function of Particle Velocity

In section 1.3.3 we introduced a saturation length derived by Pähtz et al. [46] which is a function of the average particle velocity. We will measure the particle velocities of both particle systems and thus have access to the predicted saturation length. There are two different expressions, depending on the transport regime. For the subaqueous regime, the saturation length is:

$$l_{sat}^{subaq} = [2s+1]c_v V_s V_{rs} F[\mu(s-1)g]^{-1} \tag{5.1}$$

with the particle-fluid density ratio s, the gravitational acceleration g, V_s the average particle velocity towards its steady state value, V_{rs} the steady state value of the relative velocity V_r, the value F depending on V_{rs} and the steady state particle speed square correlation $c_v \approx 1.3(1.7)$, for aeolian (subaqueous) conditions. We have access to all values and only need to measure the particle velocity. The expression for V_{rs}, the steady state value of the relative velocity V_r, is given by:

$$V_{rs} = [\sqrt{8\mu(s-1)gd/9 + (8\nu/d)^2} - 8\nu/d] \tag{5.2}$$

with the Coulomb friction coefficient μ as an empirical quantity. Pähtz et al. [46] derive μ for both subaqueous ($\mu_{sub} \approx 0.5$) and aeolian conditions ($\mu_{aeol} \approx 1.0$). All other values, such as particle diameter d, particle-fluid density ratio $s = \rho_p/\rho_f$, kinematic viscosity ν and g are at hand. The value F is dependent on V_{rs} and given by:

$$F = [V_{rs} + 16\nu/d][2V_{rs} + 16\nu/d]^{-1}. \tag{5.3}$$

For the saturation length under aeolian conditions there is a simpler form in the limit of large u_*/u_t:

$$l_{sat}^{aeol} \approx 3c_v V_s^2[\mu g]^{-1}. \tag{5.4}$$

We refer to reference [46] and the article's supplemental material for the derivation and more details on the expressions and their values. We will calculate the subaqueous and aeolian saturation length for both particle systems, respectively, to compare them later in the discussion.

5.3. Results

5.3.1. Transition from Viscous Bedload to Suspension

Figure 5.2 shows two single frame images of particle heaps consisting of 43 µm and 80 µm sized particles recorded during to equally strong wind exposure in lateral view. The length scale is valid for both images; the white arrow indicates the wind direction. The inset shows two schematic drawings from reference [10], which we introduced in section 1.4 and will address in the discussion. The top image shows a heap consisting of 43 µm sized particles, which corresponds to the barchan-ripple in the steady state. On the downwind side, we see a cloud of particles that allows resolving individual particles in contrast to the dark background. We measure a transport layer thickness of about 0.1 mm on the downwind, slightly overexposed side. The transport layer thickness corresponds to the height in which the particle motion occurs. In the lower image, we observe moving particles across the entire surface. Here the layer thickness expands to about 1 mm, and we can resolve individual particles above the overexposed layer, entrained by the wind tangentially to the heap.

For the 43 micron-sized particles, we measured an average particle velocity with the method described in section 5.2, and obtain:

$$v_{43} = 0.32 \pm 0.08\,\mathrm{m\,s^{-1}} \tag{5.5}$$

and for the 80 micron sized particles:

$$v_{80} = 1.4 \pm 0.3\,\mathrm{m\,s^{-1}}. \tag{5.6}$$

The thickness of the viscous sublayer δ_ν is proportional to the kinematic viscosity ν divided by the shear velocity u_* according to equation (1.7) and is approximately 70 µm for the set wind speed. The measured shear velocity was $u_* = 0.207 \pm 0.012\,\mathrm{m\,s^{-1}}$ and the roughness length $z_0 = 35 \pm 14\,\mu\mathrm{m}$. The 43 µm micron-sized particles are smaller than the viscous sublayer thickness, for which a linear velocity profile according to equation (1.8) applies; we calculated the shear velocity for the used wind speed in our system in section 2.3.

This results in a wind speed at height $z = 0.1\,\mathrm{mm}$ of:

$$U_{43}(z) = \frac{u_*}{\delta_\nu} z = \frac{0.207\,\mathrm{m\,s^{-1}}}{70\,\mathrm{\mu m}} \cdot 0.1\,\mathrm{mm} = 0.30 \pm 0.04\,\mathrm{m\,s^{-1}}. \tag{5.7}$$

For the 80 micron sized particles, we calculate the wind speed at 1 mm height according to the law-of-wall (eq. 1.5):

$$U_{80}(z) = \frac{u_*}{\kappa} \ln\left(\frac{z}{z_0}\right) = 1.7 \pm 0.2\,\mathrm{m\,s^{-1}} \tag{5.8}$$

with the Kármán constant $\kappa = 0.4$.

In table 5.1 we list the basic parameters we used to calculate the saturation lengths for both types of particles and give the results in the last two rows. We use two expressions, equations (5.1) and (5.4), introduced in the methods section. Our calculations yield $l_{sat}^{subaq} = 0.15\,\mathrm{cm}$ and $1.8\,\mathrm{cm}$ for the bedload saturation length, and an aeolian saturation length of $l_{sat}^{aeol} = 4\,\mathrm{cm}$ and $78\,\mathrm{cm}$ of the 43 µm and 80 µm particle systems, respectively.

		particle type		
Parameter	Notation	5020FPS	6019	Unit
Particle velocity	v	0.32 ± 0.08	1.4 ± 0.3	$\mathrm{m\,s^{-1}}$
Particle density	ρ_p	236	190	$\mathrm{kg\,m^{-3}}$
Particle diameter	d	43	80	µm
Density ratio	$s = \rho_f/\rho_p$	197	158	
Fluid density	ρ_f	1.2		$\mathrm{kg\,m^{-3}}$
Gravitational acceleration	g	9.81		$\mathrm{m\,s^{-2}}$
Kinematic viscosity	ν	$1.45 \cdot 10^{-5}$		$\mathrm{m^2\,s^{-1}}$
Subaqueous l_{sat}	l_{sat}^{subaq}	0.15	1.8	cm
Aeolian l_{sat}	l_{sat}^{aeol}	4	78	cm

Table 5.1.: Basic parameters used to calculate the saturation length for the 43 µm and 80 µm particle system for subaqueous and aeolian cases after Pähtz et al. [46].

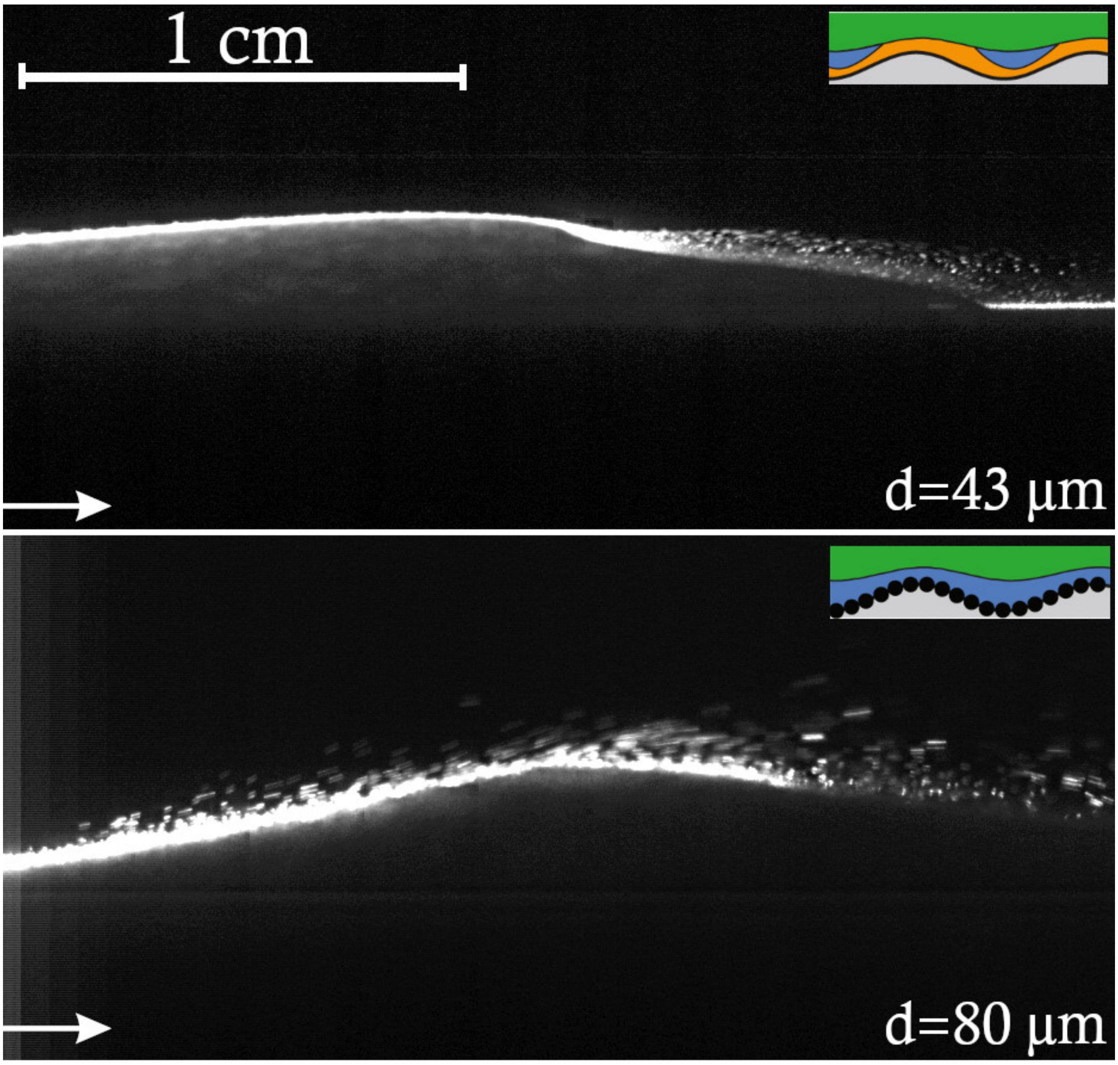

Figure 5.2.: Single frame images of particle heaps consisting of 43 µm (top) and 80 µm sized particles (bottom) recorded during wind exposure in lateral view. The white arrow indicates the wind direction; the given scale is valid for both images. Inset: a schematic showing the hydrodynamic response to the bed topography, addressed in section 1.4; for discussion, see text. The layer above the heap, in which the particles move differs by a factor of 10; the heaps are exposed to the same wind speed of approximately $3.1\,\mathrm{m\,s^{-1}}$ Inset reprinted with permission from reference [10].

5.3.2. Transient Bedform Evolution of 80 µm Particle System

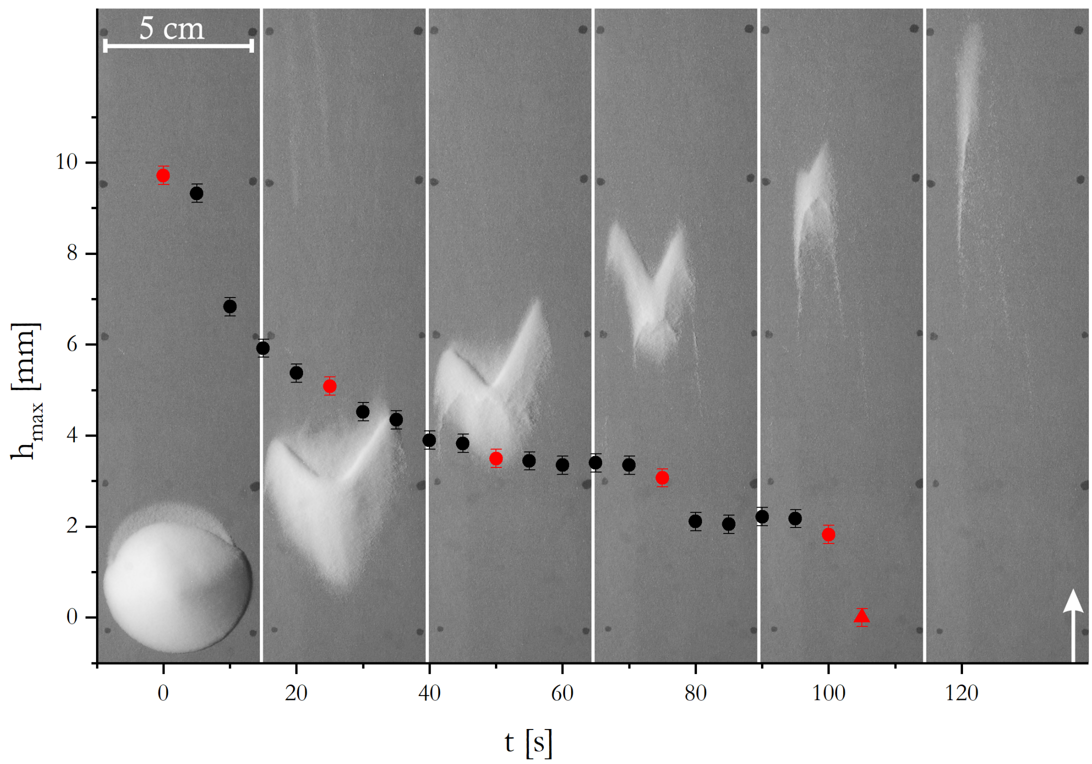

Figure 5.3.: Evolution of the maximum height h_{max} of a particle heap consisting of 80 µm coated hollow microspheres with time. The white arrow gives the wind direction; the scale is valid for every image. Red dots correspond to the bedform's height shown in the image on the background, except the last triangular data point, which is an estimation for the last image. The height decreases continuously. A migrating crescent-shaped bedform evolves out of the particle heap, with two horns pointing downwind, which loses its horn 10 cm downwind until only a thin stripe of material remains on the test surface.

Figure 5.3 shows the evolution of the maximum height h_{max} of a particle heap consisting of 80 µm coated hollow microspheres under aeolian exposure with time. In the background are time-lapse images of the single heaps; we marked the corresponding data point red. The scale for the images is in the upper left; the white arrow indicates the wind direction; the first image shows the bedform before wind exposure. The last data point is a triangle, corresponds to the last image, and was estimated since we could not evaluate the height. The maximum height decreases continuously with time. The images show that the particle heap evolves into a crescent-shaped bedform, with two horns pointing downwind. The bedform migrates, takes on an irregular shape, and loses its horns 10 centimeters downwind. We see only a thin strip of material left on the test surface in the last image.

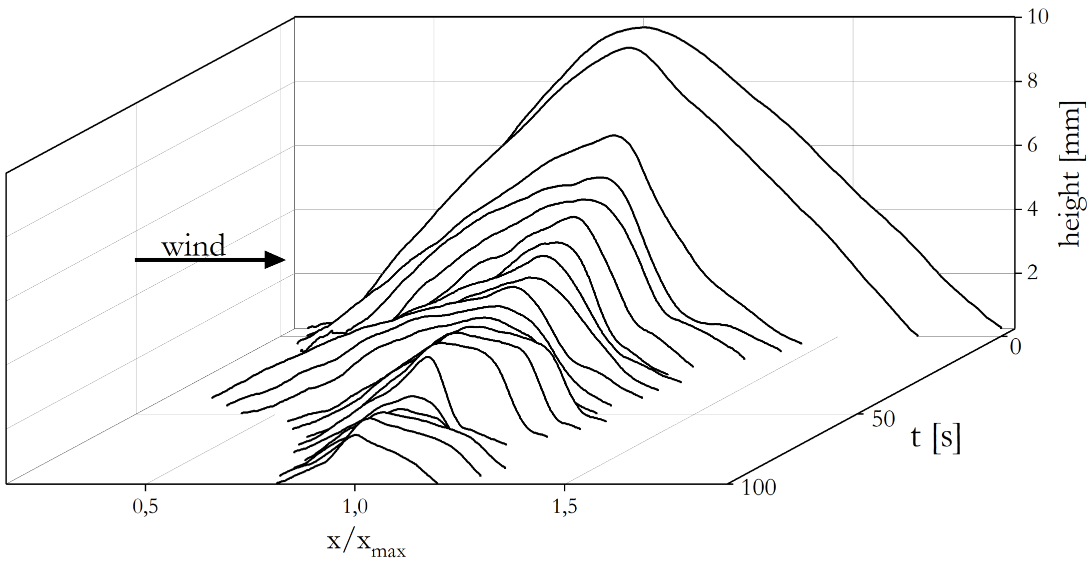

Figure 5.4.: Height profile evolution of a particle heap consisting of coated hollow glass microsphere with 80 µm diameter under aeolian exposure with time (z-axis) and normalized x-axis x/x_{max}. The black arrow indicates the wind direction; the height profiles are 5 seconds apart. The profile in the background shows the initial pile before wind exposure. Over time, the height decreases, and the height profile shape is temporary, changing significantly every 10 seconds.

In figure 5.4, we show the evolution of the height profiles of a particle heap consisting of 80 mum coated hollow glass microspheres under wind exposure in a waterfall diagram. The black arrow indicates the wind direction; the height profiles are 5 seconds apart. The x-axis x/x_{max} is normalized; thus, the position of the maximum height of each profile is at one position, while the y-axis corresponds to the height. The z-axis represents the time in seconds, i.e., the rearmost profile in the background corresponds to the initial heap before wind exposure, and the foremost small profile corresponds to the state after 100 seconds of wind exposure. We observe the successive decrease of the height with time. Furthermore, the profile shape is only temporary; we find a changed profile shape every 10 seconds. Also noteworthy is that a steep downwind slope forms in the first profiles after the experiment has started. In the last two profiles at the very front of the plot, the profile reverses, and the steep slope faces windward.

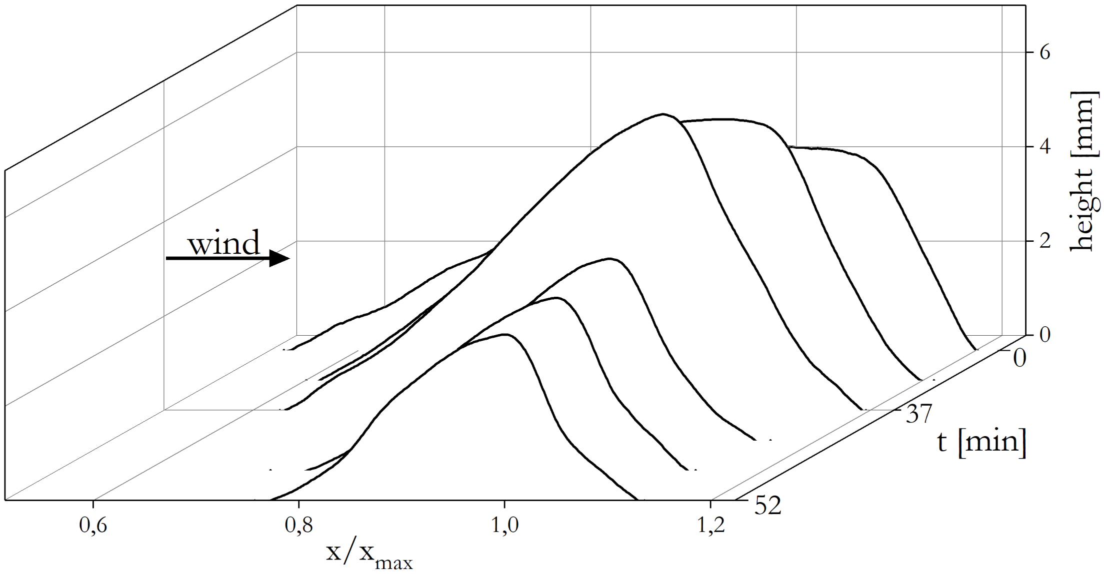

Figure 5.5.: Height profile evolution of a particle heap consisting of coated hollow glass microsphere with 43 µm diameter under aeolian exposure with time (z-axis) and normalized x-axis x/x_{max}. The black arrow indicates the wind direction. The rearmost profile corresponds to the heap after a few minutes of wind exposure; the foremost three show the steady state profiles of the barchan-ripple we characterized in chapter 4.

Figure 5.5 shows selected height profiles of the evolution of a particle heap consisting of 43 µm coated hollow glass microspheres under wind action; the structure we characterized as barchan-ripple in chapter 4. The waterfall plot concept is identical to figure 5.4; the rear profile in the background corresponds to the heap after a few minutes of wind exposure. The z-axis denotes the time in minutes. We observe growth in height from this evolution, followed by a rapid decrease after the third profile. The foremost three height profiles no longer change shape, and we characterized this phase as steady state, as described in chapter 4. The height profiles all have a steep slope in the downwind direction.

5.4. Discussion

We have selected two types of hollow glass microspheres (HGMs) with similar density and coated the particles with Aerosil® R812: Q-CEL® 5020FPS, with a particle diameter of 43 microns, and Q-CEL® 6019, with a particle diameter of 80 microns, where we sieved out all particles below 80 µm in size.

In figure 5.2 we notice that the heaps exhibit different transport layer thicknesses. The larger 80 micron-sized particles are entrained along the entire laser-illuminated line by the wind at the height of 1 mm. In contrast, the particle transport on the heap consisting of 43 micron-sized particles is limited to a height of about 0.1 mm located close to the surface of the heap.

We show that the particle velocities of the different sized particles differ by a factor of four. Furthermore, comparing the wind speed at the same height shows that both particle velocity matches the wind speed within the error limits. The particles are only separated by a difference of 30 microns in diameter, the particle velocities, and transport mechanisms seems to be entirely different.

With the measured particle velocities, we apply equations (5.1) and (5.4) to determine the saturation length, derived by Pähtz et al. [46]. Then, we compare l_{sat} for the subaqueous and aeolian cases for both types of particles. From the results, we conclude that the saturation length of 1.5 mm for the 43 µm particles is in agreement with our previous studies and measured length scales from the last two chapters. In comparison, the predicted saturation length for the aeolian case is 5 cm. This value is not consistent with our previous observations, as the steady state barchan-ripples is stable at a size of approximately 3 to 4 cm and l_{sat}^{aeol} would exceed this length. These results contrast sharply with the 80 micron-sized particle heaps with a longer saturation length between 1.8 cm in the subaqueous and 90 cm in the aeolian case.

Consequently, we show that particle heaps composed of 80 micron-sized particles form a transient bedform that shows no height growth and erodes within 100 seconds. We demonstrate this by measuring the maximum height, time-lapse images, and the evolution of the bedform's height profiles with time. These results indicate that the wind suspends the particles. Finally, a comparison is made between the 80 µm and 43 µm height profiles, plotted in a waterfall diagram (figures 5.4 and 5.5). In these plots, we note that the height profile of the 80 µm particles is temporary and fails to remain stable for 10 seconds. In contrast, the bedform consisting of 43 µm, which we characterized as barchan-ripple in chapter 3, develops a consistent height profile in the steady state over several minutes. How can we interpret this observation?

We assume that the 80 micron particles disrupt the viscous sublayer and are entrained into suspension. With a saturation length l_{sat}^{subaq} of 1.8 cm, bedform formation should be observable in the length scale available to us; however, the viscous sublayer, with a thickness of approximately ~ 70 µm, is too close to the particle diameter. In this special case, we cannot apply equation (5.1). Nevertheless, a temporary structure forms and we observe a migrating bedform. This can be understood as follows: the wind velocity fluctuates slightly, as discussed in section 2.3, which temporarily leads to changes in the thickness of the viscous sublayer. Thus, a migrating bedform still emerges from the 80 µm particle heap; we are at the boundary of viscous sublayer thickness with the 80 µm particle system, but there is no sharp transition. Thus, the viscous sublayer thickens when the velocity decreases slightly, and the particles are not instantaneously entrained in suspension. Due to this soft boundary, some suspension also occurs in our 43 µm particle system, as seen in high-speed camera recordings.

Finally, the comparison between the 80 vs. 43 µm experiment nicely demonstrates that we need to be cautious with conclusions about transport mechanisms and characteristic parameters such as the saturation length, which we only obtain on a morphological basis. For example, in the 80 µm case, we see in the second image in figure 5.3 what appears to be a miniature of a barchan dune from a morphological point of view. However, our analysis shows that the heap of 80 micron-sized particles is below the minimal size, and only a temporary structure can evolve.

Comparison with the Model of Duran Vinent et al. [10]

Finally, we want to discuss the scheme in figure 5.2, which shows the hydrodynamic response of a fluid flowing over a topography [10]. How can we relate our results within the model of Duran Vinent et al. [10]?

The 43 µm particle system is in the hydrodynamically smooth regime at small grain-based Reynolds numbers Re_d, i.e., the particles do not generate particle-scale turbulent fluctuations perturbing the viscous sublayer (see section 1.4). So far, our calculations and observations confirm that our particles are transported within the viscous bedload transport regime, with a secondary suspension component. We classify the 43 µm particle system within the model using figure 1.16. To this end, we calculate kz_0, the wavenumber $k = 2\pi/\lambda$ rescaled by the hydrodynamic roughness z_0 and can estimate the order of magnitude of kz_0. With a wavelength of $\lambda \approx 3\,\mathrm{cm}$, we obtain $k \approx 200\,\mathrm{m}^{-1}$ and from section 2.3 we know that the roughness length is $z_0 = 35\,\mu\mathrm{m}$ and thus $kz_0 \approx 10^{-3}$. According to figure 1.16, we classify the 43 µm particle system to be in the transitional regime, which is also the regime of subaqueous ripples [10].

For the 80 µm particle system, we first have to approximate the bedform wavelength, as we only observe a transient bedform below the minimal size. We use the calculated saturation length from table 5.1 for the aeolian case since we assume that no bedload transport occurs. Using equation (1.28) we can now estimate the wavelength of $\lambda = 10\,\mathrm{m}$ and calculate kz_0. For the 80 micron-sized particle system, we obtain $kz_0 \approx 10^{-5}$, which, according to the model, falls into the turbulent regime. Thus, by change of the particle system from 43 µm to 80 µm results in a shift from transitional to turbulent hydrodynamic response, which we indicated in figure 5.2 inset.

Duran Vinent et al. [10] have used their numerical model to provide a diagram that combines ripples and dunes of different environments into one plot. We add our experimental data points, which can be seen in figure 5.6 (for original plot see figure 1.19). For this purpose, we summarize the saturation lengths of the numerical model of authors Duran Vinent et al. [10] and the theoretical expression from Pähtz et al. [46] for both particle systems, including subaqueous and aeolian cases.

	43 µm	80 µm
Model	Saturation length [cm]	
Pähtz et al. [46]		
Subaqueous l_{sat}^{subaq}	0.15	1.8
Aeolian l_{sat}^{aeol}	4	78
Duran Vinent et al. [10]		
Subaqueous l_{sat}^{subaq}	0.44	0.58
Aeolian l_{sat}^{aeol}	36	53

Table 5.2.: Saturation length predictions according to two different models for the 43 µm and 80 µm particle system.

We want to stress at this point that these values are estimates, and the calculation of the saturation length for aeolian conditions is based on assumptions of the authors, which probably do not apply to our particle system, e.g. no saltation. Nevertheless, the key idea is to compare predicted saturation lengths for subaqueous and aeolian conditions and show that subaqueous equations apply in an aeolian environment in the laboratory wind tunnel.

The appearance of two transport mechanisms acting simultaneously, viscous bedload and suspension, is not reflected in theoretical and numerical models. Nevertheless, the expressions for the saturation length are reliable and agree well with our results in the context of saturation length-dependent parameters. For the 43 µm particle system, the suspension component leads to the height decrease of the barchan-ripple in the steady state. For the 80 µm particle system, the erosion is a consequence of the perturbation of the viscous sublayer.

Figure 5.6 shows the diagram of ripples and dunes in various environments as a function of the rescaled saturation length $l_{sat}u_*/\nu$ and the grain-based Reynolds number Re_d from reference [10] amended with our experimental data points. The turquoise symbols (square and diamond) represent the data points obtained with the calculation from the theoretical expression for the saturation length provided by Pähtz et al. [46], the filled turquoise symbols (square and diamond) data points correspond to the l_{sat} from the numerical model of Duran Vinent et al. [10]. The square symbols represent the barchan-ripples that we characterized in chapters 3 and 4 and the diamonds to the bedforms that form from the 80 µm particles. We labeled these as unstable bedforms because only a transient bedform forms on the length scales available to us. In conclusion, we show that our experimental observations agree with the model. Furthermore, we showed in this chapter that the aeolian barchan-ripples formed from the 43 mum particle system belong to the transitional regime and thus, in contrast to aeolian dunes, do not trigger a turbulent response of the fluid. Thus, the designation ’barchan-ripple’ is reasonable as we distinguish ripples from dunes by considering the hydrodynamic response of the fluid to the topography.

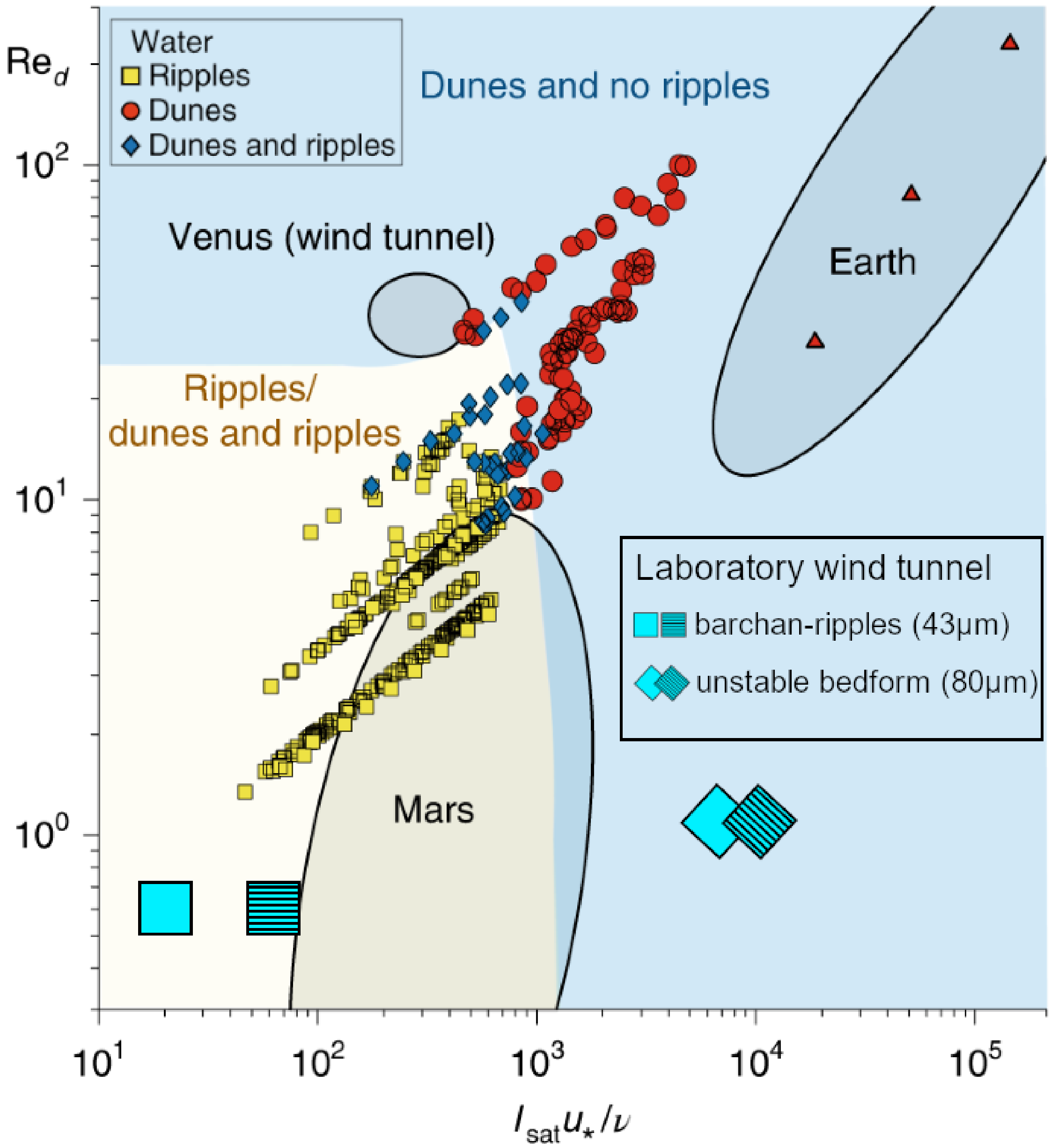

Figure 5.6.: A diagram of ripples and dunes in various environments as a function of the rescaled saturation length $l_{sat}u_*/\nu$ and the grain-based Reynolds number Re_d, which is corrected to include transport effects (for details see supplement of ref. [10]) amended with our experimental data points. The yellow area shows conditions for the presence of ripples and dunes; in the blue area, only dunes are possible. The symbols correspond to water and water-glycerol mixture data (squares, circles, diamonds) and aeolian Earth data (triangles; initial dunes), both for monodisperse sand. To denote the range for different planetary conditions, the areas are shaded. We added our experimental data points to this diagram: square symbols correspond to the barchan-ripples, the diamonds to the bedforms consisting of 80 µm particles. The turquoise filled symbols represent data points calculated with the model from authors Pähtz et al. [46] (square and diamond) and the plain turquoise symbols (square and diamond) to the model of Duran Vinent et al. [10]. Reprinted (and added with our data points) with permission from reference [10].

5.5. Conclusion

We showed that viscous bedload transport is the transport mechanism leading to aeolian barchan-ripples. To do this, we exposed two types of particles with similar densities and different diameters to equally strong winds and measured their particle velocities, which differed by a factor of 4. Furthermore, we have shown that the 80 µm particles go into suspension as they significantly perturb the viscous sublayer. This result is consistent with the calculated saturation lengths from theoretical expressions and numerical models: a heap of 80 µm particles erodes entirely within a minute, while a migrating barchan-ripple forms from the 43 µm particles; corresponding to a hydrodynamic roughening inducing a turbulent response. Finally, we extend a diagram originating from a numerical model with our data points and find agreement with our experimental results. Our results successfully demonstrate the transition from bedload-to-suspension-transport using two similar particle systems of different diameters, an investigation area promising concerning sedimentary bedform formation in its entirety.

6 Summary

A bug leaving its footprints on a dune, Morocco

'Moreover, and this often applies too to the dunes on the borders of deserts, the mere fact of their accessibility permits the feet of animals and of men to interfere seriously with both the structure and the natural movement of their surfaces. The result is a general formlessness; in so much that the average mind associates a sand hill with something essentially chaotic and disordered.'

R.A.Bagnold (1941)

In this thesis, we showed for the first time the formation of aeolian viscous bedload barchan-ripples. These bedforms are governed by the same instabilities, the longitudinal and the transverse, as subaqueous ripples and aeolian dunes and share the same transport mechanism as subaqueous ripples, making our bedforms the aeolian counterpart of subaqueous ripples.

We have been able to access the aeolian viscous bedload transport regime by carefully selecting a suitable particle system: coated hollow glass microspheres with a density of $238\,\mathrm{kg\,m^{-3}}$ and a particle diameter of $43\,\mathrm{\mu m}$ have a low grain-based Reynolds number, assigning the particle system to the hydrodynamically smooth regime. At the same time, the flow in our wind tunnel is high enough to entrain the particles and low enough to maintain a viscous sublayer of about $70\,\mathrm{\mu m}$.

We showed that a flat particle bed consisting of the selected particle system is unstable under unidirectional wind and forms transverse bars that decay into barchan-ripple chains. The transverse bars destabilize after the length $2L_0$, where L_0 represents the barchan-ripple's length from the back to the crest, consistent with numerical simulation results and water-tank experiments. Furthermore, we compared the barchan-ripple chains evolved in our wind tunnel with subaqueous experiments and numerical simulation results, which show a remarkable morphological similarity.

We concluded that a study at a single heap level is possible from the barchan-ripple size that emerged from the flat particle bed. We showed that a particle heap of the selected particle system evolves into a migrating, self-organized barchan-ripple. From studying the structure's height profiles of the central slice and time-lapsed images, we followed the formation from the onset to its mature barchan-ripple shape and showed the relaxation into a stable morphology with constant height profile shapes.

Subsequently, we studied the transport mechanism at a particle level and demonstrated that the aeolian viscous bedload transport regime is responsible for barchan-ripple formation. For this purpose, we compared two heaps consisting of the selected particle system and another particle type, similar in density and composition but with a particle diameter of $80\,\mathrm{\mu m}$. Imaging with a high-speed camera showed that the transport layer thicknesses vary by a factor of ten, and the particle velocities differ by four. Finally, we showed that a heap of 80 µm micron-sized particles forms a temporary bedform shape and erodes, in contrast to the migrating barchan-ripple, and in agreement with a hydrodynamic roughening inducing a turbulent response. Thus, we demonstrated the transition from viscous bedload transport to suspension experimentally using two similar particle systems.

Method and measured value		l_{sat} [mm]	Method Ref.
Measurement			
Saturated particle flux	q(x)	5.4	Andreotti (2010)
Theoretical and numerical models			
Particle system and wind speed	d, ρ_p, u_*	4.4	Duran Vinent (2019)
Minimum width of barchan-ripple	W_{min}	1.3	Parteli (2007)
Particle velocity	v_x	1.5	Pähtz (2013)
Elementary size of barchan-ripple	λ_{max}	2.5	Elbelrhiti (2005)

Table 6.1.: Bedload saturation length derived from a measurement, and theoretical and numerical models for the 43 µm particle system.

We measured and derived the saturation length with expressions from theoretical and numerical models and showed that the order of magnitude of l_{sat} is in the millimeter range. In chapter 3, we measured the particle flux over a flat particle bed and derived a saturation length of 5.4 mm from the local saturation flux. Based on the morphology, i.e., the barchan-ripple's length, width, and height measurements, we also obtained a millimeter-ranged l_{sat}. In the last chapter, we showed, using a theoretical expression for the saturation length and the measured particle velocity, that the saturation length approximately 1.5 mm. Finally, we summarize the obtained l_{sat} in table 6.1 and conclude that we have scaled down the saturation length to a few millimeters.

7 Conclusion and Outlook

A panorama of the star dune field Erg Chebbi, Morocco

'In places vast accumulations of sand weighing millions of tons move inexorably, in regular formation, over the surface of the country, growing, retaining their shape, even breeding, in a manner which, by its grotesque imitation of life, is vaguely disturbing to an imaginative mind.'

R.A.Bagnold (1941)

The novelty of this work is that we demonstrated how a thoughtful selection of a particle system provides access to a transport mechanism previously studied specifically only in water tank experiments. Thus, with a careful selection of the particle system and a suitable wind tunnel, it is possible to study any transport mechanism in the laboratory and the evolution of a variety of sedimentary bedforms in manageable time and length scales.

Laboratory studies remain relevant to study sedimentary bedform development from the onset, calibrate theoretical and numerical models, and gain deeper insight into sedimentary bedform formation. The experiments we presented in this thesis motivate further investigations and provide a new approach to studying these processes. The key is to control the experimental setup: the particle system and the wind tunnel. In the following section, we show the future perspective inspired by this thesis, together with preliminary results, and conclude with a general outlook.

7.1. Particle System

The access to different particle systems offers a promising new approach for laboratory experiments. The controllable parameters are the particle diameter, the particle density, and, with the application of a flow control additive, the interparticle forces. An interesting area of investigation is, for example, to study the effect of triboelectric charge on the entrainment threshold. Recently, a study by Kruss et al. [95] showed that electric charge on the particle surface has an influence on the initiation of sand transport. This study was related to saltation; it would be interesting to investigate the effect on bedload transport.

Moreover, the control of particle size distribution should allow us to perform experiments on bimodal sand transport mechanisms, which are responsible for forming megaripples, a large aeolian ripple with a scale intermediate between ripples and dunes, currently receiving wide attention [10, 11, 81, 118–121]. Regarding the interparticle forces, we would like to show preliminary results with regard to the influence of cohesion on the bedform morphology.

7.1.1. Influence of Cohesion on Bedform Morphology

Motivated by the formation of the trailing arms of the barchan ripple that point upwind, we hypothesized parallels to stabilized bedforms. We know that the morphology of dunes depends on the acting wind direction, the sand availability, and the interaction with the surrounding environment [2, 122]. Vegetation and humidity have a stabilizing effect on dunes, as they hinder sand transport [2, 114–116, 122]. Under these circumstances, a barchan dune, for example, may transform into a parabolic dune. The details of this process are the subject of current research and have so far received little attention in laboratory experiments [123, 124].

We performed experiments with cohesive and less-cohesive heaps and beds of hollow glass microspheres and observed an evolution into two distinct bedforms, resembling parabolic dunes and barchans with trailing arms fixed by slow-growing vegetation.

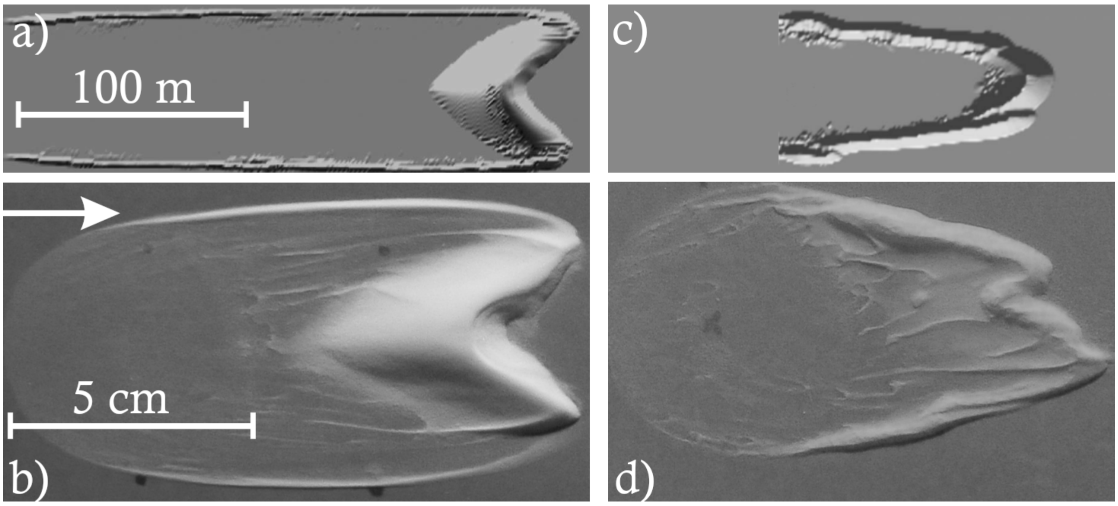

Figure 7.1.: Comparison of two bedforms evolved from b) coated and d) uncoated particle heaps with simulation results of a) a barchan under the influence of slow-growing vegetation and b) a parabolic dune. Inset source: Herrmann et al. [114]. Reproduced and modified with permission from the Coastal Education and Research Foundation, Inc.

In figure 7.1, we compare results from our experiment with simulation results. From the morphological similarity of both structures we can conclude that the experiment with the less-cohesive material resembles a barchan dune in an environment where vegetation grows slowly around the dune and fixes low amounts of sand, while the experiment with the cohesive material is similar to a parabolic dune, which is completely covered by vegetation. Two effects might be at work here: the sandpaper appears like vegetation around the bedform; stronger cohesion appears like vegetation on the bedform.

We also experimented with flat particle beds consisting of coated and uncoated material in this context. Figure 7.2 shows the temporal evolution of both bedforms starting from a round template. Here the question arises of the effect of the initial particle bed configuration on the bedform evolution. From chapter 3 we know that transverse bars form from an initially rectangular configuration. From the round bed, we observe the formation of an approximately 20 cm barchan that tracks a smaller barchan downwind. A shorter wavelength appears to emerge for the uncoated flat bed. Both beds, coated and uncoated, differ significantly in their morphological evolution. We see that the particle system's cohesion influences the morphology of the bedforms formed in the wind tunnel. In the single heap setup the bedforms show a striking resemblance to parabolic dunes and barchans with trailing arms fixed by slow-growing vegetation. These findings are qualitative in nature, but our results show the potential to study the morphology of vegetated sedimentary bedforms using varying coating levels and thus a novel approach to study fixed bedforms in the laboratory.

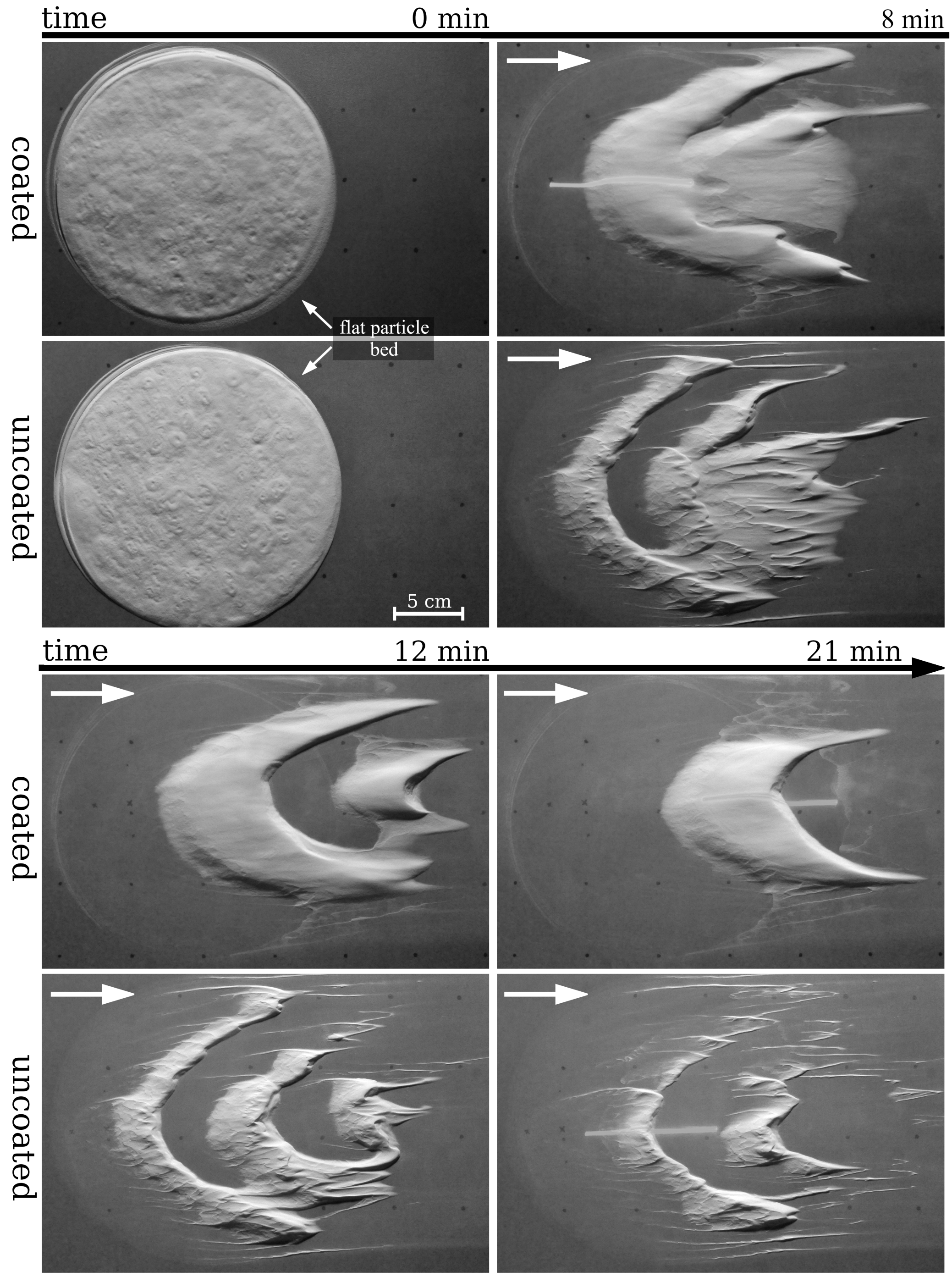

Figure 7.2.: The evolution of a round particle bed of coated and uncoated hollow glass microspheres under a wind speed of $3.1\,\mathrm{m\,s^{-1}}$. The white arrow indicates the wind direction, the timeline is on the top both image panels. The particle system's cohesion influences the morphology of the bedforms, which motivates further investigation.

7.2. Laboratory Wind Tunnel

Several improvements on the wind tunnel setup would broaden the range of possible experiments. An extended test section, ideally with a longer fetch than 10 cm, would provide more space for experiments and decrease turbulence by using roughness elements. Furthermore, a particle supply system may be helpful, serving as an incoming particle flux. These improvements would enable the study of the evolution of dune fields, whose formation is characterized by their long time scales in nature. More practically, a fluidization mechanism is desirable when handling particle systems such as those in this work. As shown in figure 3.5 and 4.3, the bedform's dynamics change as soon as the initial position is left. Therefore, we hypothesize an effect of the material's packing density, changing due to rearrangement by the wind. An investigation in this direction would be promising for studying the influence of packing density on bedform morphology. Furthermore, a flexible test section would be of significant benefit. In the following section, we would like to present preliminary experiments that we have performed with a rotating table.

7.2.1. Effect of Multimodal Winds on Barchan-Ripple Morphology

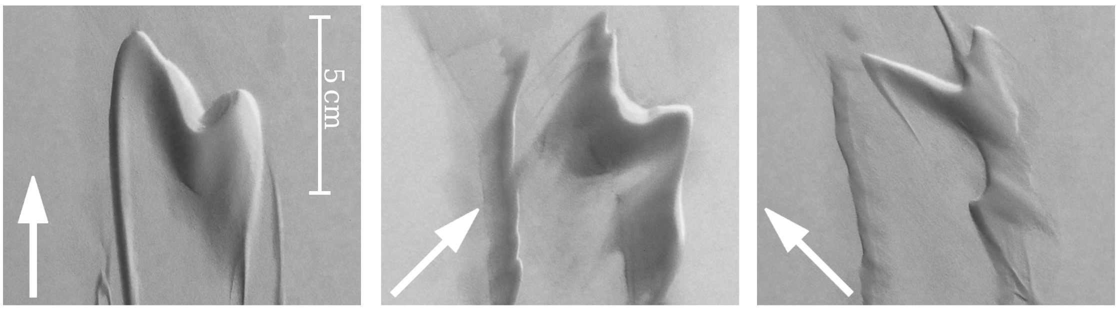

Figure 7.3.: Effect of multimodal wind on bedform morphology. The white arrows indicate the wind direction; the scale is valid for all images. The barchan-ripple evolved from a particle heap of coated hollow microspheres, as introduced in section 2.2, under a wind speed of 3.1 m s^{-1}. The barchan-ripple adapts its morphology to changes in wind direction.

In figure 7.3 we show an experiment with a mature barchan-ripple formed on a rotating plate under a wind speed of $3.1\,\mathrm{m\,s^{-1}}$; demonstrating the effect of multimodal wind exposure on the bedform morphology. We used the particle system introduced in section 2.2. The scale is valid for all images, and the white arrow indicated the wind direction. After the barchan-ripple formed from a particle heap, we exposed the bedform to two different wind directions for 30 s. We observe that the barchan-ripple adapts its shape within this time. It would be interesting to follow the intermediate steps of morphology in detail. In addition to bidirectional and multidirectional wind regimes, asymmetrical sediment supply could be simulated in the laboratory, one of several morphological signatures of asymmetrical barchans on Earth and Mars [9, 125].

In conclusion, besides characteristic parameters that can be calibrated in the laboratory, the formation of bedforms on small scales is significant for its ability to shed light on about the formation conditions of their large counterparts in nature. An extension of this work would be to control the grain-density ratio s, which is only possible with an in-depth knowledge of potential particle systems and a multi-purpose, well-controlled wind tunnel. With the insights from theoretical and numerical models, we would be able to reproduce a spectrum of transport mechanisms and hydrodynamic responses in the laboratory, in particular, the transition from bedload to saltation or suspension, as we showed in this work.

Bibliography

[1] R. A. Bagnold. *The Physics of Blown Sand and Desert Dunes*. New York: Methuen, 1941.

[2] K. Pye and H. Tsoar. *Aeolian Sand and Sand Dunes*. Berlin, Heidelberg: Springer Berlin Heidelberg, 2009. DOI: 10.1007/978-3-540-85910-9.

[3] B. Andreotti, Y. Forterre, and O. Pouliquen. *Granular Media: Between Fluid and Solid*. Cambridge: Cambridge University Press, 2013. DOI: 10.1017/CBO9781139541008.

[4] M. C. Bourke, N. Lancaster, L. K. Fenton, E. J. R. Parteli, J. R. Zimbelman, and J. Radebaugh. "Extraterrestrial dunes: An introduction to the special issue on planetary dune systems". *Geomorphology*. Planetary Dune Systems 121.1 (2010), pp. 1–14. DOI: 10.1016/j.geomorph.2010.04.007.

[5] M. W. Telfer, E. J. R. Parteli, J. Radebaugh, R. A. Beyer, T. Bertrand, F. Forget, F. Nimmo, W. M. Grundy, J. M. Moore, S. A. Stern, J. Spencer, T. R. Lauer, A. M. Earle, R. P. Binzel, H. A. Weaver, C. B. Olkin, L. A. Young, K. Ennico, and K. Runyon. "Dunes on Pluto". *Science* 360.6392 (2018), pp. 992–997. DOI: 10.1126/science.aao2975.

[6] P. Jia, B. Andreotti, and P. Claudin. "Giant ripples on comet 67P/ Churyumov–Gerasimenko sculpted by sunset thermal wind". *Proceedings of the National Academy of Sciences* 114.10 (2017), pp. 2509–2514. DOI: 10.1073/pnas.1612176114.

[7] J. Radebaugh. "Dunes on Saturn's moon Titan as revealed by the Cassini Mission". *Aeolian Research* 11 (2013), pp. 23–41. DOI: 10.1016/j.aeolia.2013.07.001.

[8] M. G. A. Lapôtre, R. C. Ewing, M. P. Lamb, W. W. Fischer, J. P. Grotzinger, D. M. Rubin, K. W. Lewis, M. J. Ballard, M. Day, S. Gupta, S. G. Banham, N. T. Bridges, D. J. D. Marais, A. A. Fraeman, J. A. Grant, K. E. Herkenhoff, D. W. Ming, M. A. Mischna, M. S. Rice, D. Y. Sumner, A. R. Vasavada, and R. A. Yingst. "Large wind ripples on Mars: A record of atmospheric evolution". *Science* 353.6294 (2016), pp. 55–58. DOI: 10.1126/science.aaf3206.

[9] M. C. Bourke. "Barchan dune asymmetry: Observations from Mars and Earth". *Icarus*. MRO/HiRISE Studies of Mars 205.1 (2010), pp. 183–197. DOI: 10.1016/j.icarus.2009.08.023.

[10] O. Duran Vinent, B. Andreotti, P. Claudin, and C. Winter. "A unified model of ripples and dunes in water and planetary environments". *Nature Geoscience* 12.5 (2019), pp. 345–350. DOI: 10.1038/s41561-019-0336-4.

[11] R. Sullivan, J. F. Kok, I. Katra, and H. Yizhaq. "A Broad Continuum of Aeolian Impact Ripple Morphologies on Mars is Enabled by Low Wind Dynamic Pressures". *Journal of Geophysical Research: Planets* 125.10 (2020), e2020JE006485. DOI: 10.1029/2020JE006485.

[12] F. Charru, B. Andreotti, and P. Claudin. "Sand Ripples and Dunes". *Annual Review of Fluid Mechanics* 45.1 (2013), pp. 469–493. DOI: 10.1146/annurev-fluid-011212-140806.

[13] F. Durst. *Grundlagen der Strömungsmechanik: eine Einführung in die Theorie der Strömungen von Fluiden*. Springer, Berlin, Heidelberg, 2006. 758 pp. DOI: 10.1007/978-3-540-31324-3.

[14] T. E. Stanton and R. T. Glazebrook. "The mechanical viscosity of fluids". *Proceedings of the Royal Society of London. Series A, Containing Papers of a Mathematical and Physical Character* 85.579 (1911), pp. 366–376. DOI: 10.1098/rspa.1911.0050.

[15] W. Tollmien, H. Schlichting, H. Görtler, and F. W. Riegels. "Bericht über Untersuchungen zur ausgebildeten Turbulenz". *Ludwig Prandtl Gesammelte Abhandlungen: zur angewandten Mechanik, Hydro- und Aerodynamik*. Berlin, Heidelberg: Springer, 1961, pp. 714–718.

[16] J. Zierep and K. Bühler. *Grundzüge der Strömungslehre*. Wiesbaden: Springer Vieweg, 2018. DOI: 10.1007/978-3-658-20473-0.

[17] B. Andreotti, P. Claudin, O. Devauchelle, O. Duran, and A. Fourrière. "Bedforms in a turbulent stream: ripples, chevrons and antidunes". *Journal of Fluid Mechanics* 690 (2012), pp. 94–128. DOI: 10.1017/jfm.2011.386.

[18] A. Busemann. "Ludwig Prandtl, 1875-1953". *Biographical Memoirs of Fellows of the Royal Society* 5 (1960), pp. 193–205. DOI: 10.1098/rsbm.1960.0015.

[19] *tec-science*. https://www.tec-science.com/. URL: https://www.tec-science.com/mechanics/gases-and-liquids/boundary-layer-and-dimensionless-similarity-parameters/ (visited on 12/30/2021).

[20] F. H. Abernathy. *National Committee for Fluid Mechanics Films*. 1970. URL: http://web.mit.edu/hml/ncfmf.html (visited on 11/19/2021).

[21] H. Ludwieg and W. Tillmann. "Technical Memorandum: Investigations of the wall-shearing stress in turbulent boundary layers". *NACA-TM-1285* (1950).

[22] J. F. Kok, E. J. R. Parteli, T. I. Michaels, and D. B. Karam. "The physics of wind-blown sand and dust". *Reports on Progress in Physics* 75.10 (2012), p. 106901. DOI: 10.1088/0034-4885/75/10/106901.

[23] E. Lajeunesse, L. Malverti, P. Lancien, L. Armstrong, F. Métivier, S. Coleman, C. E. Smith, T. Davies, A. Cantelli, and G. Parker. "Fluvial and submarine morphodynamics of laminar and near-laminar flows: a synthesis". *Sedimentology* 57.1 (2010), pp. 1–26. DOI: 10.1111/j.1365-3091.2009.01109.x.

[24] T. B. Benjamin. "Shearing flow over a wavy boundary". *Journal of Fluid Mechanics* 6.2 (1959), pp. 161–205. DOI: 10.1017/S0022112059000568.

[25] P. S. Jackson and J. C. R. Hunt. "Turbulent wind flow over a low hill". *Quarterly Journal of the Royal Meteorological Society* 101.430 (1975), pp. 929–955. DOI: 10.1002/qj.49710143015.

[26] J. C. R. Hunt, S. Leibovich, and K. J. Richards. "Turbulent shear flows over low hills". *Quarterly Journal of the Royal Meteorological Society* 114.484 (1988), pp. 1435–1470. DOI: 10.1002/qj.49711448405.

[27] J. Finnigan, K. Ayotte, I. Harman, G. Katul, H. Oldroyd, E. Patton, D. Poggi, A. Ross, and P. Taylor. "Boundary-Layer Flow Over Complex Topography". *Boundary-Layer Meteorology* 177.2 (2020), pp. 247–313. DOI: 10.1007/s10546-020-00564-3.

[28] P. Claudin, G. F. S. Wiggs, and B. Andreotti. "Field Evidence for the Upwind Velocity Shift at the Crest of Low Dunes". *Boundary-Layer Meteorology* 148.1 (2013), pp. 195–206. DOI: 10.1007/s10546-013-9804-3.

[29] K. Kroy, G. Sauermann, and H. J. Herrmann. "Minimal Model for Sand Dunes". *Physical Review Letters* 88.5 (2002), p. 054301. DOI: 10.1103/PhysRevLett.88.054301.

[30] F. J. Pettijohn, P. E. Potter, and R. Siever. *Sand and Sandstone*. New York, NY: Springer US, 1973. DOI: 10.1007/978-1-4615-9974-6.

[31] R. Greeley and J. D. Iversen. *Wind as a Geological Process: On Earth, Mars, Venus and Titan*. Cambridge Planetary Science Old. Cambridge: Cambridge University Press, 1985. DOI: 10.1017/CBO9780511573071.

[32] D. Schulze. *Pulver und Schüttgüter: Fliesseigenschaften und Handhabung*. Verfahrenstechnik. Berlin: Springer, 2006. 508 pp.

[33] I. Livingstone and A. Warren, eds. *Aeolian Geomorphology: A New Introduction*. Hoboken, NJ: John Wiley & Sons Ltdl, 2019. 1 p.

[34] Y. Shao and H. Lu. "A simple expression for wind erosion threshold friction velocity". *Journal of Geophysical Research: Atmospheres* 105 (D17 2000), pp. 22437–22443. DOI: 10.1029/2000JD900304.

[35] R. A. Bagnold and G. I. Taylor. "The movement of desert sand". *Proceedings of the Royal Society of London. Series A - Mathematical and Physical Sciences* 157.892 (1936), pp. 594–620. DOI: 10.1098/rspa.1936.0218.

[36] H. J. Casey. *Über Geschiebebewegung*. 19th ed. Berlin: Preuss. Versuchsanst. f. Wasserbau u. Schiffbau, 1935.

[37] A. F. Shields. “Anwendung der Aehnlichkeitsmechanik und der Turbulenzforschung auf die Geschiebebewegung”. PhD thesis. Berlin: Technische Hochschule Berlin, 1936.

[38] P. R. Owen. “Saltation of uniform grains in air”. *Journal of Fluid Mechanics* 20.2 (1964), pp. 225–242. DOI: 10.1017/S0022112064001173.

[39] D. Beladjine, M. Ammi, L. Oger, and A. Valance. “Collision process between an incident bead and a three-dimensional granular packing”. *Physical Review E* 75.6 (2007), p. 061305. DOI: 10.1103/PhysRevE.75.061305.

[40] P. Zhang, D. J. Sherman, and B. Li. “Aeolian creep transport: A review”. *Aeolian Research* 51 (2021), p. 100711. DOI: 10.1016/j.aeolia.2021.100711.

[41] B. Andreotti, P. Claudin, and O. Pouliquen. “Aeolian Sand Ripples: Experimental Study of Fully Developed States”. *Physical Review Letters* 96.2 (2006), p. 028001. DOI: 10.1103/PhysRevLett.96.028001.

[42] G. Sauermann, K. Kroy, and H. J. Herrmann. “Continuum Saltation Model for Sand Dunes”. *Physical Review E* 64.3 (2001), p. 031305. DOI: 10.1103/PhysRevE.64.031305.

[43] B. Andreotti, P. Claudin, and S. Douady. “Selection of dune shapes and velocities Part 1: Dynamics of sand, wind and barchans”. *The European Physical Journal B* (2002), p. 19. DOI: 10.1140/epjb/e2002-00236-4.

[44] F. Charru and E. J. Hinch. “Ripple formation on a particle bed sheared by a viscous liquid. Part 1. Steady flow”. *Journal of Fluid Mechanics* 550.-1 (2006), p. 111. DOI: 10.1017/S002211200500786X.

[45] P. Claudin and B. Andreotti. “A scaling law for aeolian dunes on Mars, Venus, Earth, and for subaqueous ripples”. *Earth and Planetary Science Letters* 252.1 (2006), pp. 30–44. DOI: 10.1016/j.epsl.2006.09.004.

[46] T. Pähtz, J. F. Kok, E. J. R. Parteli, and H. J. Herrmann. “Flux Saturation Length of Sediment Transport”. *Physical Review Letters* 111.21 (2013), p. 218002. DOI: 10.1103/PhysRevLett.111.218002.

[47] B. Andreotti, P. Claudin, and O. Pouliquen. "Measurements of the aeolian sand transport saturation length". *Geomorphology* 123.3 (2010), pp. 343–348. DOI: 10.1016/j.geomorph.2010.08.002.

[48] B. Andreotti, P. Claudin, and S. Douady. "Selection of dune shapes and velocities Part 2: A two-dimensional modelling". *The European Physical Journal B - Condensed Matter* 28.3 (2002), pp. 341–352. DOI: 10.1140/epjb/e2002-00237-3.

[49] A. Fourriere, P. Claudin, and B. Andreotti. "Bedforms in a turbulent stream: formation of ripples by primary linear instability and of dunes by nonlinear pattern coarsening". *Journal of Fluid Mechanics* 649 (2010), pp. 287–328. DOI: 10.1017/S0022112009993466.

[50] O. Duran, P. Claudin, and B. Andreotti. "On aeolian transport: Grain-scale interactions, dynamical mechanisms and scaling laws". *Aeolian Research* 3.3 (2011), pp. 243–270. DOI: 10.1016/j.aeolia.2011.07.006.

[51] T. Pähtz and O. Duran. "The Cessation Threshold of Nonsuspended Sediment Transport Across Aeolian and Fluvial Environments". *Journal of Geophysical Research: Earth Surface* 123.8 (2018), pp. 1638–1666. DOI: 10.1029/2017JF004580.

[52] T. Pähtz and O. Duran. "Fluid forces or impacts: What governs the entrainment of soil particles in sediment transport mediated by a Newtonian fluid?" *Physical Review Fluids* 2.7 (2017), p. 074303. DOI: 10.1103/PhysRevFluids.2.074303.

[53] T. Pähtz, A. H. Clark, M. Valyrakis, and O. Duran. "The Physics of Sediment Transport Initiation, Cessation, and Entrainment Across Aeolian and Fluvial Environments". *Reviews of Geophysics* 58.1 (2020). DOI: 10.1029/2019RG000679.

[54] J. F. Kennedy. "The mechanics of dunes and antidunes in erodible-bed channels". *Journal of Fluid Mechanics* 16.4 (1963), pp. 521–544. DOI: 10.1017/S0022112063000975.

[55] H. Elbelrhiti, P. Claudin, and B. Andreotti. "Field evidence for surface-wave-induced instability of sand dunes". *Nature* 437.7059 (2005), pp. 720–723. DOI: 10.1038/nature04058.

[56] K. Kroy, G. Sauermann, and H. J. Herrmann. "Minimal Model for Aeolian Sand Dunes". *Physical Review E* 66.3 (2002), p. 031302. DOI: 10.1103/PhysRevE.66.031302.

[57] P. Claudin, O. Duran, and B. Andreotti. "Dissolution instability and roughening transition". *Journal of Fluid Mechanics* 832 (2017), R2. DOI: 10.1017/jfm.2017.711.

[58] D. P. Zilker, G. W. Cook, and T. J. Hanratty. "Influence of the amplitude of a solid wavy wall on a turbulent flow. Part 1. Non-separated flows". *Journal of Fluid Mechanics* 82.1 (1977), pp. 29–51. DOI: 10.1017/S0022112077000524.

[59] K. A. Frederick and T. J. Hanratty. "Velocity measurements for a turbulent nonseparated flow over solid waves". *Experiments in Fluids* 6.7 (1988), pp. 477–486. DOI: 10.1007/BF00196509.

[60] D. Poggi, G. G. Katul, J. D. Albertson, and L. Ridolfi. "An experimental investigation of turbulent flows over a hilly surface". *Physics of Fluids* 19.3 (2007), p. 036601. DOI: 10.1063/1.2565528.

[61] F. Charru and E. J. Hinch. "'Phase diagram' of interfacial instabilities in a two-layer Couette flow and mechanism of the long-wave instability". *Journal of Fluid Mechanics* 414 (2000), pp. 195–223. DOI: 10.1017/S002211200000851X.

[62] E. J. R. Parteli, O. Duran, and H. J. Herrmann. "Minimal size of a barchan dune". *Physical Review E* 75.1 (2007), p. 011301. DOI: 10.1103/PhysRevE.75.011301.

[63] M. C. Bourke and A. S. Goudie. "Varieties of barchan form in the Namib Desert and on Mars". *Aeolian Research* 1.1 (2009), pp. 45–54. DOI: 10.1016/j.aeolia.2009.05.002.

[64] R. Greeley, J. Iversen, R. Leach, J. Marshall, B. White, and S. Williams. "Windblown sand on Venus: Preliminary results of laboratory simulations". *Icarus* 57.1 (1984), pp. 112–124. DOI: 10.1016/0019-1035(84)90013-7.

[65] R. Greeley, J. Marshall, and R. Leach. “Microdunes and other aeolian bedforms on Venus: Wind tunnel simulations”. *Icarus* 60.1 (1984), pp. 152–160. DOI: 10.1016/0019-1035(84)90144-1.

[66] P. Hersen, S. Douady, and B. Andreotti. “Relevant Length Scale of Barchan Dunes”. *Physical Review Letters* 89.26 (2002), p. 264301. DOI: 10.1103/PhysRevLett.89.264301.

[67] N. Endo, H. Kubo, and T. Sunamura. “Barchan-shaped ripple marks in a wave flume”. *Earth Surface Processes and Landforms* 29.1 (2004), pp. 31–42. DOI: 10.1002/esp.1010.

[68] O. Dauchot, F. Lechénault, C. Gasquet, and F. Daviaud. ““Barchan” Dunes in the Lab”. *Comptes Rendus Mécanique* 330.3 (2002), pp. 185–191. DOI: 10.1016/S1631-0721(02)01447-X.

[69] P. Hersen. “On the crescentic shape of barchan dunes”. *The European Physical Journal B - Condensed Matter* 37.4 (2004), pp. 507–514. DOI: 10.1140/epjb/e2004-00087-y.

[70] S. Courrech du Pont. “Dune morphodynamics”. *Comptes Rendus Physique*. Granular physics / Physique des milieux granulaires 16.1 (2015), pp. 118–138. DOI: 10.1016/j.crhy.2015.02.002.

[71] A. Warren. *Dunes: dynamics, morphology, history*. RGS-IBG book series. Chichester, West Sussex: John Wiley & Sons Inc, 2013. 219 pp.

[72] N. Endo, T. Sunamura, and H. Takimoto. “Barchan ripples under unidirectional water flows in the laboratory: formation and planar morphology”. *Earth Surface Processes and Landforms* 30.13 (2005), pp. 1675–1682. DOI: 10.1002/esp.1227.

[73] C. Groh, I. Rehberg, and C. A. Kruelle. “How attractive is a barchan dune?” *New Journal of Physics* 11.2 (2009), p. 023014. DOI: 10.1088/1367-2630/11/2/023014.

[74] P. Hersen and S. Douady. “Collision of Barchan Dunes as a Mechanism of Size Regulation”. *Geophysical Research Letters* 32.21 (2005). DOI: 10.1029/2005GL024179.

[75] P. A. Mantz. “Bedforms produced by fine, cohesionless, granular and flakey sediments under subcritical water flows”. *Sedimentology* 25.1 (1978), pp. 83–103. DOI: 10.1111/j.1365-3091.1978.tb00302.x.

[76] S. Capape, J. P. Martín-Vide, and F. Colombo. “Subaqueous Barchans and Plane Beds from Deposition of Quartz Silt”. *Journal of Hydraulic Engineering* 142.12 (2016), p. 06016020. DOI: 10.1061/(ASCE)HY.1943-7900.0001212.

[77] P. Hersen, K. H. Andersen, H. Elbelrhiti, B. Andreotti, P. Claudin, and S. Douady. “Corridors of Barchan Dunes: Stability and Size Selection”. *Physical Review E* 69.1 (2004), p. 011304. DOI: 10.1103/PhysRevE.69.011304.

[78] F. Charru and E. J. Hinch. “Ripple formation on a particle bed sheared by a viscous liquid. Part 2. Oscillating flow”. *Journal of Fluid Mechanics* 550.-1 (2006), p. 123. DOI: 10.1017/S0022112005007871.

[79] F. Charru and E. M. Franklin. “Subaqueous barchan dunes in turbulent shear flow. Part 2. Fluid flow”. *Journal of Fluid Mechanics* 694 (2012), pp. 131–154. DOI: 10.1017/jfm.2011.528.

[80] B. Andreotti, P. Claudin, J. J. Iversen, J. P. Merrison, and K. R. Rasmussen. “A lower-than-expected saltation threshold at Martian pressure and below”. *Proceedings of the National Academy of Sciences* 118.5 (2021), e2012386118. DOI: 10.1073/pnas.2012386118.

[81] M. G. A. Lapotre, R. C. Ewing, C. M. Weitz, K. W. Lewis, M. P. Lamb, B. L. Ehlmann, and D. M. Rubin. “Morphologic Diversity of Martian Ripples: Implications for Large-Ripple Formation”. *Geophysical Research Letters* 45.19 (2018), pp. 10, 229–10, 239. DOI: 10.1029/2018GL079029.

[82] M. Baddock, I. Livingstone, and G. Wiggs. “The geomorphological significance of airflow patterns in transverse dune interdunes”. *Geomorphology* 87.4 (2007), pp. 322–336. DOI: 10.1016/j.geomorph.2006.10.006.

[83] E. Parteli, V. Schwämmle, H. Herrmann, L. Monteiro, and L. Maia. “Profile measurement and simulation of a transverse dune field in the Lençóis Maranhenses”. *Geomorphology* 81.1 (2006), pp. 29–42. DOI: 10.1016/j.geomorph.2006.02.015.

[84] Lisa Dossow. “A wind tunnel study on developement of simple aeolian dunes”. Bachelor thesis. Köln: Universität zu Köln, 2016.

[85] R. Rothon, ed. *Fillers for Polymer Applications*. Polymers and Polymeric Composites: A Reference Series. Springer International Publishing, 2017.

[86] M. Seckin. “From sand pile to migrating dune - morphological transition of a barchan in a laboratory wind tunnel”. Master thesis. Köln: Universität zu Köln, 2018.

[87] V. V. Budov. “Hollow glass microspheres. use, properties, and technology (Review)”. *Glass and Ceramics* 51.7 (1994), pp. 230–235. DOI: 10.1007/BF00680655.

[88] A. Castellanos. “The relationship between attractive interparticle forces and bulk behaviour in dry and uncharged fine powders”. *Advances in Physics* 54.4 (2005), pp. 263–376. DOI: 10.1080/17461390500402657.

[89] K. Meyer and I. Zimmermann. “Effect of glidants in binary powder mixtures”. *Powder Technology* 139.1 (2004), pp. 40–54. DOI: 10.1016/j.powtec.2003.09.007.

[90] K. Meyer. “Nanomaterialien als Fließregulierungmittel”. PhD thesis. Würzburg: Universität Würzburg, 2003.

[91] Evonik. *Technical Datasheet AEROSIL R812*.

[92] J. Wessing. “Modifikation von feinkörnigen Pulvern mit Hilfe von Nanomaterialien”. Master thesis. Cologne: University of Cologne, 2014.

[93] Marcus Eber. “Wirksamkeit und Leistungsfähigkeit von nanoskaligen Fließregulierungsmitteln”. PhD thesis. Universität Würzburg, 2004.

[94] Potters Industries. *Technical Datasheet Hollow Microspheres Q-CEL 5020FPS*.

[95] M. Kruss, T. Salzmann, E. Parteli, F. Jungmann, J. Teiser, L. Schönau, and G. Wurm. “Lifting of Tribocharged Grains by Martian Winds”. *The Planetary Science Journal* 2.6 (2021), p. 238. DOI: 10.3847/PSJ/ac38a4.

[96] K. R. Rasmussen, A. Valance, and J. Merrison. “Laboratory studies of aeolian sediment transport processes on planetary surfaces”. *Geomorphology* 244 (2015), pp. 74–94. DOI: 10.1016/j.geomorph.2015.03.041.

[97] *openPIV*. OpenPIV. URL: http://www.openpiv.net/ (visited on 08/26/2020).

[98] R. J. Wasson and R. Hyde. "Factors determining desert dune type". *Nature* 304.5924 (1983), pp. 337–339. DOI: 10.1038/304337a0.

[99] E. J. R. Parteli, J. S. Andrade, and H. J. Herrmann. "Transverse Instability of Dunes". *Physical Review Letters* 107.18 (2011), p. 188001. DOI: 10.1103/PhysRevLett.107.188001.

[100] H. P. Melo, E. J. Parteli, J. S. Andrade, and H. J. Herrmann. "Linear stability analysis of transverse dunes". *Physica A: Statistical Mechanics and its Applications* 391.20 (2012), pp. 4606–4614. DOI: 10.1016/j.physa.2012.05.042.

[101] E. Reffet, S. Courrech du Pont, P. Hersen, and S. Douady. "Formation and stability of transverse and longitudinal sand dunes". *Geology* 38.6 (2010), pp. 491–494. DOI: 10.1130/G30894.1.

[102] R. D. Lorenz. "Martian Ripples Making a Splash". *Journal of Geophysical Research: Planets* 125.10 (2020), e2020JE006658. DOI: 10.1029/2020JE006658.

[103] C. F. Jenkin. "The pressure on retaining walls." *Minutes of the Proceedings of the Institution of Civil Engineers* 234.1932 (1932), pp. 103–154. DOI: 10.1680/imotp.1932.13306.

[104] R. A. Bagnold and G. I. Taylor. "The size-garding of sand by wind". *Proceedings of the Royal Society of London. Series A - Mathematical and Physical Sciences* 163.913 (1937), pp. 250–264. DOI: 10.1098/rspa.1937.0225.

[105] R. A. Bagnold and G. I. Taylor. "The measurement of sand storms". *Proceedings of the Royal Society of London. Series A. Mathematical and Physical Sciences* 167.929 (1938), pp. 282–291. DOI: 10.1098/rspa.1938.0132.

[106] W. S. Chepil. "Dynamics of Wind Erosion: II. Initiation of Soil Movement". *Soil Science* 60.5 (1945), p. 397. DOI: 10.1097/00010694-194511000-00005.

[107] A. Zingg. "Wind tunnel studies of the movement of sedimentary material". *Proc. 5th Hydraulic Conf.* 34 (1953), pp. 111–35.

[108] P. R. Owen and Gillette, D.A. "Wind tunnel constraint on saltation". *Proceedings on International Workshop on the Physics of Blown Sand, University of Aarhus, Aarhus, Denmark* (1985), pp. 253–269.

[109] J. D. Iversen and B. R. White. "Saltation threshold on Earth, Mars and Venus". *Sedimentology* 29.1 (1982), pp. 111–119. DOI: 10.1111/j.1365-3091.1982.tb01713.x.

[110] *GIMP*. GIMP. URL: https://www.gimp.org/ (visited on 08/26/2020).

[111] *Savitzky-Golay Filter*. The SciPy community - Savitzky-Golay-Filter. URL: https://docs.scipy.org/doc/scipy/reference/generated/scipy.signal.savgol_filter.html (visited on 08/26/2020).

[112] C. Bartneck. *LEGO Brick Dimensions and Measurements*. URL: https://www.bartneck.de/2019/04/21/lego-brick-dimensions-and-measurements/ (visited on 02/02/2022).

[113] O. Duran, B. Andreotti, and P. Claudin. "Numerical simulation of turbulent sediment transport, from bed load to saltation". *Physics of Fluids* 24.10 (2012), p. 103306. DOI: 10.1063/1.4757662.

[114] H. J. Herrmann, O. Duran, E. J. R. Parteli, and V. Schatz. "Vegetation and Induration as Sand Dunes Stabilizators". *Journal of Coastal Research* 246 (2008), pp. 1357–1368. DOI: 10.2112/08A-0011.1.

[115] O. Duran and H. J. Herrmann. "Vegetation Against Dune Mobility". *Physical Review Letters* 97.18 (2006), p. 188001. DOI: 10.1103/PhysRevLett.97.188001.

[116] O. Duran. "Vegetated dunes and barchan dune fields". PhD thesis. Stuttgart: Universität Stuttgart, 2007.

[117] Potters Industries. *Technical Datasheet Hollow Microspheres Q-CEL 6019*.

[118] T. Gough, C. Hugenholtz, and T. Barchyn. "Eolian megaripple stripes". *Geology* 48.11 (2020), pp. 1067–1071. DOI: 10.1130/G47460.1.

[119] R. Yizhaq H., N. Swet, L. Saban, and I. Katra. "Rediscovery of the fluid drag ripples in wind tunnel experiments". *Sixth Intl Planetary Dunes Workshop 2020*. Vol. LPI Contrib. No. 2188. 2020.

[120] T. Pähtz, Y. Liu, Y. Xia, P. Hu, Z. He, and K. Tholen. “Unified Model of Sediment Transport Threshold and Rate Across Weak and Intense Subaqueous Bedload, Windblown Sand, and Windblown Snow”. *Journal of Geophysical Research: Earth Surface* 126.4 (2021), e2020JF005859. DOI: 10.1029/2020JF005859.

[121] K. Tholen, T. Pähtz, H. Yizhaq, I. Katra, and K. Kroy. “Megaripple mechanics: bimodal transport ingrained in bimodal sands”. *Nature Communications* 13.1 (2022), p. 162. DOI: 10.1038/s41467-021-26985-3.

[122] H. Tsoar and D. G. Blumberg. “Formation of parabolic dunes from barchan and transverse dunes along Israel’s Mediterranean coast”. *Earth Surface Processes and Landforms* 27.11 (2002), pp. 1147–1161. DOI: 10.1002/esp.417.

[123] G. Hanoch, H. Yizhaq, and Y. Ashkenazy. “Modeling the bistability of barchan and parabolic dunes”. *Aeolian Research* 35 (2018), pp. 9–18. DOI: 10.1016/j.aeolia.2018.07.003.

[124] D. Zhang, P. Liang, X. Yang, and H. Li. “The control of wind strength on the barchan to parabolic dune transition”. *Earth Surface Processes and Landforms* 45.10 (2020), pp. 2300–2313. DOI: 10.1002/esp.4881.

[125] E. J. R. Parteli, O. Duran, M. C. Bourke, H. Tsoar, T. Pöschel, and H. Herrmann. “Origins of barchan dune asymmetry: Insights from numerical simulations”. *Aeolian Research* 12 (2014), pp. 121–133. DOI: 10.1016/j.aeolia.2013.12.002.

List of Figures

List of Tables

A Appendix

The photos under the chapter headings were taken by the author M. Seçkin during a field trip to the Erg Chebbi star dune field (Morocco) and in the laboratory at the German Aerospace Center in Cologne.

Moreover, we attached the particle size analysis and the pycnometer measurement, the results of which we presented in section 2.2.4.

AccuPyc II 1340 V1.05 Unit 1 Serial #: 2046 Page 1

Sample: Q-CEL-neu-MP-MSK
Operator:
Submitter:
Bar Code:
File: C:\1340\DATA\002-574.SMP

Analysis Gas: Helium
Reported: 24.01.2020 10:26:14
Sample Mass: 0.1192 g
Temperature: 24.23 °C
Number of Purges: 10

Analysis Start: 24.01.2020 9:29:28
Analysis End: 24.01.2020 10:26:14
Equilib. Rate: 0.005 psig/min
Expansion Volume: 0.8599 cm³
Cell Volume: 1.3322 cm³

Summary Report

Sample Volume
Average: 0.5012 cm³
Standard Deviation: 0.0002 cm³

Sample Density
Average: 0.2378 g/cm³
Standard Deviation: 0.0001 g/cm³

AccuPyc II 1340 V1.05 Unit 1 Serial #: 2046 Page 2

Sample: Q-CEL-neu-MP-MSK
Operator:
Submitter:
Bar Code:
File: C:\1340\DATA\002-574.SMP

Analysis Gas: Helium
Reported: 24.01.2020 10:26:14
Sample Mass: 0.1192 g
Temperature: 24.23 °C
Number of Purges: 10

Analysis Start: 24.01.2020 9:29:28
Analysis End: 24.01.2020 10:26:14
Equilib. Rate: 0.005 psig/min
Expansion Volume: 0.8599 cm³
Cell Volume: 1.3322 cm³

Density and Volume Table

Cycle#	Volume (cm³)	Volume Deviation (cm³)	Density (g/cm³)	Density Deviation (g/cm³)	Elapsed Time (mm:ss)	Temperature (°C)
1	0.5016	0.0003	0.2377	-0.0002	17:27	24.26
2	0.5012	0.0000	0.2378	0.0000	21:32	24.21
3	0.5012	0.0000	0.2378	0.0000	27:07	24.24
4	0.5013	0.0001	0.2378	0.0000	31:25	24.25
5	0.5014	0.0001	0.2378	-0.0001	36:03	24.23
6	0.5012	0.0000	0.2378	0.0000	39:49	24.24
7	0.5011	-0.0001	0.2379	0.0001	43:31	24.24
8	0.5011	-0.0001	0.2379	0.0000	47:21	24.22
9	0.5010	-0.0002	0.2379	0.0001	51:40	24.20
10	0.5010	-0.0002	0.2379	0.0001	55:52	24.20

Summary Data	Average	Standard Deviation
Volume:	0.5012 cm³	0.0002 cm³
Density:	0.2378 g/cm³	0.0001 g/cm³

Lehmann&Voss&Co.

HELOS-Partikelgrößenanalyse
WINDOX 5

HELOS (H0069) & RODOS, R3: 0.5/0.9...175µm **2019-08-01, 15:07:00**,176

Q-CEL 5020FPS

x_{10} = 14,41 µm	x_{50} = 40,21 µm	x_{99} = 111,19 µm	**SMD = 20,57 µm**	**VMD = 42,45 µm**
x_{20} = 22,91 µm	**x_{90} = 71,91 µm**	**x_{100} = 147,00 µm**	S_V = 0,29 m²/cm³	S_m = 2917,34 cm²/g

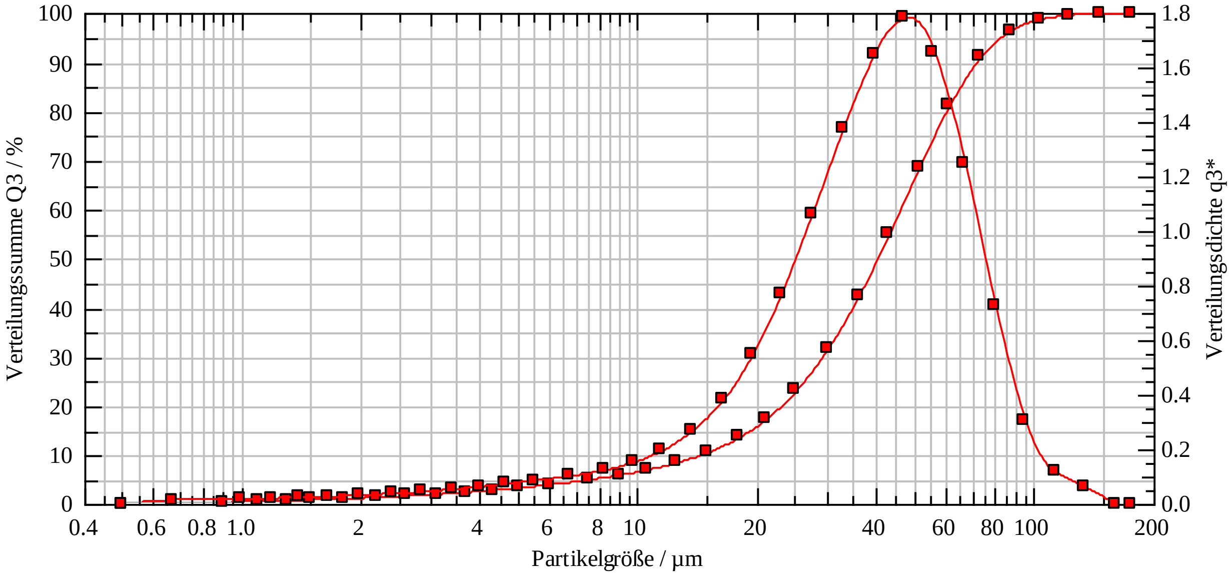

Kommentar:

Benutzerparameter:
Messart: RODOS / R3
EK-/LA-/PA-Nr.: 23800059-01
Charge/Lot-Nr.: E-11754
Prüfer: Lulaj

Verteilungssumme

x_0/µm	Q_3/%	x_0/µm	Q_3/%	x_0/µm	Q_3/%	x_0/µm	Q_3/%
0,90	0,36	3,70	2,34	15,00	10,50	61,00	81,14
1,10	0,52	4,30	2,76	18,00	13,55	73,00	90,88
1,30	0,68	5,00	3,23	21,00	17,23	87,00	96,39
1,50	0,82	6,00	3,91	25,00	23,04	103,00	98,63
1,80	1,04	7,50	4,90	30,00	31,44	123,00	99,53
2,20	1,32	9,00	5,88	36,00	42,34	147,00	100,00
2,60	1,59	10,50	6,90	43,00	55,07	175,00	100,00
3,10	1,93	12,50	8,38	51,00	68,26		

Verteilungsdichte (log.)

x_m/µm	$q_3$lg	x_m/µm	$q_3$lg	x_m/µm	$q_3$lg	x_m/µm	$q_3$lg
0,67	0,01	3,39	0,05	13,69	0,27	55,78	1,66
0,99	0,02	3,99	0,06	16,43	0,38	66,73	1,25
1,20	0,02	4,64	0,07	19,44	0,55	79,69	0,72
1,40	0,02	5,48	0,09	22,91	0,77	94,66	0,31
1,64	0,03	6,71	0,10	27,39	1,06	112,56	0,12
1,99	0,03	8,22	0,12	32,86	1,38	134,47	0,06
2,39	0,04	9,72	0,15	39,34	1,65	160,39	0,00
2,84	0,04	11,46	0,20	46,83	1,78		

Auswertung: WINDOX 5.10.0.0, *HRLD*
Revalidierung:
Referenzmessung: 08-01 15:06:22
Kontamination: 0,00 %

Produkt: _seltene Materialien_
Dichte: 1,00 g/cm³
Formfaktor: 1,00
C_{opt}= 3,36 %

Triggerbedingung: Rm 10s, Nm 10s, opt C.1%
Zeitbasis: 100,00 ms
Start: c.opt >= 1%
Gültigkeit: immer
Stopp: 3s c.opt <= 1% oder 100s Echtzeit

Dispergiermethode: 3 bar, 90% Förderrate
Kaskade: 0
Druck: 3,00 bar, Vakuum: 91,00 mbar
Dosierer: VIBRI
Zuführgeschw.: <E14>

An dieser Stelle möchte ich mich bei all denjenigen bedanken, die mich während der Anfertigung dieser Doktorarbeit unterstützt und motiviert haben.

Zuerst gebührt mein Dank Prof. Dr. Matthias Sperl, der meine Doktorarbeit betreut und begutachtet hat. Für die hilfreichen Anregungen und die konstruktive Kritik bei der Erstellung dieser Arbeit möchte ich mich herzlich bedanken. Ich bedanke mich bei Dr. Eric J.R. Parteli, dem zweiten Gutachter dieser Arbeit, für die wissenschaftlichen Diskussionen und seine Unterstützung.

Ich möchte mich besonders bei Dr. Philip Born bedanken, der mir mit viel Geduld, Interesse und Hilfsbereitschaft zur Seite stand. Bedanken möchte ich mich für die zahlreichen interessanten Debatten und Ideen, die maßgeblich dazu beigetragen haben, dass diese Dissertation in dieser Form vorliegt.

Außerdem möchte ich Dr. Philip Born, Dr. Till Kranz und Louise Shuttleworth für das Korrekturlesen meiner Dissertation danken.

Ich bedanke mich bei Prof. Matthias Sperl, Dr. Stefan Frank-Richter und Philip Pütsch, für den Bau und die Optimierung des Windkanals. Außerdem möchte ich mich bei Dr. Stefan Frank-Richter und Lisa Künstler für die Vorarbeiten zu diesem Thema bedanken.

Ich möchte mich herzlich bei den Studenten bedanken, die mir bei der Umsetzung vieler Experimente geholfen haben: Lisa Stuch, für ihre Geduld am Windkanal und die Experimente zu den runden Teilchenbetten; Tim Breuer, Moritz Menzel und Julian Hellner für die Installation und Instandhaltung der Lüftersteuerung. Ein besonderer Dank gilt an Caimin McKenna, der während seines DAAD RISE Praktikums die PIV Experimente durchführte und mir wesentlich dabei half, die Höhenprofile aufzunehmen.

Weiterhin möchte ich mich bei Matthias Kolbe für die SEM Bilder und Jessica Schettler für die Pyknometer Messung bedanken. Ich danke Thorsten Heyden von der Firma Lehmann und Voss, der mir ausführliche Informationen sowie kleine Probenmengen zur Verfügung gestellt hat. Außerdem möchte ich mich bei allen Mitarbeitern bei der Institutswerkstatt für ihre Geduld und Hilfsbereitschaft bedanken. Ich bedanke mich besonderer bei Katharina Tholen für unsere wissenschaftlichen

Diskussionen. Außerdem danke ich Prof. Dr. Klaus Kroy, der mich in Leipzig herzlich willkommen hieß.

Weiterhin möchte ich mich bei meiner Arbeitsgruppe bedanken, die stets eine lockere Atmosphäre ermöglicht und es mir einfach macht mich wohlzufühlen: Dr. Juan Carlos Arano Romero, Dr. Philip Born, Joelle Eßfeld, Torben Fritsche, Dr. Till Kranz, Lisa Künstler, Dr. Antoine Micallef, Dr. Juan Petit, Advair Salgakar, Prof. Dr. Matthias Sperl, Dr. Karsten Tell, Ya-Chun Wang, und Dr. Peidong Yu.

Ich bedanke mich bei Prof. Dr. Olaf Bubenzer für die Möglichkeit an der Marokko-Exkursion teilzunehmen.

Außerdem möchte ich mich bei Dr. Olfa D'Angelo bedanken, meiner Bürokollegin und Freundin, mit der ich im Rahmen des ESA Programmes Fly Your Thesis! sogar ein paar Minuten schwerelos war. Danke auch an Felix Kuthe, Tolga Bastürk und Abeba Birhane für die unvergessliche Zeit als GrainPower Team.

Meinen Freundinnen Sabrina Seiler und Louise Shuttleworth danke ich besonders für den starken emotionalen Rückhalt über die Dauer meiner gesamten Doktorarbeit. Ich bedanke mich besonders bei Christian Bass und Sabrina Seiler für die emotionale Unterstützung während der Schreibphase.

Abschließend möchte ich mich bei meinen Eltern Hülya und Hayati Seckin bedanken, die stets an meiner Seite standen.

Erklärung zur Dissertation

gemäß der Promotionsordnung vom 02. Februar 2006 mit den Änderungsordnungen vom 10. Mai 2012, 16. Januar 2013 und 21. Februar 2014

Ich versichere, dass ich die von mir vorgelegte Dissertation selbstständig angefertigt, die benutzten Quellen und Hilfsmittel vollständig angegeben und die Stellen der Arbeit - einschließlich Tabellen, Karten und Abbildungen - , die anderen Werken im Wortlaut oder dem Sinn nach entnommen sind, in jedem Einzelfall als Entlehnung kenntlich gemacht habe; dass diese Dissertation noch keiner anderen Fakultät oder Universität zur Prüfung vorgelegen hat; dass sie - abgesehen von unten angegebenen Teilpublikationen - noch nicht veröffentlicht worden ist sowie, dass ich eine solche Veröffentlichung vor Abschluss des Promotionsverfahrens nicht vornehmen werde. Die Bestimmungen dieser Promotionsordnung sind mir bekannt. Die von mir vorgelegte Dissertation ist von Prof. Dr. Matthias Sperl betreut worden.

Köln, den 04.04.2022

Merve Seçkin

Date of birth: 12/04/1988 | **Nationality:** German | **Gender:** Female

EDUCATION AND TRAINING

15/03/2019 – CURRENT – Institute of Materials Physics in Space, Germany
PH.D. IN PHYSICS – Deutsches Zentrum für Luft- und Raumfahrt e.V.

Thesis: Aeolian structure formation in a laboratory wind tunnel

14/06/2016 – 08/02/2019 – Cologne, Germany
MASTER OF SCIENCE IN PHYSICS – Universität zu Köln

Thesis: From sand pile to migrating dune: morphological transition of a barchan in a laboratory wind tunnel

01/10/2011 – 13/06/2016 – Cologne, Germany
BACHELOR OF SCIENCE IN PHYSICS – Universität zu Köln

Thesis: Die Reaktion von Vanadium und Benzol auf Gr/Ir(111)

17/08/2009 – 01/07/2011 – Hagen, Germany
ALLGEMEINE HOCHSCHULREIFE – Rahel-Varnhagen-Kolleg der Stadt Hagen

01/08/2004 – 30/05/2008 – Plettenberg, Germany
STAATLICH ANERKANNTE ERZIEHERIN – Gertrud-Bäumer-Berufskolleg des Märkischen Kreises

PROJECTS

17/02/2020 – 28/02/2020
Multi-method field course in an aeolian sand dune field Erg Chebbi in Morocco

Excursion with research groups Geomorphology and 3DGeo of the Institute of Geography at Heidelberg University

24/09/2018 – 01/12/2019
Fly your Thesis! 2019 - 72nd ESA parabolic flight campaign

Team member of the 'Grain Power 3D-Printing' - group

01/10/2015 – 27/04/2017
Mission X: Train Like an Astronaut 2017

Co-responsibility for MX project; teacher trainings across Germany

SCHOLARSHIPS

01/10/2016 – 31/03/2018
Bonn-Cologne Graduate School of Physics and Astronomy (BCGS) honors branch

01/10/2011 – 31/03/2012
Deutschlandstipendium (German National Scholarship)

PUBLICATIONS

Aeolian structure formation in a laboratory wind tunnel

Merve Seçkin, Philip Born and Matthias Sperl
2021
Deutsche Physikalische Gesellschaft Research Abstract, DPG2021 - DY13.3

From sand pile to migrating dune - morphological transition of a barchan in a laboratory wind tunnel

Merve Seçkin and Matthias Sperl
2019
Geophysical Research Abstract, Vol. 21, EGU2019 -17216

Synthesis of Organometallic Sandwich Complexes and Nanowires on Graphene

Felix Huttmann, Nicolas Schleheck, Merve Seçkin, and Thomas Michely
2016
Deutsche Physikalische Gesellschaft Research Abstract, DPG2016 - O.58.8 (contr.)